Non invasive multimodal analysis of epileptic spikes

Cristian Arnal-Real

Thèse de Doctorat

Mention Biologie Santé
Spécialité Neurosciences

présentée à ***l'Ecole Doctorale en Sciences Technologie et Santé (ED 585)***

de l'Université de Picardie Jules Verne

par

Cristian Arnal-Real

pour obtenir le grade de Docteur de l'Université de Picardie Jules Verne

Modélisation multimodale non-invasive des pointes épileptiques

Soutenue le 26/01/2021, après avis des rapporteurs, devant le jury d'examen :

M. A. Depaulis, DR INSERM, Grenoble	**Rapporteur**
Mme. N. Roche-Labarbe, MCF HDR, Université de Caen	**Rapporteur**
M. P. Derambure, PU-PH, Lille (Président)	**Examinateur**
M. F. Wallois, PU-PH, Amiens	**Directeur de thèse**

GRAMFC

Groupe de Recherche sur l'Analyse Multimodale de la Fonction Cérébrale
INSERM U1105

Non-invasive multimodal analysis of epileptic spikes

Cristian Arnal-Real 2020

Interictal Epileptic spike (IIS) is a key feature of the epileptic network. They are characterized by an increased neural synchronization of a large population of neurons. IIS are the results from a disturbance of the functional balance between various neuronal (synaptic and non-synaptic), vascular, and metabolic compartments.

To better characterize the complex interactions at different scales a simultaneous multimodal-multiscale approach of the activity of these different compartments around the IIS is mandatory. In an epileptic rat model, we simultaneously evaluated (1) the synaptic dynamic by combining electrocorticography and multiunit activity recording in the time and time-frequency domain; (2) the non-synaptic dynamic by recording modifications in light scattering induced by changes in the membrane configuration related to cell activity using the fast optical signal; (3) the vascular dynamic around IIS using functional near infrared spectroscopy and, independently recorded but synchronized to the IIS, the changes in cerebral blood flow using diffuse correlation spectroscopy.

The first observed alteration in the measured signals was in the hemodynamic compartments a few seconds before the peak of the IIS. These hemodynamic changes were followed by changes in coherence and then synchronization between the deep and superficial neural networks in the 1 s preceding the IIS peaks. Finally, changes in light scattering that occurred before the epileptic spikes support the idea of a change in membrane configuration that occurs before the IIS.

Our multimodal and multiscale approach highlights the complexity of (1) interactions between neuronal, vascular, and extracellular compartments, (2) neural interactions between various layers, (3) the synaptic mechanisms (coherence and synchronization), and (4) non-synaptic mechanisms that take place in the neuronal network around IISs in a very specific cerebral hemodynamic environment.

Modélisation multimodale non-invasive des pointes épileptiques

Cristian Arnal-Real 2020

La pointe épileptique interictal (IIS) est une caractéristique clé du réseau épileptique. Elles se caractérisent par une synchronisation neuronale accrue d'une large population de neurones. Les IIS sont les résultats d'une perturbation de l'équilibre fonctionnel entre divers compartiments neuronaux (synaptiques et non synaptiques), vasculaires et métaboliques.

Pour mieux caractériser les interactions complexes à différentes échelles, une approche multimodale-multi-échelles simultanée de l'activité de ces différents compartiments autour de l'IIS est obligatoire. Dans un modèle de rat épileptique, nous avons évalué simultanément (1) la dynamique synaptique en combinant l'électrocorticographie et l'enregistrement de l'activité multi-unitaires dans le domaine temporel et temps-fréquence; (2) la dynamique non synaptique en enregistrant les modifications de la diffusion de la lumière induites par les modifications de la configuration de la membrane liées à l'activité cellulaire en utilisant le signal optique rapide; (3) la dynamique vasculaire autour de l'IIS en utilisant la spectroscopie fonctionnelle proche infrarouge et, indépendamment enregistrée mais synchronisée avec l'IIS, les changements dans le flux sanguin cérébral en utilisant la spectroscopie de corrélation de diffusion.

La première altération dans les signaux mesurés était observée dans les compartiments hémodynamiques quelques secondes avant la pointe de l'IIS. Ces changements hémodynamiques ont été suivis de changements de cohérence puis de synchronisation entre les réseaux de neurones profonds et superficiels dans les 1 s précédant les pointes épileptiques. Enfin, les changements dans la diffusion de la lumière qui se sont produits avant les pointes épileptiques soutiennent l'idée d'un changement de configuration de la membrane survenant avant la pointe épileptique.

Notre approche multimodale et multi-échelles met en évidence la complexité (1) des interactions entre les compartiments neuronaux, vasculaires et extracellulaires, (2) des interactions neuronales entre différentes couches, (3) des mécanismes synaptiques (cohérence et synchronisation), et (4) non synaptiques mécanismes qui ont lieu dans le réseau neuronal autour des pointes épileptiques dans un environnement hémodynamique cérébral très spécifique.

Contents

ACKNOWLEDGEMENTS

There is a wide multitude of people to whom I would like to dedicate this thesis. First, I would like to express my gratitude to my supervisor, *Prof. Dr. Fabrice Wallois* for giving me the opportunity to work in his laboratory. His ability to see beyond, where I could not, showed me the way, either through his excellent guidance, critical comments, and his desire to create a unique work environment. Without your help this would not have been possible. I am also deeply grateful to *Dr. Mahdi Mahmoudzadeh*, without whom my increase in knowledge of signal analysis would not have become possible. He said me that, although things seem to paint badly there is always a possible solution. I am fully grateful to *Dr. Fabrice Wallois* and *Dr. Mahdi Mahmoudzadeh*.

I would like to thank every one of the Inserm-U1105 laboratory, because each of them has given me a vision of identify the problems to finally achieve consistent solutions, I don't forget their continued support and friendship.

I am also indebted to all my friends who are already in France or Spain, they have been accompanying me on this hard path, through their advice and support when one needs it most.

This project was generously funded by the "*Conseil Régional de Picardie*", France. I am grateful for their financial support.

Above all, I would like to thank my couple and all my family without exceptions, to give me their support and courage, and showing that in difficult times one can get the best of yourself.

GLOSSARY

AP anteroposterior

BOLD blood oxygenation level dependent

CBF cerebral blood flow

CBV cerebral blood volume

CSD current source density

CT-scan computed tomography scan

CW Continuous wave

DCS Diffuse correlation spectroscopy

ECoG electrocorticography

ED epileptic discharges

EEG electroencephalogram

EPP early pre-spike period

FD frequency domain

fMRI functional magnetic resonance imaging

fNIRS functional near-infrared spectroscopy

FOS fast-optical signal

Hb hemoglobin

HbO_2 oxyhemoglobin

HbR deoxy-hemoglobin

HbT total hemoglobin

HRF hemodynamic response function

IED Interictal epileptic discharge

IIS interictal epileptic spike

ISI inter-spike interval

LPP late pre-spike period

ML medial-lateral

MLE multi-site linear electrode

MUA multi-unit activity

NIRS near infrared spectroscopy

NVC neurovascular coupling

PDS paroxysmal depolarization shifts

PET positron emission tomography

PG penicillin G

PMT photomultiplier

R return to baseline period

rCBF relative Cerebral Blood Flow

rCBV relative Cerebral Blood Volume

$rCMRO_2$ relative Cerebral Metabolic Rate of Oxygen

RMS root mean square

S1 & **S2** spike 1 & spike 2 periods

SNR signal-to-noise ratio

SPECT single photon emission computed tomography

SW1 & **SW2** slow wave 1 & slow wave 2 periods

T0 time-zero

TD time domain

TFR time-frequency representation

UA unit activity

CHAPTER

1

Introduction and background

1.1. Introduction

Epilepsy is one of the most common neurological disorders around the world of which there are around 50 million epileptic patients. Over 2.4 million of new cases are diagnosed annually. The disease is defined by two or more seizures resulting from brain hyperactivity, which can range from very short episodes of absence or muscle contractions to prolonged and severe seizures. In addition, possible temporary symptoms such as loss of consciousness, and changes in movement, senses, mood states or other cognitive functions might be observed.

One of the key biomarkers in epilepsy is the interictal spike (IIS). The IISs are hypersynchronous events caused by excessive and simultaneous neuronal discharges. The cortical area involved in IISs is quite extensive (Cosandier-Rimélé *et al.*, 2007) and the mechanism that drives these neurons from normal dynamic synchronization to aberrant hyper-synchronization and tight coupling is still not completely understood.

Many groups have created a wide variety of IIS models to understand the underlying mechanisms of the IIS. However, the complex pathophysiological mechanisms of IIS require a global multiscale

approach in order to better understand the interactions between synaptic and non-synaptic, vascular and metabolic interactions within the neural system.

1.1.1. Epilepsy

To define the epilepsy's concept, it is necessary to distinguish between seizures and epilepsy. The epileptic seizures are a transient occurrence of symptoms and/or signs provoked by the excessive and synchronous firing of neuronal populations in the brain. Epilepsy, therefore, is the disease defined by the high tendency to generate seizures including their consequences in the neurobiological, cognitive, social and psychological aspects (Fisher *et al.*, 2005).

The International League Against Epilepsy (ILAE, Fisher et al. 2014) define the epilepsy as follow:

Epilepsy is a disease of the brain defined by any of the following conditions:

1. *At least two unprovoked (or reflex) seizures occurring greater than 24 hours apart.*
2. *One unprovoked (or reflex) seizure and a probability of further seizures similar to the general recurrence risk (at least 60%) after two unprovoked seizures, occurring over the next 10 years.*
3. *Diagnosis of an epilepsy syndrome*

    - *Epilepsy is considered to be resolved for individuals who had an age-dependent epilepsy syndrome but are now past the applicable age or those who have remained seizure-free for the last 10 years, with no seizure medicines for the last 5 years.*

1.1.1.1. Epidemiology

In the worldwide population, 50 million of people are affected by epilepsy. Every year it is estimated that around 5 million of people will be diagnosed with this disease, and around 7 per 1000 will present active epilepsy with recurrent seizures that will require treatment. In most of the cases (~80%) patients are located in countries with low and middle incomes (World Health Organization, 2019).

Prevalence studies in countries around the world in the last century (Banerjee et al., 2009), highlighted the inequality of the populations in front of this disease: 41 per 1000 in Nigeria in front of 3.3 per 1000 in Italy.

The differences in prevalence can be related to endemic pathologies (neurocysticercosis or malaria), medical infrastructures and access to treatment (Banerjee *et al.*, 2009).

1.1.1.2. History

The epilepsy was present all along the history of medicine. The classification as a disease was first debated, considering magic or religious (i.e. possessions) aspects.

One of the first references in the history about epileptic seizures is in the Code of Hammurabi, King of Babylon (1728-1682 B. C.), it was called the "fall down disease" (Ruiz-Ezquerro 2008). Special laws were applied to the people with epilepsy. This increased the fears and prejudices of the people. In a recovered text from tablets dated of the period between 1067 and 1046 B.C. it was related that a patient turns its head to the left, opens its eyes widely, presents hands and feet stiffness and loses consciousness (Garcia-Albea, 1999).

400 years B.C. in the ancient Greece, it was called the 'Sacred Disease' from the scientific and non-scientific communities. In this period, Hippocrates criticized this mystic explanation as it creates misdiagnosis. He attributed the epileptic symptoms to abnormal cerebral function (Office of Health Economics, 1971). Hippocrates had identified that the epilepsy starts during the gestation and that it could be acquired after a traumatic experience.

From the Hippocratic period to the Middle Ages the definition of epilepsy was kept, and some classifications were added. During the Middle Ages and the Renaissance all the naturalistic theories built by Greek Medicine were replaced by the old mystical beliefs. The new beliefs were based on religious texts. In the Bible, it was reported a clear example of epilepsy that was considered as possession (Lennox, 1939).

However, it would not be until the XVIII century that the mystic hypotheses started to disappear. The Swiss Samuel André Tissot (1728-1797 A.D.) published in 1770 the *Traité de l'epilepsie*, a work to mark a definitive separation between the supernatural and scientific origin of epilepsy (Garcia-Albea, 1999).

In the XIX century the experimental medicine gets started with new disciplines like microbiology and histology. In this period all the mystic beliefs get discarded and the epilepsy was considered as a mental disorder. New institutions were created, and autopsies were realized to understand the epileptic mechanisms in antemortem epileptic patients. The studies of Bouchet and Cazauvieilh in 1825 has described macroscopic abnormalities in the temporal lobes and in the hippocampus (Gloor, 1991). Sommer in 1880, has reviewed all the discoveries about the epilepsy and affirmed categorically that the epilepsy is linked with the hippocampus and the nearby tissues. During this century Camilo Golgi and Santiago Ramón y Cajal developed new histological techniques to study the nervous system. New

neuroanatomy concepts were developed with the 'neuron theory'. Advances in semiological and neurophysiological knowledge appeared concurrently.

In the last century, simultaneously to the new knowledges based on histology, the recent technique of clinical electroencephalography was developed. Kaufmann, in 1912, recorded bioelectric activity in an animal model of epileptic seizures. Hans Berger, in 1929, recorded electrical brain activity from the scalp (Millett, 2001). Quickly this method used in research gained importance in the clinical practice, becoming one of the criteria, with clinical evaluation, for diagnosis and classification of seizures and epileptic syndromes. Rapidly, electroencephalogram (EEG) was used as a criteria to differentiate focal and generalized epilepsies (Penfield & Jasper, 1954). The last century was the most important. Thanks to the scientific community the old idea of the sacral disease was definitely demystified, in terms of its origin and nature, and considered as a disease of the brain function.

1.1.1.3. Clinical classification

Seizures can be considered as a brief episode of symptoms due to abnormal excessive neuronal activity in the brain (ictal discharges). It can be classified into different groups:

I. Generalized epilepsy
   a. Absence or minor seizures
   b. Tonic clonic seizures
   c. Myoclonic seizures
   d. Infantile spasms

II. Partial or focal epilepsy
   a. Motor epilepsy
   b. Complex partial
   c. Akinetic seizures
   d. Sensory epilepsy

III. *Status epilepticus* (acute repetitive seizures)

This disorder may result from different etiologies, such as genetic disorders, birth trauma or congenital defect in children and young adults and tumors, cerebrovascular disease in middle-aged adults (Leppik, 1997). Nevertheless, in many cases the underlying cause is unknown.

Nevertheless, certain physiological situations may facilitate the emergence of abnormal discharges that propels the neuronal networks to a pathological epileptic loop. This comprises:

I. Changes in blood glucose concentration
II. Emotional stress
III. Fatigue
IV. Infection meningitis, brain tumors, cerebrovascular disease or metabolic abnormalities
V. Nutritional deficiency
VI. Plasma pH
VII. Total osmotic pressure and electrolytes composition of extra cellular fluids
VIII. Trauma

1.1.1.3.1. Ictal and interictal activities

The period of epileptic seizure is also known clinically as the *ictal period.* This period can last from a few seconds to minutes and is characterized by a significant increase in brain activity which ends when the neuronal activity returns to a state of normal activity. The ictal discharge is characterized by abnormal rhythmic activity made of spikes, spike and waves, rapid activities… Once the ictal period is over, it may be associated in the following minutes by drowsiness, nausea, migraines, headaches, or confusion. This is considered as the post ictal period. The time between the completion of an ictal period and the beginning of another ictal period is considered as *interictal periods.* During this interictal period, abnormal interictal activities can be recorded on the EEG such as isolated spikes, polyspikes, spike and waves. These pathological activities of the epileptic brains are called “Interictal Epileptic Discharge” (IED). Like seizures, IEDs are likely to be generated by the same group of neurons that cause the seizures (Asano *et al.*, 2003; Marsh *et al.*, 2010).

1.1.1.3.1.1. Interictal Epileptic Discharges

The IEDs are commonly recorded in surface EEG and in pre-surgical intracranial EEG to delineate the epileptogenic region in focal epilepsies (Jacobs *et al.*, 2008). The multiple electrophysiological recordings made on the scalp, on the cortex with cortical grids (ECoG), or intracranially by intracerebral electrodes (SEEG) have shown their effectiveness in identifying the different patterns of IED thanks to the proximity of their sources (de Curtis *et al.*, 2012). Different patterns of IED are recorded on the EEG of epileptic patients such as spikes, polyspikes, spike and waves, sharp waves, sequences of fast oscillations, etc.

(Figure 1.1). IEDs have to be differentiated from non-epileptic sharp waves. The Non-epileptic sharp waves are irregular, express a complex morphology with longer duration and smaller amplitude than IEDs (De Curtis & Avanzini, 2001). The variability of IEDs pattern suggests that they might be related to different neurological mechanisms and with different functional roles in the epileptic tissue. The following definitions are in use (Chatrian, 1974):

I. *Sharp wave*: Its pattern is transient and completely different from the background, with a strong peak and a duration of 70-200 ms.

II. *Spike:* Its properties are like a sharp wave, but it has a duration of 20-70 ms.

III. *Spike-and-slow-wave complex:* Its pattern consists of a spike followed by a slow wave (classically, the slow wave has a higher amplitude than the spike).

IV. *Multiple spike-and-slow-wave complex:* It is like spike-and-slow-wave complex but has two or more spikes associated with one or more slow waves.

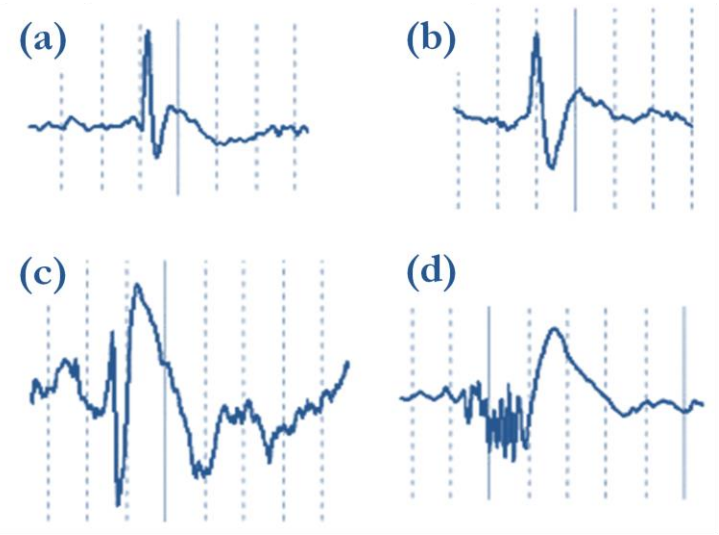

Figure 1.1. Patterns of Interictal epileptic discharge (IED): (a) Spike, (b) Sharp wave, (c) Spike-and-slow-wave, (d) Multiple spike-and-slow-wave.

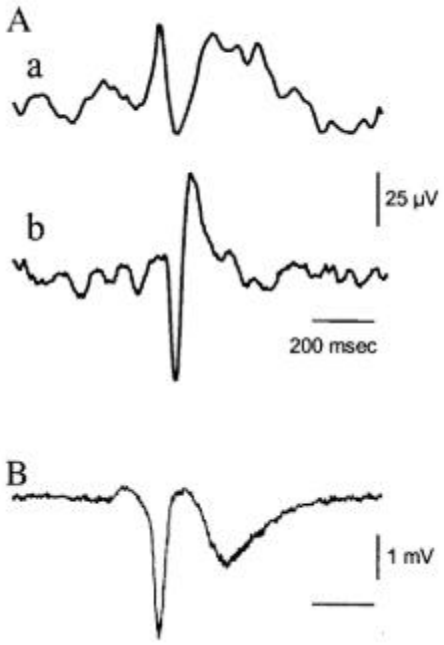

Figure 1.2. Interictal spikes (IISs) recorded (A) in human (a) focal lesional epilepsy and (b) focal idiopathic epilepsy with scalp EEG electrodes and (B) in an experimental in vitro model of focal epileptogenesis recorded extracellularly (from De Curtis et al. 1999).

The recorded IED proximal to the sources are assumed to be produced by synchronous neuronal firing of a large population of neurons (Figure 1.2). The mechanism underlying the IED became one of an attractive issue in the epilepsy. In the different periods related to the IED, the period that would produce the first burst of neuronal excitation in the IED, might be due to a recruitment of neurons through synaptic excitations that would reach the threshold of regenerative calcium currents (Chamberlin *et al.*, 1990; Ives & Jefferys, 1990).

Bursting neurons have been observed in deep layers of the neocortex during the interictal spikes (IISs) (i.e. CA1-CA3 of the hippocampus, piriform cortex, entorhinal cortex) (De Curtis & Avanzini, 2001) (Hoffman & Haberly, 1991; Fountain *et al.*, 1998). The NMDA and AMPA glutamate receptors subtypes participate in the excitatory postsynaptic potentials in IISs (Traub & Wong, 1982). The bursting activity is controlled by a $GABA_B$ receptor-mediated inhibitory synaptic potential (De Curtis *et al.*, 1999).

Changes in conductance can be related with the bursting discharges and paroxysmal depolarization shifts (PDSs)(De Curtis & Avanzini, 2001). The PDS is the intracellular correlation of IIS, it can be triggered by the accumulation of excitatory synaptic potentials mediated by glutamate receptors (Chamberlin *et*

al., 1990; Hoffman & Haberly, 1991) or by the release from inhibition. During the IIS, the calcium spikes participate in the elaboration of the PDS as it has been shown with the application of a calcium channel blocker which remove or reduce the occurrence of seizure (Figure 1.3) (De Curtis & Avanzini, 2001).

Non-synaptic interactions participate in the neuronal synchronization during the IIS through changes in the extracellular electric field and intracellular gap junctions between neurons or interneurons (de Curtis *et al.*, 2012). Due to the increase of the neuronal excitability, the number of spontaneous firing neurons might be increased, the extracellular space surrounding neurons and the ion concentration (calcium and/or sodium) might be modified.

Current studies support that inhibitory networks have an essential role in the spontaneous IIS (de Curtis *et al.*, 2012; De Curtis & Avoli, 2016; Saillet *et al.*, 2016). Synchronous neuronal activation facilitated by inhibition mechanisms was suggested in some studies for generating spike-and-wave IIS patterns (De Curtis & Avanzini, 1994; Pinault *et al.*, 1998). This synchronous activation in principal cells is characterized as a rebound response to a brief hyperpolarization from the GABAergic cells (Cobb *et al.*, 1995). The interaction between them (i.e. Principal and GABAergic cells) can induce fast cortical frequencies in the gamma range and HFO (100 – 500 Hz)occurring a few milliseconds before the PDS or the spike onset (Buzsáki & Chrobak, 1995; Fisahn *et al.*, 1998).

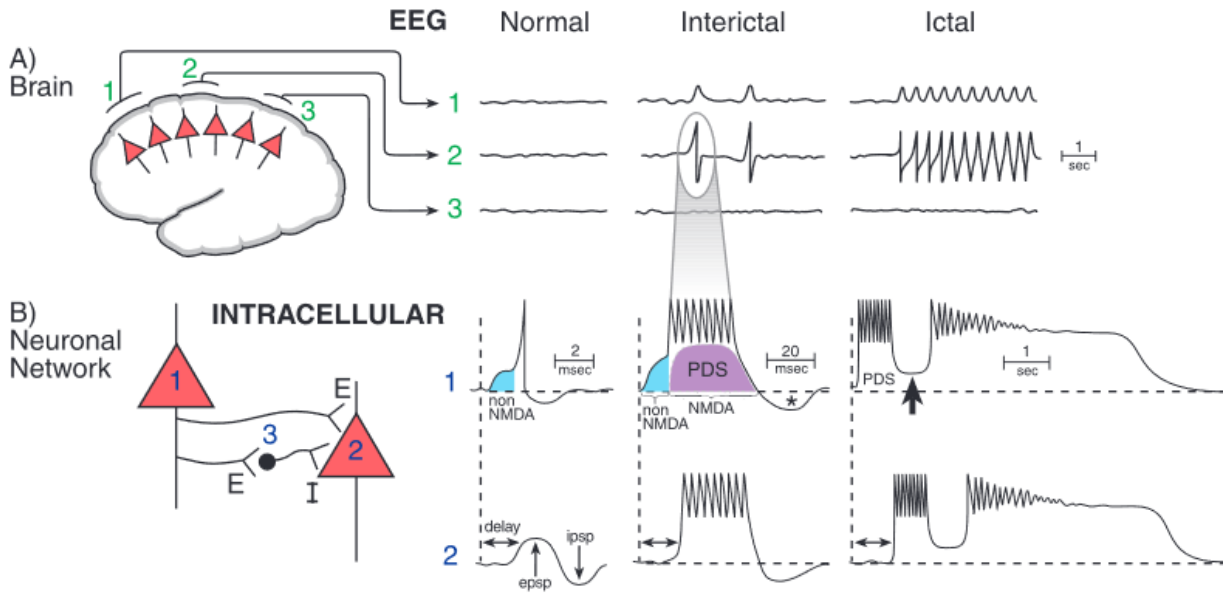

Figure 1.3. Representation of the abnormal neuronal firing recorded at the neocortex by EEG and intracellularly. A) Three simplified EEG signals from different neocortical regions of the brain at three different epileptic periods (normal, interictal and ictal). B) Two intracellular signals from pyramidal neurons. The intracellular signals show a paroxysmal depolarization shift (PDS) related with the IISs present at the EEG in both neurons (from Stafstrom 1998).

1.1.1.4. Animal models in epilepsy research

The IIS suggest is not a simple paroxysm of excitatory activity. It results from complex mechanisms at the cellular, network levels, involving different types of neurons (Faingold, 1999). The cellular and network interaction mechanisms occurring together with IIS have been studied in different epileptic models: in human (in vivo/in vitro), in animal (in vivo/ in vitro) and in computational models.

The animal model has been used in epilepsy research from the last century to better define the basic mechanism related to epilepsy. To consider an animal model as an ideal model of epilepsy it must be as close as possible to a human type of epilepsy. This means if the focus of the study is the seizures, the animal model needs to present the symptoms as seen in human, like generalized or focal epilepsies, with absences or convulsive behavior. In case of studies focusing on IED a large interictal period between the seizures is mandatory and the IED should look similar to those recorded in human (Marsh *et al.*, 2010).

1.1.1.4.1. Models of IEDs

Using a wide variety of methods such as electrical excitation or the use of drugs, the balance that exists between the different neurotransmitters in the cerebral cortex can lead to greater excitability,

triggering epileptic spikes or seizures. In experimental animals, the typical methodologies used for the replication of extracellular IED and intracellular PDS are described below:

I. Using drugs that:
   a. Interfere with GABAergic inhibition mechanisms: penicillin, bicuculline and picrotoxin (Matsumoto & Marsan, 1964; De Curtis *et al.*, 1999).
   b. Increase GABAergic and glutamatergic synaptic transmissions: potassium blocked 4-aminopiridine (Szente & Baranyi, 1987).

II. Using solutions:
   a. That improves the neuronal excitability: high potassium model, low-magnesium model or low-calcium model (Anderson *et al.*, 1986).
   b. That improves the glutamatergic transmission: kainic acid (Ashwood *et al.*, 1986).

III. Using electrical stimulations: protocolized and repeated electrical stimulations (McIntyre & Wong, 1986).

Models of epilepsy have been developed *in vitro* (brain slices) and *in vivo* (chronic and acute protocols). The *in vitro* model corresponds to a more controlled condition and is used to evaluate the effect of neurotransmitters more precisely at the cellular level. This option (i.e. *in vitro*) has a limitation due to the loss of functional circuitry surrounding the tissue (Barkmeier & Loeb, 2009). In the in vivo model the brain is analyzed as a complete system. The IED can be triggered immediately using focal or systemic doses of pilocarpine, kainic acid, $GABA_A$ blockers (as penicillin or bicuculline) or electrical stimulations (Barkmeier & Loeb, 2009). The use of drugs as kainic acid or pilocarpine produce systematically spontaneous seizures mixed with periods of IED (Williams *et al.*, 2006; Duarte *et al.*, 2010). GABAergic blockers can produce, in a single dose, focal IED for 6 to 8 hours (Holmes *et al.*, 1987).

The IED can also be triggered by initial lesion of the brain, corresponding to chronical lesional models (Gasteiger *et al.*, 1985). Other chronical models can be produced by the electrical repetitive stimulations or after applying solutions of toxic metals or tetanus toxins on the neocortex (Gotman, 1984; Mathern *et al.*, 1994).

1.1.1.4.1.1. Penicillin model

The penicillin can be administrated intracorticaly, intramusculary, intraperitonealy or intravenously (Dragic & Pavlovic, 2004). In the cortex, the penicillin is commonly injected mechanically with the use of a glass micropipette.

The first report of the penicillin model was published in 1945 (Walker, 1945). The penicillin model is characterized by (Edmonds *et al.*, 1974; Dragic & Pavlovic, 2004):

a. Penicillin produces IIS or seizures in a wide variety of vertebrates.
b. Production of IIS or seizure begins rapidly (15 mins) and continues for some hours.
c. Cytoarchitectural changes after penicillin application are rarely found.
d. The amount of penicillin applied is related with the spread's degree of the abnormal activity.
e. Penicillin-induced seizures are not resistant to anticonvulsant agents.
f. The induced epileptiform activity disappears after 24 hours.

1.1.2. The neuro vascular system

The human brain is made of about 86.1 ± 8.1 billion of neurons and 84.6 ± 9.8 billion of non-neuronal cells. Only 19% of them are located in the cerebral cortex. This percentages are not far from other primates' ratios (Figure 1.4). The neocortex neurons are principally located in a small area (~2.5 mm thickness) called grey matter (Fischl & Dale, 2000). The communication between all the neurons of the brain occurs via synapse interactions combining electrical and chemical interactions propagated through the neuron's axons (Attwell & Laughlin, 2001). It is calculated than the number of synapse in the human brain can approximate 160 trillion (Nguyen, 2010). This synaptic communication rely on 50% of the brain's energy, which is provided by oxygen and glucose supply through surrounding blood vessels (Duvernoy *et al.*, 1981; Attwell & Laughlin, 2001).

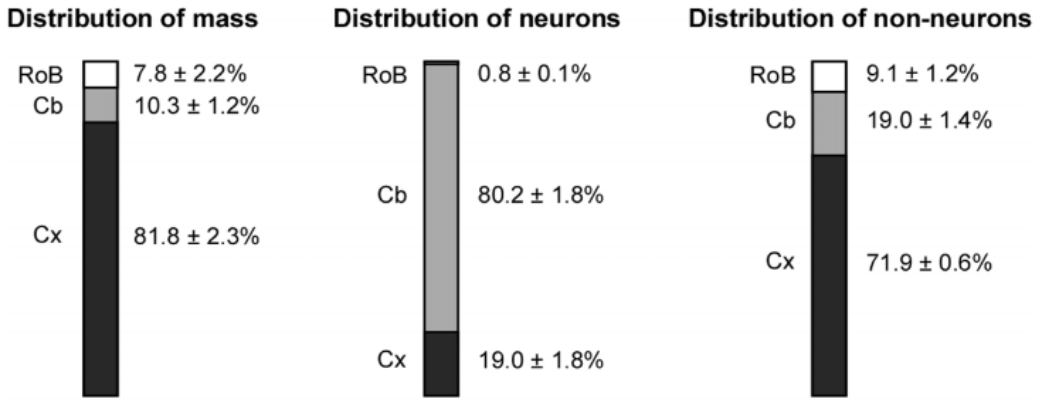

Figure 1.4. Graphical representation of the mass, the neurons, and the non-neuronal cells distribution in the adult human brain. Each vertical bar represents the percentage of cells located in the cortex (Cx, black bar), cerebellum (Cb, gray bar), and remaining areas of the brain (RoB, white bar).Values are mean±SD (from Azevedo et al. 2009).

The arteries and arterioles penetrate the neuronal layers to supply neurons with oxygen. Thicker smooth muscle is organized along the vessel walls to principally maintain the tone of the blood pressure fluctuations and to provide an active vasomotion. A major density of arterioles is present in zones involved in processing of information (Herkenham, 1980; Weber *et al.*, 2008). After providing the neural tissue with oxygen (95-100% oxygen saturation) and nutrients, the capillaries convert into venules to flow the low oxygenated blood (60% oxygen saturation), enriched with carbon dioxide and cellular waste toward the larger veins (Duvernoy *et al.*, 1981).

1.1.2.1. Compartments

The neurovascular system is formed by a dynamic structure based on (1) the neuronal and astrocytes compartment on one side and (2) the vascular compartments with vessels surrounded by the vascular endothelium cells and the pericytes and (3) the extracellular components. The neurovascular unit is made of a quadripartite synapse which includes, the neurons, the vessels, the astrocytes, and the extracellular space. It has the role of maintaining the optimal and adequate level of oxygen and nutrients to the brain (McAdams & Juul, 2012; Kratzer *et al.*, 2014; Moretti *et al.*, 2015). The astrocytes play a key role in the brain-blood-barrier (BBB) regulation to provide nutrients and regulate the neuronal synapses (Petzold & Murthy, 2011).

1.1.2.1.1. Neurons

The neurons send and receive codified information via specialized connections called synapses. Neurons are observed in all the animals there is a wide variety in their shape, size, and electrochemical properties (Figure 1.5). The neurons are commonly classified depending of the morphology or functionality.

1.1.2.1.1.1. Morphological classification

Neurons have the most diverse and complex morphology of all cells in the body. Neurons are divided into three compartments: soma, dendrites, and axon. The size and shape of the soma, the density and shape of the dendrites, as well as the arrangement, length, and branching pattern of the axons variates for each type of neuron.

The soma or neuronal body can be highly variable, being pyramidal, spherical, stellate, fusiform or basket-shaped. The average size of a neuronal cell is about 20µm, although it can vary depending on the type of neuron.

Three major groups arise from the morphological classification: multipolar, bipolar, unipolar, and pseudo-unipolar neurons. The unipolar neurons just have a single process, that only exist in invertebrate animals; Pseudo-unipolar neurons may appear to be unipolar, the truth is that there is a bifurcation at the tip of the axon, they are the most common neurons in the sense of touch and pain perception; Bipolar neurons has one axon and one dendrite which can be found, for example, in the retina, cochlea and olfactory mucosa; Multipolar neurons are defined as having two or more dendrites that extend out from the soma. The multipolar neurons, in humans, are the most common neurons by far.

1.1.2.1.1.2. Functional classification

Neurons can be classified according to their function in the nervous system. In this classification, it is relevant in which direction the neuronal signal is transmitted, in relation to the central nervous system (CNS). There are three types of neurons: motor neurons, sensory neurons, and interneurons.

- *Sensory neurons* (or afferent) neurons send information from the sensory receptors toward the brain for processing. Almost all sensory neurons are pseudo-unipolar.
- *Motor neurons* (or efferent) transmit information away from the CNS toward some type of effector. Motor neurons are typically multipolar.
- *Interneurons* are placed between motor and sensory pathways and are highly involved in signal integration. Most interneurons are in the CNS.

Synapses are cellular structures where information is exchanged between two neurons. Both the neuron that emits the information (presynaptic neuron) and the one that receives it (postsynaptic) participate in them. There are two types of synapses in the nervous system: chemical and electrical. Electrical synapses are gap junctions that are established between two contiguous neurons. They are much less common than chemical synapses and have no need for neurotransmitter mediation. The neurotransmitters are chemical messengers, they can be amino acids such as glutamate, gamma-aminobutyric acid (GABA) or aspartate; monoamines such as dopamine, serotonin or adrenaline; polypeptides such as somatostatin, neuropeptide Y, or substance P; but there are also other types of neurotransmitters such as acetylcholine, adenosine or taurine.

Depending on the effect of synaptic contacts, there are categories of neurons: inhibitory, excitatory, and neuromodulator neurons that influence neurotransmission.

Excitatory neurons are neurons whose synapse causes the next neuron in the network to activate and continue to transmit an electrical impulse to continue sending the message. That is, they are the neurons that produce neurotransmitters that act as "triggers" for the functionality of the next neuron. They are the main neurons in transmitting information both from the sensory organs to the CNS and from the brain to the organs and motor tissues.

Inhibitory neurons are neurons whose synapse causes the next neuron in the network to remain inactive or to cease to be excited. Inhibitory neurons are those that produce neurotransmitters that act as “calming” for the following neurons, that is, they slow down their activity or prevent them from becoming excited.

Neuromodulator neurons neither excite nor inhibit the functionality of other neurons, but rather regulate the way in which they synapse. That is, they "control" the way in which the other neurons communicate with each other. An example of a neuromodulator is norepinephrine. By itself, norepinephrine has little effect on synaptic transmission, but when a neuron is exposed to norepinephrine first, it will react more powerfully to glutamate.

The two most common (>90%) neurotransmitters in the brain are glutamate and GABA (Sanzone, 2011). Glutamate has effects that are excitatory at ionotropic receptors and a modulatory effect at metabotropic receptors. GABA have inhibitory effects on several types of receptors. It is usual to refer to neurons that release glutamate as "excitatory neurons", and neurons that release GABA as "inhibitory neurons". Two distinctive neuronal types of excitation and inhibition in the CNS are pyramidal neurons and inhibitory interneurons.

The pyramidal neuron is a type of multipolar neuron with single axon, large apical dendrite, and several basal dendrites. Pyramidal cells are the most populous excitatory neuron type in the mammalian cortex and receive both excitatory (glutamatergic) and inhibitory (GABAergic) inputs (Fröhlich, 2016). Higher populations of pyramidal cells are found in the corticospinal tract and in the prefrontal cortex. In the motor system, they convey output information’s from cortical layers to medullar motor neurons through the cortical tract (Salimi *et al.*, 2008). In the prefrontal cortex they are responsible for receiving and processing all the inputs received from all sensory modalities, playing a crucial role in the recognition of objects in the visual processing areas of the cortex (Elston, 2003).

Inhibitory interneurons project locally and shape the neural networks function throughout the brain using inhibitory neurotransmitters (GABA and glycine). They present a complex connectivity within the

neural network (Figure 1.5). They also elicit micro-vessel diameter changes producing a vascular response (Cauli *et al.*, 2004; Saillet *et al.*, 2016). Dysregulation of interneurons may lead to neurodevelopmental disorders (Lunden *et al.*, 2019).

Microcircuits are critical for the function of the cortex (Lunden *et al.*, 2019). The glutamatergic pyramidal neurons are dedicated in sending information within cortical areas and to other parts of the brain. Inhibitory GABAergic interneurons regulate the activity of these pyramidal cells. These interneurons participate in the regulation of gating in spiking, temporal, and spatial network dynamics (Vogels & Abbott, 2009), as well as features of the waking brain state (attention, arousal, and the regulation of pupil diameter) (McGinley *et al.*, 2015).

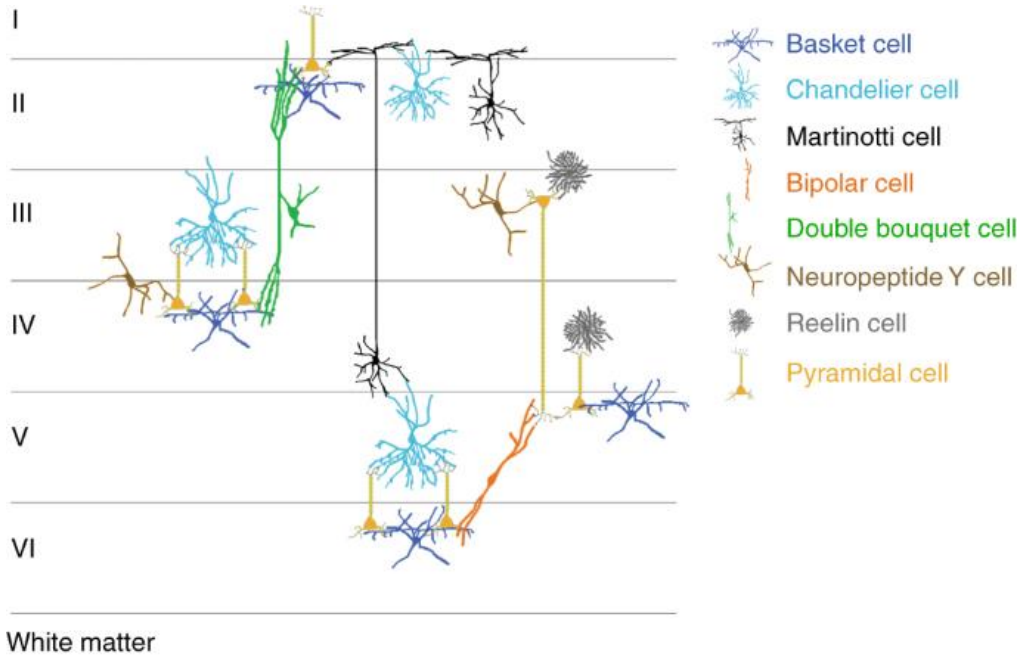

Figure 1.5. Some neuronal types and their connections within the cortex, including their frequent laminar location at the cortex (from Lunden et al. 2019).

1.1.2.1.2. Astrocytes

The astrocytes are responsible for the maintenance of neural function, intertwining around the neurons to form support networks and act as a filtering barrier between the blood and the neuron. The astrocytes play a central role, in the neurovascular coupling, to convey the neuronal activation to the blood vessels, evoking changes in blood flow (Petzold & Murthy, 2011).

Astrocytes can detect different molecules released by neuronal synaptic activities into the extracellular spaces (e.g. K+, Na+, Ca++, ATP, glutamate, GABA, acetylcholine (ACh)) which might

participate in vasodilatation. The astrocytes can also release some molecules and be affected by the oxygen supply that could produce vasoconstriction (Gordon *et al.*, 2008). Astrocytes are not considered as neurons providing primary and secondary current. They do not produce EEG changes when solicited.

The transmission of electrical signals in astrocytes occurs thanks to the IP3 messenger molecule and calcium. IP3 activates calcium channels in cell organelles, releasing it into the cytoplasm of the astrocyte. Calcium ions are therefore essential for communication between astrocytes, increasing glucose consumption as well as vasodilation (Mishra *et al.*, 2016). The calcium ions stimulate the production of IP3 and the net effect is an electrical wave that propagates from astrocyte to astrocyte. The propagation of calcium waves is mediated via repetitive diffusion of IP3 or via the release of ATP as a extracellular messenger activating IP3-coupled metabotropic purinoreceptors (Volterra & Steinhäuser, 2004). Astrocyte end-feet are in contact with the cerebral arterioles regulating the flow of nutrients and oxygen and producing vasodilatation (Figure 1.8). The calcium waves stimulate some vasodilatation pathways as following: the increase of arachidonic acid, adenosine from ATP, changes in K+ concentration and synthesis of prostanoids (Figure 1.6)(Paulson *et al.*, 2010).

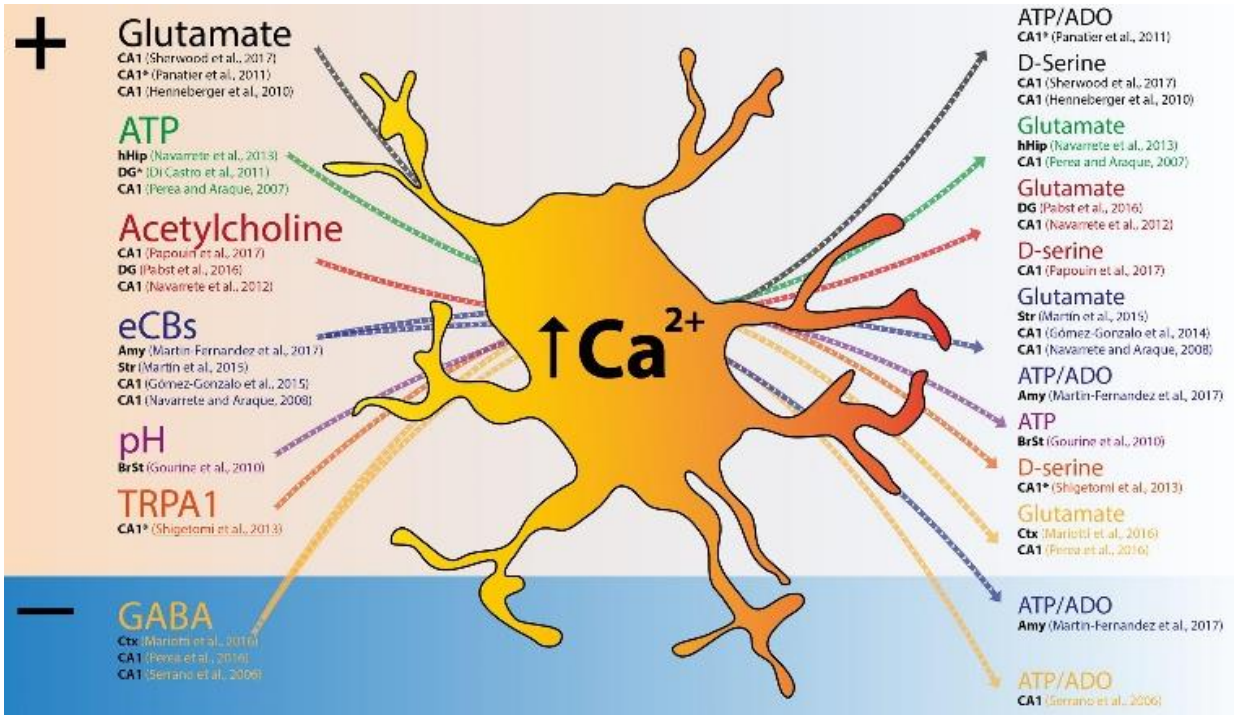

Figure 1.6. Scheme showing input signals that cause astrocyte Ca^{2+} elevations and respective gliotransmitter release. Both excitatory (+) and inhibitory (–) signals trigger global or focal Ca^{2+} increase in astrocytes (left side) and lead gliotransmitter release that excites or inhibits the neighboring synapses (right side) (from Guerra-Gomes et al. 2018).

1.1.2.1.3. Endothelial cells

The endothelial cells (Figure 1.7) are the first barrier between the vessels and the tissue and participate in fluid filtration. Surrounding the endothelium are the smooth muscles which can produce changes in the vascular diameter by relaxing or contracting effects. Substances as ACh and adenosine causes a release of vasodilator nitric oxide (NO) by the endothelial cells, that lead to a relaxation of the vascular smooth muscle (Ignarro *et al.*, 1999).

1.1.2.1.4. Pericytes

Pericytes are cells located around the endothelial cells acting as mural cells regulating the microcirculation at the capillaries and the venules levels (Figure 1.7) (Dore-Duffy, 2008). Pericytes are rooted in basement membrane, where they communicate with endothelial cells by direct physical contact and paracrine signaling (Bergers & Song, 2005). These cells can maturate in endothelial cells and vascular smooth muscle in the conjunctive tissue. They participate in the maintenance of the local homeostasis and hemostasis (Dore-Duffy, 2008). They constitute a key factor of the neurovascular unit. The pericytes are identified as essential contributor in the regulation of the cerebral blood flow. Their capability of vasoconstriction has been demonstrated (Peppiatt *et al.*, 2006). The distribution of pericytes thorough the brain seems higher in childhood than in adulthood (Diaz-Flores *et al.*, 1991).

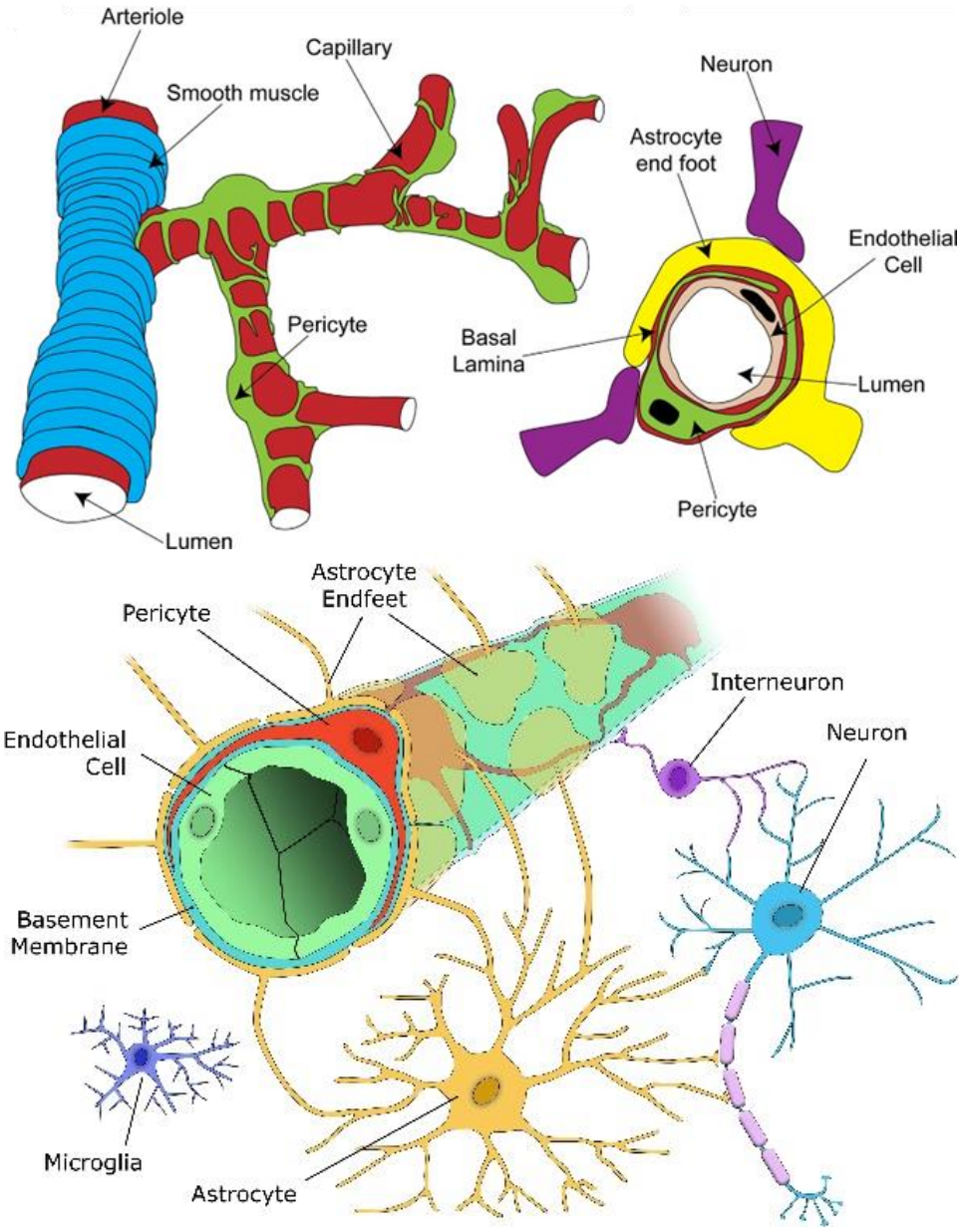

Figure 1.7. Schema of the compartments of the neurovascular system (from Brown et al. 2019)

1.1.2.2. Neurovascular coupling

It is known that neural and vascular systems in the brain constitute two halves of the same functional unit in which interactions are supported by the concept of the neurovascular coupling (NVC): Changes in regional blood flow occurring in response to an increase in the demand of metabolism in the same region related to an increased neuronal activity.

Living systems are experts in energy conversions. Animal cells activity is related to aerobic mitochondrial metabolism, anaerobic glycolysis and net lactate extrusion. In normal conditions, the main

energy source of the brain is the oxidative process of glucose (Glucose + $6O_2 \rightarrow 6CO_2 + 6H_2O$ + energy) (Siesjö, 1978).The efficiency of the oxidative pathway in terms of energy obtained from glucose is approximately 40% (Blanco & Blanco, 2017). The cerebral metabolic ratio of oxygen ($CMRO_2$) is around 6 times the cerebral metabolic rate of glucose consumption (CMRglc). The principal supplier of oxygen is the blood and the glucose which can be stored by the astrocytes. Neural energy therefore depends on the glia and the correct blood supply to develop a normal activity.

New methods for measuring CBF were introduced in the 1960s, allowing to characterize the increase in CBF in relation with the increase in brain activity (Lassen *et al.*, 1978). Subsequent studies showed that the direct relationship between increased activity and increased in CBF is more complex (Fox & Raichle, 1986; Mintun *et al.*, 2001). Nevertheless CBF is not directly related to an increase in CMRO2 (Fujita *et al.*, 1999; Okazawa & Vafaee, 2001). It has been subject of numerous studies to determine if exist a coupling relationship between CBF and $CMRO_2$ during neural stimulation, both in humans and in animal models (Nourhashemi *et al.*, 2016; Mahmoudzadeh *et al.*, 2017), pointing out that the relationship is possibly between CBF and CMRglc, and not so much with $CMRO_2$. New evidences supports the functional attempt to accommodate the cerebral tissue's increased demand for glucose supply during neural activation with a crucial role of astrocytes in rCBF regulation (Paulson *et al.*, 2010).

1.1.2.2.1. Dynamic models of neurovascular coupling in epilepsy

Dynamic models are being used to explain the mechanisms observed between the different elements that set up the neurovascular unit. These models aim at modeling the concentration changes in hemoglobin (reduced or oxygenated) in response to neuronal activation. Two common dynamic models for NVC are described below.

- *Balloon model:* The balloon model includes the blood oxygenation and volume changes coupled with the blood flow and oxygen consumption at the activity periods. The model assumes a no capillary recruitment and volume changes in venous compartment (negligible in arteriolar compartment). The name of balloon is taken from the fact that in the vascular compartment there is a dilatation in the venous part (whose shape resembles a balloon) (Buxton *et al.*, 1998).

- *Windkessel model*: The Windkessel model is based on the observed mismatch between regional cerebral blood flow (rCBF) and relative cerebral blood volume (rCBV). This model considers the compliance capacity of the capillaries and veins to passively regulate the pressures generated by the dilation and contraction of the arterioles. The vasomotor control of arterioles determines the

rCBF provoking 70% of the vascular resistance. Around 80% of CBF is controlled by capillaries and veins (Mandeville *et al.*, 1999).

1.1.2.2.2. The effect of IISs on neurovascular coupling and cerebral blood flow

The increase in neural activity related to changes in hemoglobin concentrations has been largely described. Studies performed with functional magnetic resolution imaging (fMRI) and spectrometry measurements on NVC in both epileptic patients and epileptic animals have shown that the duration and frequency of epileptic events modulate the hemodynamic changes (Osharina *et al.*, 2010, 2017; Gotman & Pittau, 2011). Similar findings were reported for CBF in laser Doppler flow (LDF), showing an increase in CBF secondarily to IIS (Saillet *et al.*, 2016). Other studies have verified hemodynamic changes in oxyhemoglobin (HbO_2) and deoxyhemoglobin prior to IISs (5-6s) in humans and rodents using functional near-infrared spectroscopy (fNIRS) (Osharina *et al.*, 2010, 2017; Wallois *et al.*, 2010) and fMRI (Hawco *et al.*, 2007; Jacobs *et al.*, 2009; Gotman & Pittau, 2011), suggesting that not only a NVC linked to IISs exists but also some early hemodynamics changes occurring before the IIS which might account for the hypersynchronization onset that built up the IIS.

1.1.2.2.3. The pre-spike period

The changes seen in the pre-spike period (-5 s before IIS onset) is characterized by a significant decreases in HbO_2/HbT concomitant with significant increases in HbR (Osharina *et al.*, 2010, 2017). These changes may reflect the activation of different parts of the neuronal populations, which would cause NVC by the participation of neurotransmitters, vasoactive molecules, ion pumps and gap junctions.

The GABA interneurons, astrocytes, vasoactive interneurons could mediate the pre-spike hemodynamic changes due to their localization and connection to the microvessels (Gordon *et al.*, 2011; Lecrux & Hamel, 2011).

The decrease in HbO_2/HbT concentration might reflect a local vasoconstriction followed by a decrease in rCBF. In the animal models using GABA antagonists this vasoconstriction could be explained partially by the mechanisms used in the GABA blockage (Kocharyan *et al.*, 2008).

The pre-spike period raises many questions due to its complex interactions that can be observed in hemodynamic changes, for example, if these interactions would be treated just with the early detection of these changes in order to somehow alleviate the IIS activity on the way. Overall, exist postulates that the pre-spike hemodynamic changes probably support the concept of neurovascular coupling leading to spiking activity (Stanimirovic & Friedman, 2012; Osharina *et al.*, 2017).

1.1.3. The extracellular space during IIS

Some non-synaptic changes might contribute to produce or maintain the IISs. Changes that facilitate the neural activation observed during IISs are the neural activation itself, causing neuronal and glial swelling that reduce the extracellular spaces (McBain *et al.*, 1990; Andrew & Macvicar, 1994) which might facilitate ephaptic conduction between neurons. These neuronal and glial swelling produce a shrinking of the extracellular space, inducing an increase of the $[K^+]$ in the extracellular space (Jensen *et al.*, 1994, 1996) during the IISs (De Curtis *et al.*, 1998), enhancing membrane depolarization and intrinsic burst firing by the falling of ionic transmembrane driving forces during the activation of repolarizing potassium conductance and by shifting the reversal potential of inhibitory synaptic potentials toward more positive values (De Curtis & Avanzini, 2001). Some studies have validated the idea that such cellular swelling can modify photon scattering and consequently be evaluated by fast-optical signal (FOS) technique, which have high temporal resolution (Gratton & Fabiani, 1998). The efficiency of this methodology to monitor changes in membrane configuration during IISs has been demonstrated (Manoochehri *et al.*, 2017). These authors observed decrease-increase-decrease in light scattering surrounding the IIS and starting few hundreds of milliseconds before the IIS, suggesting a shrinking-swelling-shrinking sequence in the neuronal population resulting in an increase-decrease-increase of extracellular space from -300 to +300 ms from the IIS maximum EEG peak.

1.1.4. Combining neuroimaging studies

There are a multitude of studies that combine multiple techniques to understand the relationship between hemodynamic / electrical changes related to neural activation. Different techniques such as EEG, ECoG, local-field potentials (LFP), and magnetoencephalography (MEG) are developed to record electrophysiological events related to neuronal activity. They are based on the depolarization and repolarization of the membrane of neurons related to the exchange of ions with the cellular environment, producing a recordable electric current. They temporarily have a high resolution (on the order of milliseconds). In practice, to record the neuronal electrical activity, non-invasive recordings, such as EEG, are normally chosen, which entail less precise spatial resolution than, for example, the use of ECoG, which is normally reserved for brain surgeries.

Functional magnetic resonance imaging (fMRI) is used to detect changes in the magnetic resonance signal associated with deoxygenated hemoglobin concentration changes (Van Horn & Poldrack, 2009). To measure $CMRO_2$, rCBF, glucose (rCMG) and rCBV, positron emission tomography (PET) is used. These techniques have many advantages including high spatial precision but low temporal precision. Other

disadvantages of these techniques are (1) the high cost (2) the difficult accessibility, (3) the restriction of movements (important for epilepsy), (4) the absence of monitoring, (5) the noise and (6) the discomfort for long scanning.

A combined spatiotemporal approach is nevertheless necessary to better understand the mechanisms underlying the different neuronal, hemodynamic and extracellular space dynamic that propel an assembly of neurons to aberrantly synchronize toward the IIS discharge. It is therefore mandatory to develop a multimodal multiscale approach that allows to simultaneously scan the different compartments. The NIRS is a portable method and a low-cost alternative for MRI or PET. It can be used combined with EEG, ECoG and LFP recording to understand the mechanisms that propels neurons to epileptic synchronization. Each electrophysiological combination (EEG, ECoG or LFP) with NIRS provide a useful data but at different scales. The surface EEG records electrical field resulting from depolarizing or hyperpolarizing currents at the dendrite of well orientated synchronized pyramidal cells at approximately 1cm of depth from the surface. The ECoG record the electrical fields resulting from post-synaptic potentials at approximately 1mm of the cortical surface. The LFP signal reflects the sum of unit activities within approximately 50-350 µm from the tip of the electrode (Gray *et al.*, 1995) and slower ionic events from within 0.5–3 mm from the tip of the electrode (Juergens *et al.*, 1999).

Table 1.1. Brain imaging common techniques.

Imaging Method	Time Resolution	Spatial Resolution	Source of signal	Invasive	Price
fMRI	>1s	2 mm	Para-magnetism of Deoxy-hemoglobin	No	High
PET	>10s	4-6mm	Tracers in blood used to measure oxygen/glucose metabolism	Yes	High
Surface EEG	ms	Approx.1cm	Post-Synaptic Potentials	No	Low
ECoG	ms	<1 mm	Post-Synaptic Potentials	Yes	High
MEG	<1 ms	2-3 mm	Weak magnetic fields (10-14 Tesla) produced by brain activity	No	High
NIRS	>1s ms	Approx.1cm	HbO_2/HbR changes (slow optical signal) Neuronal changes (fast optical signal)	No	Low

1.2. Objective and contributions of this thesis

This thesis aims at analyzing the different mechanisms that propels the neurons to an aberrant epileptic synchronization by developing a combined multimodal multiscale approach of the neuronal, hemodynamic, and extracellular space compartments. To fit this purpose, we developed a combined ECoG, LFP and Multiunit activity (Neuronal), NIRS and diffuse correlation spectroscopy (DCS) (hemodynamic) and fast optical signal (extra cellular space) recordings. This approach allows to address (1) the activation of a large assembly of neurons (ECoG) (2) the single and multi- unit activity (UA and MUA), (3) the neurovascular coupling (NIRS, DCS) and the changes in the extracellular space (FOS) occurring around the IIS. Because of their high temporal resolutions, these technics allows to monitor the changes observed during the pre-spike, the spike, and the post-spike periods.

1.2.1. Contributions

General visions of the principal contributions of this thesis are the following:

- To develop an animal model that allows simultaneous measurements of: (1) the electrophysiological activities including electroencephalogram (EEG), local field potentials (LFP), multiunit and unit activities (MUA and UA) (2) hemodynamic changes (fNIRS and DCS) (3) changes in the extracellular space (FOS).
- To analyze the dynamic of the different compartments to better understand the mechanisms that propels neurons to hypersynchronization during IIS.
- To evaluate the dynamic of the non-synaptic and the vascular compartments together with the synaptic activities.

1.3. Thesis overview

In *Chapter 1*, I made a brief introduction on epilepsy, including epidemiology, history, and classification to introduce the IIS animal model. In the following points, I described briefly the current knowledge about the neuronal and the vascular compartments dynamic related to the interictal epileptic discharges. I then described briefly the main mechanisms of the neurovascular coupling and abouts what is currently known concerning the pre-spike period of the IIS. Finally, Other perspectives such as the changes in the extracellular space during IIS were briefly reviewed.

In the following chapters, I am going to present my thesis, with the intention of evaluating all the changes that may be related to IIS, including approaches to the analysis of electrophysiological data (ECoG, LFP, UA and MUA), such as optical imaging (fNIRS y DCS), placing special emphasis on the pre-IIS periods to investigate how they are generated.

Chapter 2: Material and methods. In Chapter 2, I made an overview of the different systems used to carry out a multimodal study on IIS. The main knowledge about each methodology have been briefly described: (1) to record bioelectrical activities such as ECoG and MLE, (2) to record neural structural changes (FOS), (3) to record hemodynamic activity (fNIRS) and (4) to record cerebral blood flow (DCS).

Chapter 3: Results: What trigger the interictal epileptic spike? A multimodal multiscale simultaneous analysis using ECoG, MUA, NIRS, DCS and FOS in rats. Chapter 3 presents the main results of the thesis which is under review in *Frontiers in Neurology*.

Chapter 4: Conclusions and perspective. In the last chapter I summarized the principal conclusions and future perspectives for future research.

CHAPTER

2

Material and methods

2.1. Introduction

The neural populations have multiple biological ways involved in their normal or abnormal behavior. Electrophysiological technics were used in order to record the bioelectrical activity like electrocorticogram (ECoG) and multisite linear electrodes (MLE) recordings, also other technics were used to record the neural structural changes (Fast-Optical Signal, FOS), hemodynamic activity (Near-Infrared Spectroscopy, NIRS) or blood flow (Diffuse Correlation Spectroscopy, DCS). Neural systems require a multimodal methodology for a well understanding of *in vivo* activities.

In our experimental protocols, we follow the previous idea, including more than one method in the recordings, so our data requires more steps to be processed correctly. For that reason, a review of the material and methods of our designed recording setup is necessary for a well understanding of the results and their limitations.

The next sections of this chapter explain in more detail all the applied technics, including their bases and schemas for each setup of recording. After those sections, it is presented the processing and analysis of the data for each modality and how the systems are synchronized. The last part of this chapter presents the difficulties that appeared during the thesis' period related to the systems.

2.2. Electrophysiological system

2.2.1. Fundamental elements for electrophysiological systems

Electrophysiology is part of physiology which studies the flux of ions through any biological tissue. To record the ion flux, the electrodes are the first fundamental part to acquire the bioelectrical activity. In an attempt to have useful data, the recording of biological tissue usually needs to be amplified before the acquisition (Scanziani & Häusser, 2009). Amplification emphasizes the desired signal versus the background noise; the correlation between these two signals is called the signal-to-noise ratio (SNR).

2.2.2. Electrodes

The characteristics of electrodes are essential depending on the goal of the study. The activity of neural populations can be recorded at the scalp or in direct contact with them, according to the electrode's features (Thompson & Patterson, 1973). Materials, shape, and size are related to the functionality (Buzsáki, 2004; Kolb & Whishaw, 2009). For example, one ECoG-electrode is not the best electrode to record an electrocardiogram (ECG) or electromyogram (EMG) activity. Some electrodes to record specifics for neural activities are:

- *Based on solid conductors*: Depending of the purpose, the electrodes are created in different shapes, sizes, and materials. These electrodes are insulated except for the recording site. Some of them can be implanted inside living tissues. It can be used to record long field potentials or unit activity, and also, they can form tetrodes to record close sites inside the neuronal tissue (Dowben & Rose, 1953; Hubel, 1957; Buzsáki, 2004).
- *Empty and thin tubes filled with electrolyte solutions*: One of the most used in the neural recordings are the glass pipette tubes filled with some electrolyte solution (Wolbarsht *et al.*, 1960). This electrode allows to recording intra- and extracellular single-unit activity, patch-clamp, and more technics with a good SNR (Ovchinnikov & Ovchinnikov, 1987). They are commonly used for Patch-Clamp technics (Yajuan *et al.*, 2012).
- *Circuits printed at boards or flexible polymers:* These electrodes are the last generation of electrodes. Usually, they are involved in invasive recordings, and for this reason, they are frequently printed in biocompatible materials (Muthuswamy *et al.*, 2016). Thanks to the biocompatibility and to their numerous available designs, they can be implanted in the living tissue for long periods or just for acute recording. Almost all of these electrodes have more than one contact site (also called multielectrode), which depending on the desired recording population, could have different diameters (from the size one cell up to millimeters). These multisite electrodes can be designed with

multiple shanks or in arrays to record LFP, unit and/or multiunit activities present in other parts of the brain.

2.2.2.1. Multielectrodes

The multichannel probes (or also called neural probes) exist for the demanding to record various site activity simultaneously and even to add also spatial characteristics. The multisite recordings increase the capability of analysis in each experiment exponentially. For example, it is well known that each region of the brain cortex has a specific function, and this fact is shown in the different electrode signals of EEG in human systems (Phillips *et al.*, 1984; Freeman & van Dijk, 1987).

Usually, the multi electrodes are designed to traverse and record the brain cortex and deeper structures, but also can be placed on brain slices. The multielectrodes are generally small and built with biocompatible materials (circuits printed at boards or flexible polymers) to be implanted chronically or just for acute recordings inside the brain. These invasive neural probes must be sharp and several millimeters long. Moreover, multielectrodes can be distributed exclusively in one or multiple shanks and in arrays.

The penetration of the multielectrode probes in the brain tissue can produce trauma; for that reason, is recommended to be slender probes and thinner as it's possible with a decent stiffness in order to cross the meninges properly (Seymour & Kipke, 2007; Stice *et al.*, 2007). In addition, the velocity that it is inserted the probe (single or multiple shank) it is an important factor to reduce the dimpling.

The **number** of recording sites in each design is different, but they tend to be powers of 2. In this case, the greater number of sites, the greater amount of bioelectric data can be recorded. These recorded data have the benefit of sharing the time in all the sites and the spatial relation of those recordings.

The **size** of each contact is related to the aimed population activity. The invasive multielectrode probes can record the local field potentials (LFP), the multi-unit (MUA), or single-unit activity (SUA) depending on the size of each contact. If the neuronal cell bodies in the mammalian brain are around 10-20 µm (Muthuswamy *et al.*, 2016), the diameter of the recording sites generally must be approximate between 10 µm (SUA and MUA) to 1 mm (LFP).

The **materials** used to build the electrodes are determined depending on extracellular media and how it is rich in ions; this determines the impedance of them. Usually, the multielectrodes are built-in low impedance materials like gold, platinum, and iridium/platinum.

The probe designated for our recordings is manufactured by NeuroNexus Tech (Figure 2.1). It is a multisite linear electrode (MLE) with 16 channels in a row, spaced by 150 µm (total distance from channel 1 to channel 16 is 2250 µm) and with 177 µm² (15 µm of diameter) of contact surface for each site, built-in Iridium. The 16 channels are placed in a 5 mm length shank, and the first channel starts at 33 µm from the tip. One of its essential specs is the flexibility that allows touching bregma on the skull (to calibrate the system) without breaking or deforming the shank.

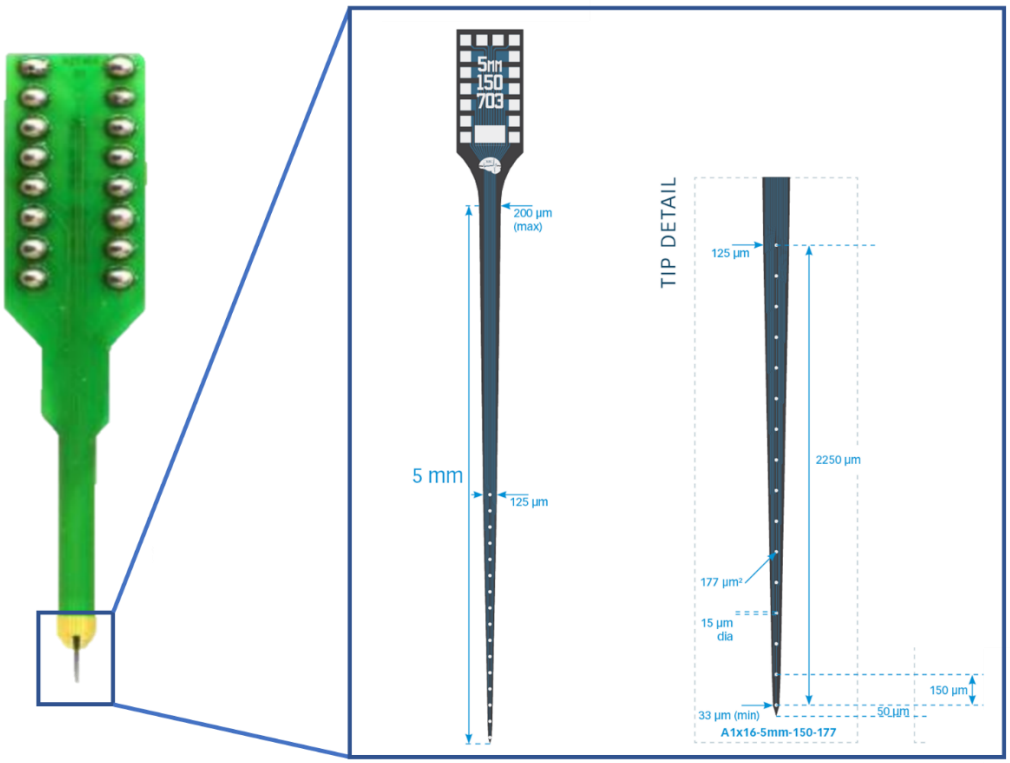

Figure 2.1. Multisite linear electrode (MLE) for the setup. The image shows the specifications of the chosen electrode (A1x16-5mm-150-177). Provided by NeuroNexus Tech.

2.2.3. Amplifiers

The amplifier is an essential electronic device that consists of a double-input (goal signal – reference signal) electronic circuit than its output signal is the differential of these two with its power increased. It is required to provide a power supply for the amplifier to increase the amplitude of the output signal respect the original, in addition, to preserve the shape of the signal (Agarwal & Lang, 2005). The gain is the expression of the ratio between the amplificated signal in connection with the original signal.

2.2.3.1. Preamplifiers

One of the main problems to acquire any electrophysiological signal is that usually, the primary signal collects environmental noise before it arrives at the amplifier or acquisition system (bad SNR). In some experimental EEG recordings in humans, the preamplifiers (amplifiers close or attached to the electrodes) are used to acquire the cerebral activity with the minimal electrical noise impact (50 - 60 Hz and their harmonics) (Grant *et al.*, 2006), but at the usual EEG recording is not required because the goal frequencies have enough power to reach the main amplifier without visible interferences (or also called noise). The goal frequencies in clinical EEG recordings are low compared with the MUA or SUA (>300 Hz) that they require in addition to a higher sampling frequency rate (recommended > 6 kHz). For that reason, it is a requirement in the MUA or SUA recordings to have a preamplifier before the signal reaches the main amplifier because this improves the SNR and the posterior filtering and analysis (Szabo & Marczynski, 1993).

The NeuroNexus 16-channel probe was mounted in an adapter (ADPT-NN-16) from Multi Channel Systems GmbH (MCS, Germany) with two preamplifiers (MPA8I, 2 x 8 channels input) with a fixed gain of x10, an input-noise of <1.5μV_{RMS} (1 Hz to 5kHz) and a bandwidth of DC to 50 kHz. Both preamplifiers are assembled to the NeuroNexus probe by the adapter from MCS (ADPT-NN-16), and the whole electrode's system is attached to a stereotaxic arm (Figure 2.2).

The electrode system is connected to two sockets at the signal collector (SC8x8) with an interface of 8 x 15-pin SubD connector and 0.08 Hz high pass filtered. Thus, the signal collector sends by a 68-pin MCS standard cable (C68x2M) the analog data to the main amplifier (located at the next experimentation room).

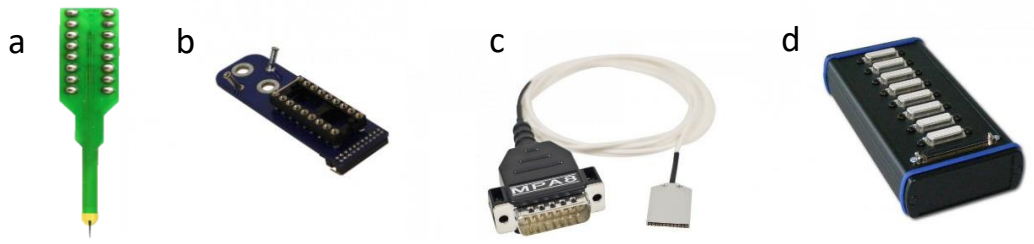

Figure 2.2. Images of the principal devices related to the pre amplifying setup. **(a)** NeuroNexus MLE probe with 16 channels at the printed circuit. **(b)** Adapter for the MLE *ADPT-NN-16*. **(c)** Preamplifier *MPA8I*. **(d)** Signal collector *SC8x8*.

2.2.3.2. Main amplifiers

Any electrophysiological activity requires to be amplified. As it was explained before, the differential amplifier needs two signals: one the goal signal and the other the reference (Seaba, 1984). In the market can be found some amplifiers with different specifications; some of them are more specific than others and differ in the number of input channels and the sampling frequency that can afford.

Our designed system for the multielectrode needs an amplifier with a wide input range, a programable gain with 32 inputs as minimum. For that reason, an amplifier system of 32 channels Programmable Gain Amplifier (PGA32) with a bandwidth from 1 to 5000 Hz was chosen. Also, it has an input noise of < 2 μV_{RMS} and an independently programmable gain from 10 to 5000. It was supplied by MCS as to as other devices: the output signal divider (SD32), formed by 32 BNC connectors, was added to the amplifier system to send the amplified output signals to the acquisition interface by BNC cables (Figure 2.3).

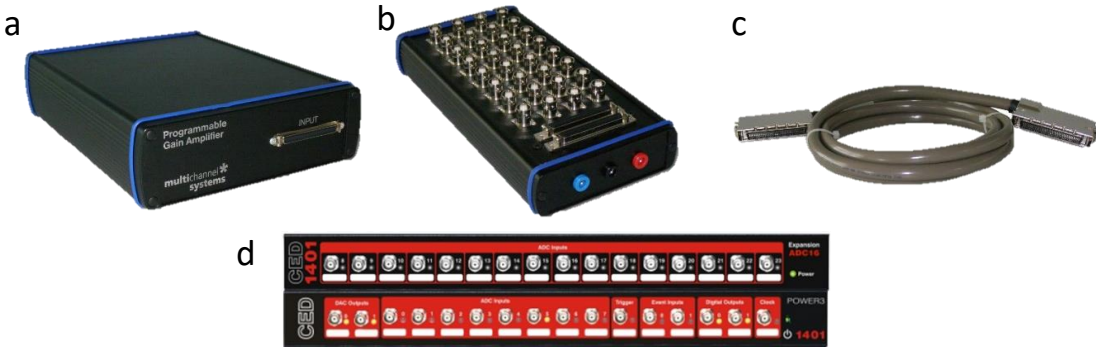

Figure 2.3. Images of the setup devices related to the amplification and acquisition. **(a)** Programmable Gain Amplifier of 32 channels (PGA). **(b)** Signal divider of 32 channels (SD32). **(c)** Wire to connect each device of MCS up to 68 channels (C68x2M). **(d)** Acquisition interface *Power CED1401-3*.

2.2.4. Acquisition interface

The acquisition interface must have the capability to record all the desired signals simultaneously with a correct sampling rate during long recording sessions. Also, the acquisition interface requires to have good accuracy in terms of time and noise.

Our selected interface (Power3-1401) was supplied by Cambridge Electronic Design (CED; Cambridge, UK) (Figure 2.3) because this interface has a complete range of application for electrophysiological experiments. The device works with its software (*Spike2*) to collect, process, display, and filter signals online or offline. The Power3-1401 can integrate other device signals that help to share the timeline's recording, and it can also be synchronized by triggers with other recording devices of our setup.

The unique specifications are 1MHz of multi-channel sampling rate, up to 48 waveform inputs (with expansion units), programable gain, and reasonable resolution of the clock with event inputs. This allows recording the 16 channel input signals of our MLE in high sampling rates.

2.2.5. Adaptations / modifications to the electrophysiological system

From the preamplifiers to the BNC outputs, the setup could be upgraded, but just with specific MCS products. The main problem was that MCS could not supply the parts that our recording protocol requires, for example, to add modules for electrophysiological or physiological signals. For that reason, the system has been studied in detail to add two ECoG electrodes, and one ECG monitor required for our protocol of recording, was added *posterior*. Also, the physiological activity like breathing and body's temperature (controlled by PID loop between the rectal thermocouple and heat plate) were monitored to control in-depth the anesthesia level and animal healthcare at the same time.

Two 15-pin SubD sockets were created to monitor and record the extra signals, and then they were connected to the SC8x8. The new channels use the same route as the preamplifier signals without any power supply (non-preamplified). In total, six channels were created and connected in this way: 2 at the socket-3 (ECoG-1 and ECoG-2), three at the socket-4 (ECG-1, ECG-2, and Breathing), and one BNC connected to the PID temperature system for the body's temperature (Figure 2.4). To record the ECG signals, three-needle electrodes were used (2 signals, 1 reference), two gold plated electrodes with one needle electrode for ECoG (2 signals, 1 reference), and one piezoelectric for the respiration signal.

To reduce the electrical noise of the electrophysiological system, a Faraday cage was used. This tool helps to isolate the signals of the recordings from the environmental noise, thanks to the principle of an electromagnetic field inside of a cage built-in conductive material cause that the external electric charges be distributed through the cage and the electromagnetic fields inside the Faraday cage be equal to 0.

Starting from the MLE probe to the acquisition system, the setup requires a technical mapping of whole channels (Figure 2.4), because the probe's electrodes are mapped in one way, inside the adapter ones are in another way. Those channels after pass the signal collector and PGA, to be acquired by the interface, the calculated channel map was entered manually to the software *Spike2* (Cambridge Electronic Design; Cambridge UK).

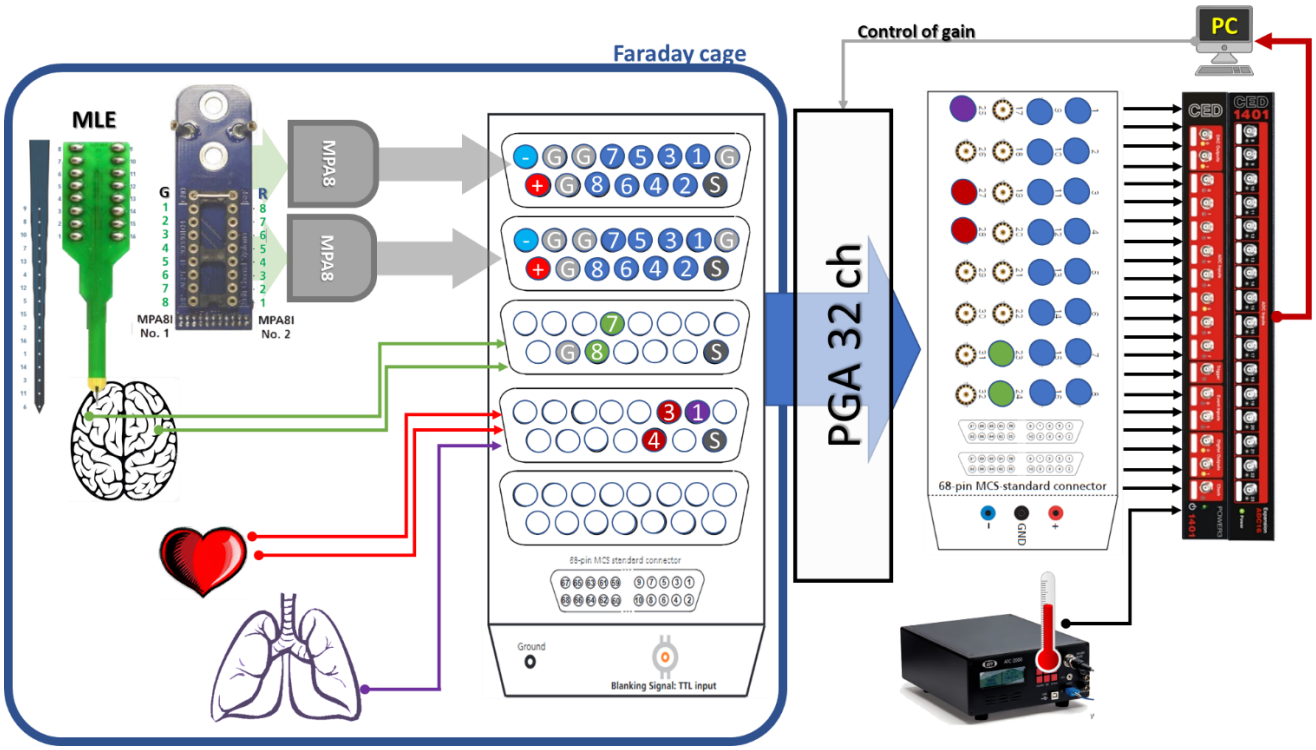

Figure 2.4. Summary of the electrophysiological system. The MLE (Multisite linear electrode) (Left-top) with its mapping numbers, Electrocorticogram electrodes (two green arrows), Electrocardiogram (two red arrows), and breathing signal (purple arrow) are connected to the different sockets at the signal collector (center) to drive the signals to the programmable gain amplifier (PGA) and after this to BNC-cables (black arrows) are plugged to the acquisition interface. The body's temperature sensor is plugged independently of PGA.

2.2.6. Main analyzes performed on electrophysiological data

2.2.6.1. Time-Frequency representation

The Time-Frequency representation (TFR) is a methodology that helps to characterize phase-locked and non-phase-locked changes in neuronal activity occurring in a determined epoch. According to the procedures described by Hoechstetter et al. (Hoechstetter *et al.*, 2004) and its implementation in BESA Research®, the TFR is expressed as the percentage power changes in a time-frequency bin in a specific signal (relative to the mean power over the baseline epoch for a specified frequency):

$$TFR = \frac{\mathrm{P(t,f)} - \mathrm{P_{baseline}(f)}}{\mathrm{P_{baseline}(f)}} . 100\%$$

where P(t,f) is the power at time *t* and frequency f and $\mathrm{P_{baseline}(f)}$ = mean activity at frequency f over the baseline period.

2.2.6.2. Current source density

The current source density (CSD) is a methodology based on the analysis of the extracellularly recorded potentials in a multitude of strategically positioned electrodes that will help to find the current source generators. Typically, the CSD is applied to the lower frequency range of the LFP (<500Hz), and it is commonly used in recordings that have some type of event, such as evoked potentials.

At the cellular level, when a positive current enters the cell, it is known as a sink current, and it is represented with negative values in the CSD analysis. On the contrary, if the current entering the cell is negative, it would be a current source, and it would be represented with positive values in the CSD analysis (Leung, 2011).

The rapid development of multielectrodes in the last decades (Egert *et al.*, 1998; Buzsáki, 2004; Senzai *et al.*, 2019) stimulated the interest to analyze LFP signals, including the CSD. The multiple approaches to estimate the CSD are the traditional (Mitzdorf, 1985), inverse (Łęski *et al.*, 2011), spike (Somogyvári *et al.*, 2012), and kernel (Potworowski *et al.*, 2011) CSDs. Each one of them has their pros and cons, the inverse CSD (iCSD) incorporate the assumptions about the structure of the sources or the properties of the tissue, the spike CSD (sCSD) was developed for localization of single-cell current sources, and the kernel CSD (kCSD) is the improved version of iCSD, constructing spaces of much larger dimensionality and dealing with the noise.

2.2.6.3. Wavelet coherence

The wavelet coherence is an analysis (Grinsted *et al.*, 2004) tool to extract the coherence and phase lag, using squared cross-wavelet coherence (R^2), of two time series without assumptions of linearity or stationarity (Chang & Glover, 2010). R^2 have values between 0 to 1 (represented in color scale) and it can be conceptualized as a correlation between time-frequency domain between two different signals.

2.2.6.4. Spike sorting

The study of the neuron firing recorded extracellularly is extended in Neuroscience. The use of specific electrodes and amplifiers is mandatory to have a good SNR for proper unit activity identification. These recordings also depend on the placement and orientation of the electrode tip with respect to the neuronal population to record and morphology of the neurons to record (Figure 2.5) (Gold *et al.*, 2006).

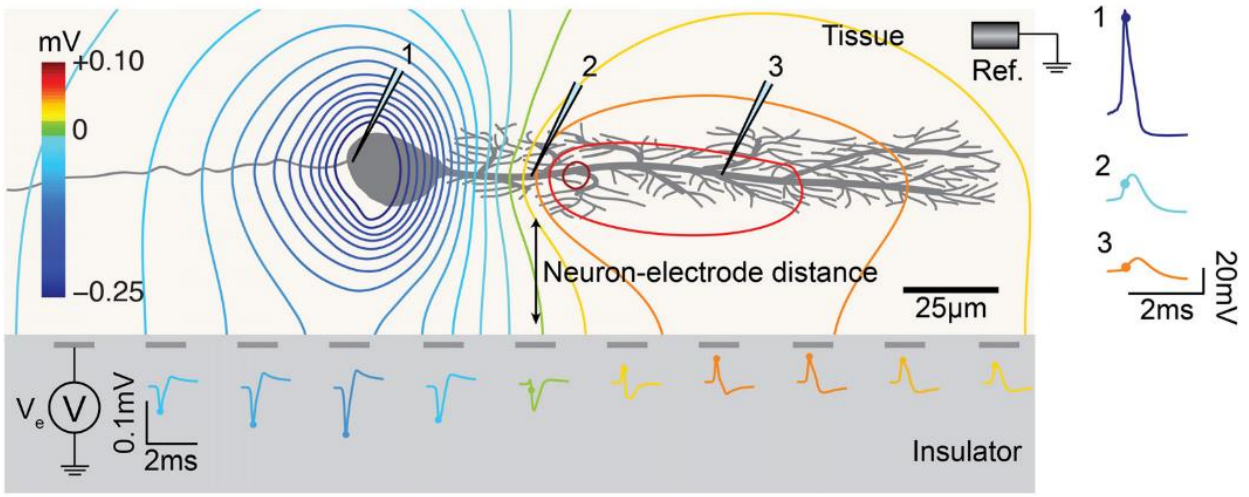

Figure 2.5. The General neuron-electrode interface is separated into two parts. The distance between the neuron and the electrodes influences the signal amplitude measured at the electrodes. The high spatial resolution allows for recording at several locations of a single neuron, with large negative spikes located at the peri-somatic area and positive spikes at the dendritic area (from Obien *et al.*, 2015).

A huge multitude of neurons exist in the brain and depend on the region to have a greater or lesser density of population. For that reason, spike sorting is an essential tool for the classification of which unit activity corresponds to which neuron.

It is well known that individual neuronal activity is related to processing in the brain itself. For this reason, over the years, multielectrodes have started to be used to record activities together throughout neuronal populations, opening up a wide range of possibilities, such as, for example, the study of connectivity in neuronal populations (Buzsáki, 2004). To try to separate the unit activity from a large MUA background is not easy at all, but these neurons can show amazing responses (Quiroga *et al.*, 2005).

The easiest way to separate the unit activities is an amplitude discriminator. It is the fastest way, but the units usually can share this peak amplitude and have different shapes. For that reason, it is commonly extended the use of 'windows discriminators' to solve this problem by the commercial acquisition systems. Still, it has the disadvantage that needs to be set by the user (Quiroga, 2007).

Template matching is another strategy to perform spike sorting. This approach selects representative unit activities as templates for each cluster and assigns the remaining units to them, based on a mean square metric.

Spike sorting algorithms usually have four major steps, where each one represents a critical procedure for the final result (Rey *et al.*, 2015). The main steps from continuous data to the classified spike shapes are the followings (Figure 2.6):

I. *Filtering*: To start the processing the continuous data, it is necessary to apply a bandpass filter to visualize correctly the spikes. This step is crucial and requires using it correctly because this can change the unit activity shapes drastically. A high sampling frequency rate is especially recommended to have enough data points for following data processing (> 6 kHz). An example of a usual bandpass filter is 300 to 3000 Hz, where the frequencies below 300 Hz are filtered to remove the high amplitude slow-components, and the frequencies above 3000 Hz are removed to avoid the noisy appearance. If the bandpass filter is too narrow, it can hide some spike features present in the data, which compromise the final clustering. Preferably, it is recommended by the literature the use of non-causal filters in front of the causal, because the causal filters can introduce phase distortions changing the final spike shapes (Quiroga *et al.*, 2005; Quiroga, 2007).

II. *Spike detection*: Usually, the spikes are detected using an amplitude threshold. This can be set automatically or manually but set by a multiple of the standard deviation of the signal. To perform it for a large number of channels, an automatic threshold is preferable, but it could be really high value if the neuronal firing rate is high, which would lead to miss low amplitude spikes. The detected spikes are stored for a posterior clustering. The number of data points of the stored spike shapes is preferable to be as much as is possible and depends on the sampling rate of the recording.

III. *Feature extraction*: To extract the spike shapes' features is mandatory before applying any clustering algorithms if it wants to be processed in a reasonable time. This step transforms the actual dimension of shapes to a low dimensional space with few features. Usually, the method to extract the spike shapes' features takes 2 or 3 principal components (Abeles & Goldstein, 1977), which contains 80% of the signal's energy. Principal components analysis (PCA) is a dimensionality reduction that selects the essential features of our spikes, transform them, and quantifies the importance of these features, to keep the essential features and drop the others.

IV. *Clustering*: Clustering is the final step of the spike clustering, based on to group the sorted spikes with similar features to the same cluster. Exist various approaches included the manual one, but this one is a high time-consumer, and it could introduce errors (Harris *et al.*, 2000). Other approaches use algorithms that assume Gaussian distribution for the clusters (Harris *et al.*, 2000; Pouzat *et al.*, 2002), or random process algorithms (Blatt *et al.*, 1996).

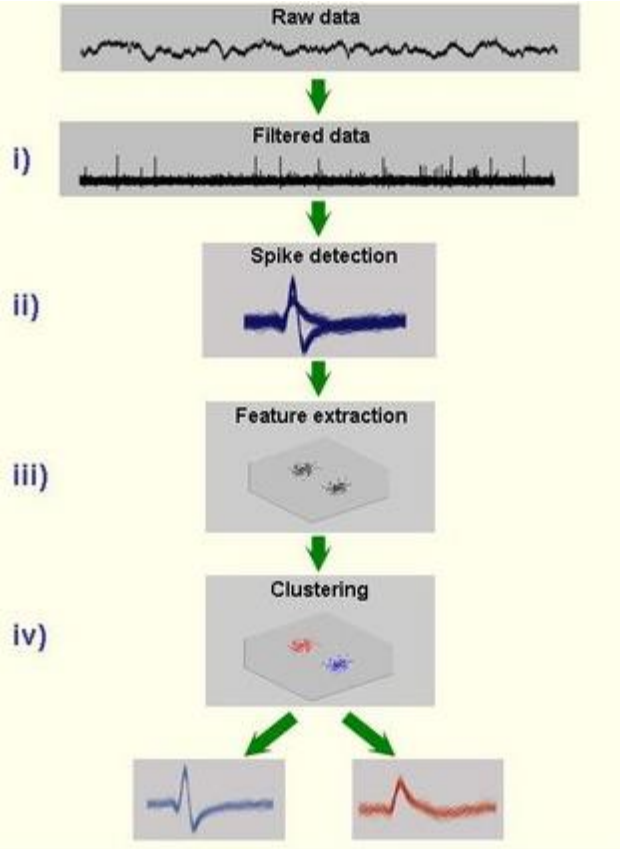

Figure 2.6. Schematic representation of the main steps for spike sorting. i) Filtering; ii) Spike detection; iii) Feature extraction; iv) Clustering (from Quiroga, 2007).

2.3. Systems based in optical imaging with near-infrared lights

2.3.1. Near-infrared spectroscopy

The fundamental components for NIRS systems are light sources and detectors, accompanied by amplification, electronic drivers, and data acquisition methods. The methodology for measuring oxy- and deoxy- hemoglobin in NIRS has three main paradigms from the probe to the tissue by the diffuse optical technique: Time-domain paradigm, continuous-wave paradigm, and frequency-domain paradigm. NIRS can be classified into two types, slow and fast optical signals.

2.3.1.1. Fundamental components

2.3.1.1.1. Light source

The light source must be capable of projecting different light wavelengths. The power of emitting is important to be adjusted to compensate for the losses in magnitude inside of a safe range. A critical parameter that needs to be resolute to evaluate laser safety and efficiency is the photothermal impact of

laser sources. The increment of temperature can produce alterations in the normal cellular metabolism to the electrical capacitance of membrane, leading to necrosis (Fujii & Ibata, 1982; LaManna *et al.*, 1989; Seese *et al.*, 1998; Ito *et al.*, 2000). If the temperature exceeds than 1ºC could have long-term effects on the brain tissue (Denda *et al.*, 2010). The laser wavelength and power are effective constraints for tissue-released energy calculation; for example, the wavelengths that exceed the 950 nm are used for laser surgeries (Bozkurt & Onaral, 2004).

One category of the light source is the laser diode (LD), that it has high-precision spectroscopy with a suitable acquisition timescale. The power range of LDs is from <1 to 500mW with discrete colors (1nm) but is expensive compared to other options, like tungsten halogen-lamps or light-emitting diodes (LED), with less precision in colors and minor power range (Strangman *et al.*, 2002). For these reasons, the laser diodes were used in our experimentation, and their two wavelengths were defined at 830 and 690 nm according to best ranges to resolve HbO_2 and HbR index (Figure 2.7) with a safe exposure (Nourhashemi *et al.*, 2016). Our experimental setup, values were tuned to 2.56mW for 830nm and 7.13mW for 690nm, considered safe for the skin (restricted by the American National Standards Institute (ANSI)). Imagent™ (ISS Inc.) products were used for our optical recordings.

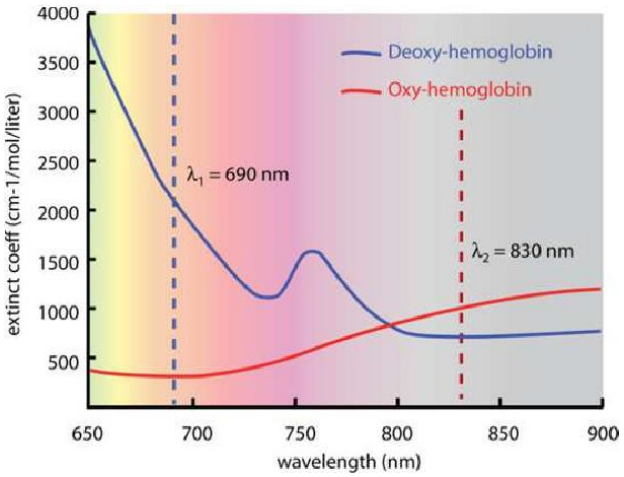

Figure 2.7. Oxy-hemoglobin (HbO_2) and deoxy-hemoglobin (HbR) absorption spectrum (from Mansouri & Kashou, 2012).

2.3.1.1.2. Light detector

The other critical element in the NIRS instrumentation is the light detector because this element must be matched up with the light source's nature. If the level of the light source is low, the photodetectors must have high sensitivity.

For the near-infrared detection, a photo-multiplier tube (PMT) was required in our setup. This device is capable of detecting, not just the infrared-light; it includes visible and ultra-violet light range, with high sensitivity and low noise in lights detection. As the light source, PMT is provided in Imagent™ (ISS Inc.) device. This element is formed by an anode, a series of dynodes, and a photocathode inside of a vacuum tube. The BOXY (ISS Inc.) software is used to control the voltage implicated in each PMT detection of our device.

2.3.1.1.3. Optical fibers

Optical fibers are one crucial part of the NIRS system. This component is in contact with the goal of study, and for that, in its design must take in consideration the light coupling between the source-detector setup, and which approach for calculation are chosen.

The material of the optical fibers (also called optodes) is generally glass. This material usually makes the core and the cladding but with a different refraction index to help the light remain inside the core. The optodes placement design must consider setting a correct distance between source and detectors because it is intrinsically related to the deepness of the light, which is around half of that distance (if they at placed at 90º). With a higher distance between them, a deeper structure will be recorded, but with a worse SNR, and if it is too short, the physiological noise will be recorded (Figure 2.8).

In the optical recordings, a good and stable connection between the source-detector pairs at the surface of attachment ensures the stability of photons path length. Three of the main characteristics to take into consideration to design the protocol for use optodes are their place on the scalp, the light-shielding, the distance between source and detector, and their angle on the scalp surface.

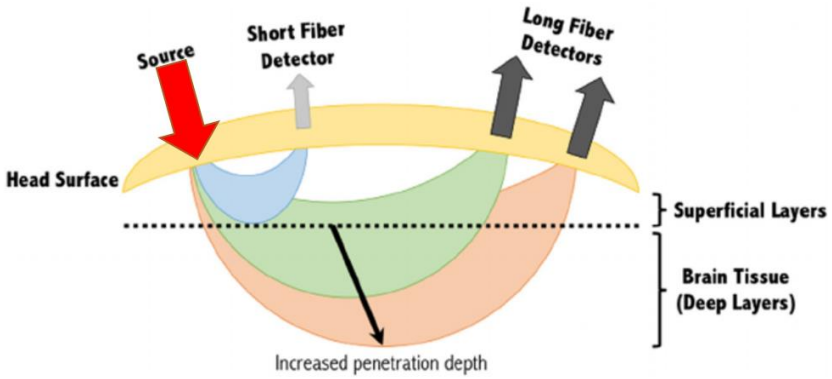

Figure 2.8. Different profiles of the banana shape of the near-infrared spectroscopy (NIRS) at various source-detector distances. One source can provide different recordings depending on the separation of the detector. The short or long separation of the source-detector can provide from physiological noise up to don't detect the signal.

2.3.1.2. The methodology of NIRS measurement

2.3.1.2.1. Continuous wave (CW)

It is the method where the light is emitted continuously with constant amplitude (Nioka *et al.*, 1997; Siegel *et al.*, 1999) (Figure 2.9). The system measures continuous changes in the optical attenuation (changes in the signal intensity), which means that it can only measure the hemodynamic changes of the blood in a same region (Hoshi, 2003). The variations in the tissue chromophore concentrations from the baseline value can be obtained from the modified Beer-Lambert law (absorption of light in a medium). The attenuation of light is linked with the changes in concentrations in chromophores and it can be obtained by the modified Beer-Lambert law: $A = P \times L \times E \times C + K$, where A is the absorbance, E is the extinction coefficient (in mol/cm), P is the pathlength of samples (in cm), C is the concentration of compounds (in mol/L), and additive term, K, due to scattering losses (Victor & Weindling, 2008). This method cannot measure the absolute concentration value because it is required than the attenuated light components (scattering and absorption) be separated. To achieve that, it is necessary to use frequency-domain or time-resolved methods.

2.3.1.2.2. Time-domain (TD)

The time-domain method uses technics of pulsed-laser sources and photodetectors with picosecond resolution. A mathematical approach based on diffusion theory allows the estimation of absorption/scattering coefficients of the media through the measurement of the differential pathlength (Figure 2.8). The absolute values of the hemodynamic components and the tissue Hb_2O saturation measurement can be provided by this methodology (Ferrari & Quaresima, 2012). The main problem with this method is that the instrumentation is expensive and is not portable.

2.3.1.2.3. Frequency domain (FD)

The methodology of the Frequency Domain Spectroscopy (FD) is based on the radio frequency amplitude modulated sources (generally 100-1000 MHz) (Figure 2.8). This technique provides less information than the TD, but it gives a direct calculation of absorption and scattering factors of the tissue via the amplitude reduction and its phase shift (Ø) from the light source (Yang *et al.*, 1997), and an absolute concentration value of hemodynamic components and the tissue HbO_2 saturation.

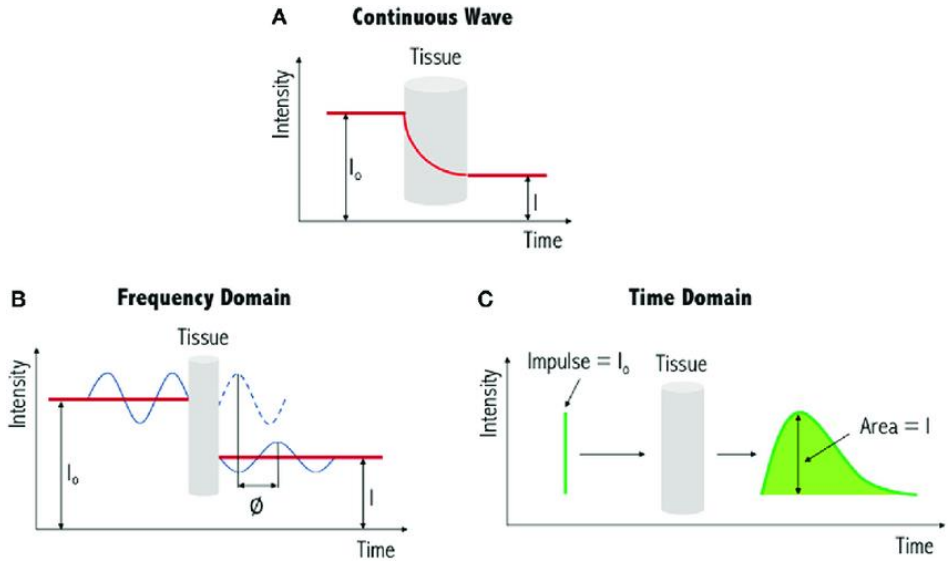

Figure 2.9. Three physical techniques of near-infrared spectroscopy. **(A)** Continuous-wave: measures the intensity (*I*) changes of the light after passing through the tissue, also called differential pathlength (DP). **(B)** Frequency domain: the phase shift (Ø) between the source and transmitted light estimates the DP. **(C)** Time-domain: in order to calculate the DP is to use the mean time taken to traverse the tissue (Rupawala *et al.*, 2018).

2.3.1.3. Slow optical signal

Nowadays, NIRS is well known as a useful method for cerebral hemodynamic research (Roche-Labarbe *et al.*, 2010; Keller *et al.*, 2010; Bourel-Ponchel *et al.*, 2017). The functional NIRS are often called slow signal due to the hemodynamic changes look relatively slow. Usually, the stimulation provokes a slow hemodynamic response after the onset, related to the blood oxygenation and CBF. This signal is commonly used with EEG to link the electrical activity with the hemodynamic.

2.3.1.4. Fast optical signal

To measure the changes light scattering of the neurons related to neuronal activity in the cortical tissue, the NIRS has been used in the last decades (Cohen, 1973; Gratton & Fabiani, 1998). The extracted signals of light scattering are termed as “fast optical signals” (FOS) or “event-related optical signals” (EROS) because they are produced in the course of milliseconds (Gratton & Fabiani, 2010). They are not related to the changes in HbO_2, HbR or water. Principally, the changes in FOS record the light scattering in the active tissues. These changes are fast in order of milliseconds; for that, a fast acquisition rate is mandatory.

The types of parameters are related to the passage of the light through the tissue. The first one is the light intensity associated with the quantity of light passing through the tissue, and the second one is

the photon delay, that is the exact time that the photons require to pass through the tissue. The second parameter, if the frequency-domain is used, it can be expressed as phase delay (Figure 2.10) (Gratton & Fabiani, 1998).

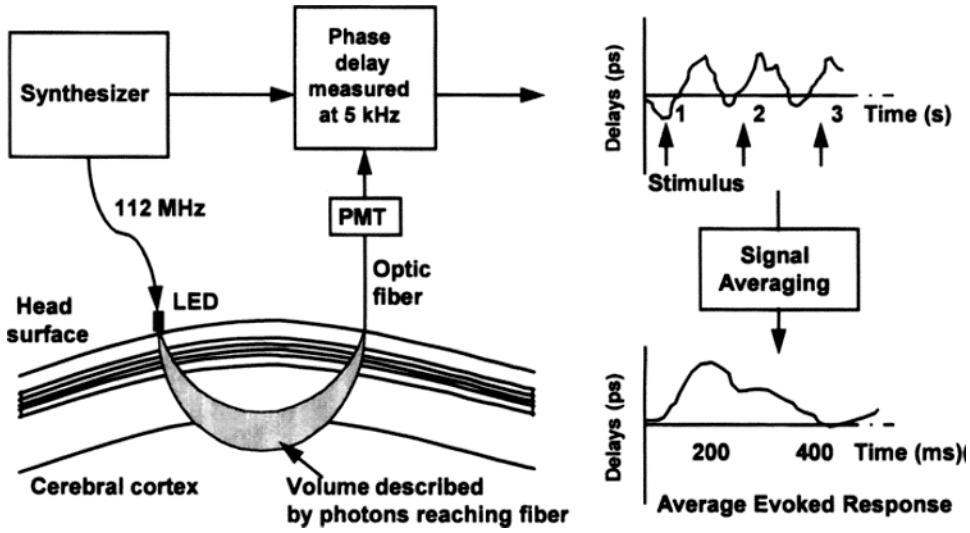

Figure 2.10. Fast optical signal (FOS) recording methodology. *Left*, the recording setup is based on a light source, a detector, and a radiofrequency synthesizer. *Right*, the process of the obtained data (from Fabiani *et al.*, 1996).

2.3.2. Diffuse Correlation Spectroscopy: Cerebral blood flow measurement method.

Monitoring the changes of the scattered light over tissue contributes to having additional information because it corresponds to the light scattering of red blood cells. The electric field potential or the Fourier Transform measurements show the scattering of the tissue that it helps to extract a significant signal like the blood flow (Durduran *et al.*, 2010).

A simple comparison between the NIRS and Diffuse Correlation Spectroscopy (DCS) is that they are two techniques that use near-infrared light but the DCS uses a complex methodology with extra calculations.

The DCS can measure the cerebral blood flow (CBF) in small vessels. Currently exist other techniques to know the rCBF like the transcranial Doppler (TCD) method, but this technique just estimates the rCBF in the main arteries. DCS is based on the movement of scatters such as red blood cells inside the tissue, instead of changing the oxygen flows or injecting any solution to the subject to record the CBF (by fNIRS method) (Patel *et al.*, 1998), that could have ethical limitations.

To calculate the blood flow index is required a temporal autocorrelation function of the electric field (Durduran & Yodh, 2014), that is made by the DCS device. The main optical properties implicated in DCS are the tissue absorption and scattering coefficient. Their difference is an additional absorption term that is dependent of the scattering dynamics. The autocorrelation function draws a curve in a standard condition, for example in a relaxed muscle, this creates a curve than usually shows a high correlation between the extracted interval of the signal at time t and his next window at time $t+\tau$. When the optodes are placed in experimental conditions on the tissue, like a contracted muscle, the autocorrelation curve shows a major discrepancy at the correlation curve, compared to the first example (Figure 2.11). To see this discrepancy all over the recording is required to extract the angle (θ) of the autocorrelation curve par each window continuously all over the recording and plot their values like a continuous signal, this method adds a good temporal dimension to analyze any variations of the blood flow recording.

In our setup, we used a DCS system developed by Hemophotonics S.L. (Barcelona, Spain). This system displays the autocorrelation curve and its consequent blood flow at the screen. This uses CW lasers in the near-infrared range (~785 nm, ~28mW), four fast photon-counting avalanche photodiodes (APD), and a four-channel autocorrelator board. The optodes' use is carefully selected for our protocols and their ratio for photon emitting and detection.

The light source in this device usually is used with a distance >2cm (Nourhashemi *et al.*, 2017), but our setup (5 mm distance) was mandatory to use an adjustable attenuator to reduce the power of the source until the photodetector does not be saturated.

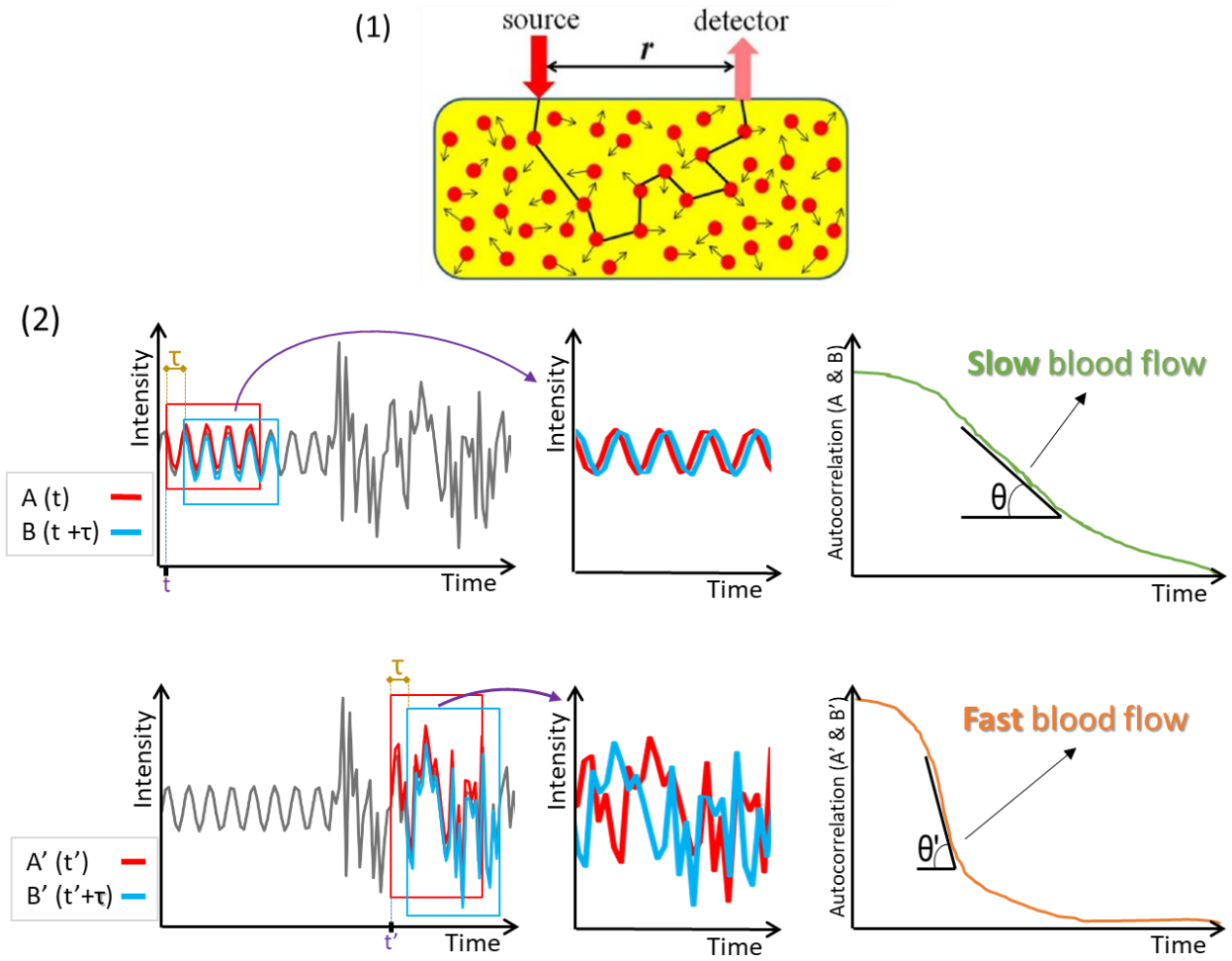

Figure 2.11. Basics of diffuse correlation spectroscopy (DCS) of the blood flow recordings. **(1)** The source and detector optodes are situated on the tissue with a definite distance ***r***, in black line is the trajectory of one collected photon released by the source; **(2)** Process for extracts two periods with a **τ** difference of time for each one, and their autocorrelation. The three images of top show a schematic of slow blood flow at time ***t*** because the angle **θ** of the autocorrelation curve is acute; The three images of bot show the same signal as top at time ***t'***, where the signal has an open angle **θ'** of autocorrelation curve, faster blood flow.

2.4. Drugs

The electrophysiological recordings were done with urethane anesthesia. The urethane gives a reasonable level of anesthesia for surgeries without interferences in brain activity (Maggi & Meli, 1986). The neural activity is kept meanwhile, the rat is completely anesthetized.

The use of urethane can produce an activity diminution of the LFP; for that reason, some authors define the theta frequencies in anesthetized rats between 2.5 to 8 Hz (Leung, 1985) in front of 3 to 12 Hz.

If the anesthesia dosage level exceeds 1.5 g/kg in rat, the urethane can depress the cardiorespiratory and thermoregulation functions (Maggi & Meli, 1986). For that reason, in our experiments were used an intraperitoneal injection of urethane between 1.25 to 1.5 g/Kg. This anesthetic takes around 30 to 45 minutes to produce the desired effect, but it is capable of keeping a stable level of

sedation for 7 hours after the administration keeping the thermoregulation, cardiorespiratory and neural activity (Pagliardini *et al.*, 2013).

The level of anesthesia of each rat was checked, testing theirs reflects. The reflexes were checked from caudal part to cranial part direction. The reflex testing involves a noxious stimulus like tail pinch, pedal withdrawal, ear pinch, and finally, palpebral reflex; if after this tests the rat increases the respiratory rate, heart rate, or blood pressure, it is convenient to wait more time or reinject. When all the reflexes are no longer present, it is ready for the surgical procedure. In the case of urethane anesthesia, the reinjections when the reflexes still present after a specified time or appear during the recording are 0.3g/Kg intraperitoneally.

Before any intervention, the urethane solution was prepared the same day and heated to 30-36ºC for don't create a contrast with the internal temperature of the animal after the injection.

To avoid the animal suffering in the urethane, anesthetized animals are required to use local anesthesia to block the sensations in the surgical area. Lidocaine was used topically at the external ear, skin of incision site, and the exposed skull.

For the Penicillin model of IIS was used Penicillin-G (PG) from SIGMA-ALDRICH. After mixing around 7 ml of H_2O with 1 million units of PG, the solution can be stockage at 25 ºC for 3 days, 2 to 8ºC for weeks, and from -20°C for months/years. In our case, the Penicillin was stockage in several Eppendorf filled up with 20µL each one (one Eppendorf was one experiment) and kept inside the freezer at -28ºC.

2.5. Experimentation

2.5.1. Animal preparation

To realize all the experiments described in this thesis 82 (17 + 27 + 16 + 21) male adult Sprague-Dawley (Blackthorn, Bicester, UK) rats were used (Table 2.1) with a weight comprises between 260 and 550g. Those rats were at the animal facility of the *Université de Picardie Jules Verne* (UPJV) in a controlled temperature (23±3ºC), the regular cycle of light-obscurity, and fed with standard rat food and tap water *ad libitum*. The number of rats and their suffering was approved by the *Direction Générale de la recherche et de l'innovation* (reference number: APAFIS#1464-2015081710033478.V6) and following the recommendations of the Ethical Committee of the Animalary Platform of the UPJV (B80021009). In all the cases, the number of rats and their suffering was taken carefully.

Table 2.1. The number of rats destinated for each protocol and the number of rats that couldn't be recorded.

Protocol	Designated subjects	Dead subjects
ECoG + NIRS	17	2
MLE + ECoG + NIRS	27	6
MLE alone	16	5
MLE + DCS	21	4
Total	81	17

Each rat was weighted on the scale and anesthetized in a dose of 1.5g/kg by intraperitoneal injection. During the experimental procedure, the recording body's temperature (rectal thermometer), breathing, and heart rate were controlled to know the anesthesia level. Around 1 hour after the injection, the surgical protocol was started.

The animal was placed at the stereotaxic frame (World Precision Instruments) to expose the skull, removing part of its scalp. A 10x15mm field of bone was exposed when the periosteum was removed and eight craniotomy holes (diameter of 1.5 - 2mm) was drilled at determined coordinates (Paxinos & Watson, 2006) (Table 2.2).

Table 2.2. Coordinates of each probe in millimeters, from Bregma (Paxinos & Watson, 2006).

	Probe	Antero-Posterior	Medio-Lateral	Dorso-Ventral
	ECoG 1	0	2.5 or 3.5	0 - 0.2
	ECoG 2	0	-2.5	0 - 0.2
	MLE	0	2.5 or -2.5	2.5 - 3
	Reference of MLE	10.5	-2	0
NIRS	Emitter 1	2.5	2.5	0 - 0.2
NIRS	Emitter 2	2.5	-2.5	0 - 0.2
NIRS	Detector A	-2.5	2.5	0 - 0.2
NIRS	Detector B	-2.5	-2.5	0 - 0.2
DCS	Emitter	2.5	2.5	0 - 0.2
DCS	Detector	-2.5	2.5	0 - 0.2

Then the rats and the stereotaxic were placed inside the Faraday cage to place the different probes for spectroscopy, electrophysiology, and physiology measurements.

For monitoring the animal welfare, three electrodes of ECG was positioned (two in the skin of the frontal paws and one in the skin of left-rear paw); a piezoelectric at the ventral part (close to the diaphragm) to record the breathing, and a rectal thermometer with a PID to control a heating pad (to keep the rats at 37-38ºC).

2.5.2. Recordings with multilinear electrodes

After the physiological probes were placed, the multilinear electrode (MLE) was introduced 2.5 to 3mm (+1 mm to cross the bone) at Bregma in 90º of the cortical surface, in due to record the entire columnar cortex (6 layers). This step has to be done carefully to don't damage neurons with the penetration speed and even electrode with any sliver of bone from the previous trepanation; also the state of the electrodes must be checked for each experiment, cleaning it with an enzymatic detergent if it is required. The reference electrode was placed at the right part of the occipital bone through a screw. The reference electrode was a screw placed at the occipital bone and connected to the probe's adapter.

The ECoG electrodes are placed just after the MLE probe inside the holes at 90º relative to the neocortical surface and trying to leave enough space for the spectrometry optodes (Figure 2.12). Their reference electrode was placed at the neck muscle using a needle electrode.

2.5.3. Recordings with NIRS system

The optodes of the NIRS setup are 8 in total: 4 sets, two with one 690 nm, and one 830 nm emitter in every one and two sets with one 690nm and one 830nm detector. Each set of emitters was placed caudally at 2.5mm from Bregma and 2.5 mm on each side of the midline, and each set of detectors was placed rostrally at 2.5mm from Bregma and 2.5mm on each side of the midline. All the optodes were inserted into the holes and secured at 90º relatives to the neocortical surface. The distance between them are in total 5mm because the created banana-shape photon trajectory 1.7mm corresponds to the desired deepness to research about the light scattering changes related to the neural activity, that is one-third of that distance (Pogue *et al.*, 1995).

The NIRS system, before starting the acquisition, was turned on to reach a suitable temperature of work for their internal components. The optodes were checked at the animal brain looking its raw data to determine than they work correctly (for any micro or macro bending), to don't have any saturation of the signal or low intensity, they had to be fixed and calibrated by software before any recording. After this step, a baseline period for reference was recorded for 15 minutes, synchronizing at first the electrophysiological system (MLE, ECG, ECoG, Breathing and Body's temperature) with the NIRS system using a button to produce the synchronization trigger (Figure 2.12A). All the recordings were done in a dark room and recorded in the next room, according to don't interfere in the acquired signal.

2.5.4. Recordings with DCS system

The DCS setup (Figure 2.12B) has just two optodes in front of the NIRS setup that have four sets because the temporal resolution, if it has four optodes (2 par hemisphere) reduces to half. In our experiment, we want to analyze fast activities related to IISs; then it is required the maximum possible points per second. The DCS optodes were positioned in the same holes of the left hemisphere as the emitter and detector of the NIRS and fixed at 90º to have a comparable banana-shape between the different systems.

Before the start of DCS recordings, the optodes were cleaned and tested. The distance between the emitter and detector is too short for DCS systems, and this saturates the detector, for that was implanted an adjustable attenuator of light at the source laser, that required to be calibrated in each recording. Like the NIRS system, all the recordings were done in a dark room and recorded at the next room, according to don't interfere in the acquired signal. The DCS setup requires to send a trigger to the electrophysiological system to be synchronized.

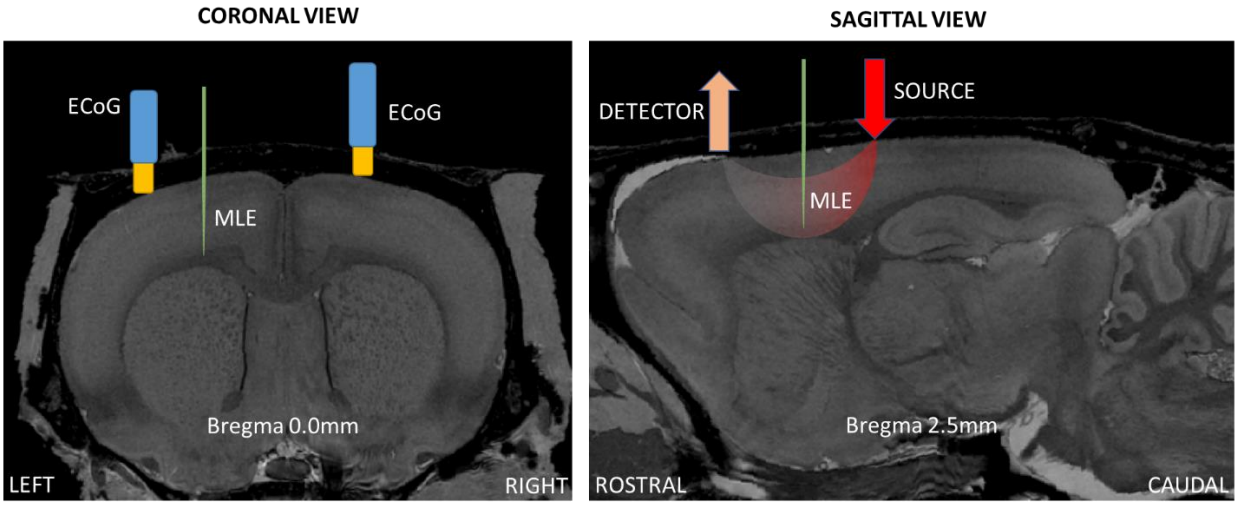

Figure 2.12. Coronal and sagittal views in MRI atlas for Sprague-Dawley rats (Papp *et al.*, 2014). *Left side*, the MLE and ECoG electrodes at Bregma 0.0mm coronal slice. *Right side*, detector, and light source optodes placement (linked with the photon diffusion banana shape) with MLE at a sagittal slice (Bregma 2.5mm).

2.5.5. Apparition of IISs

A dose of Penicillin G was applied to produce IISs in the hole located at the left hemisphere on the coordinates AP 0mm and ML 2.5mm. This drug has a GABAergic inhibition of the neuronal tissue. For an easier absorption of the neural tissue, the dura-mater of the hole was removed, and a volume of 6 - 8 µL (1000 – 1500 units) was expulsed mechanically by a glass micropipette (*Hamilton*®) and allowed to flow over the cortical surface. After this step, it was necessary to wait about 20 minutes to see the effect of the PG in the ECoG recording. If the spikes don't appear, a dose of 2µL was added and wait 15 minutes more.

After the apparition of the IIS, the recordings were continued approximately 80 minutes in NIRS recordings, and in DCS recordings were 70 minutes recording in the left hemisphere and 20 minutes in the right hemisphere.

In some recordings, the position of the MLE probe was changed of hemisphere 20 minutes before finishing the protocol to record the ECoG hole where it was not applied to the PG.

2.5.6. Data acquisition

The signals of MLE and ECoG were amplified by Multi-Channel Systems setup and recorded using the CED 1401 (Cambridge Electronic Design Ltd) acquisition board interface (Figure 2.13). The MLE signals were sampled at 20kHz par channel, and the two monopolar gold-plated electrodes of ECoG were sampled at 1024 Hz each one. The deeper channel of MLE was filtered online (IIR filter 300-3000Hz) to show the multiunit activities during the recordings. The LFP of the whole electrode's probe is displayed one next to the others.

NIRS recordings were realized with a frequency-domain spectrometer, where the two sets of emitters were modulated at a frequency of 110MHz (Figure 2.13). The sampling frequency of the detectors was 156.25 Hz, according to achieve two kinds of results the FOS and hemodynamic analysis. The data cannot be plotted by the BOXY software; this must be processed offline.

For DCS recordings, was set then the extract of the autocorrelation curve angle result was extracted at 1 sample every 0.46 seconds (2.5Hz). The data are plotted online at the DCS screen computer all over the recording, to have a look of the cerebral blood flow data (Figure 2.13).

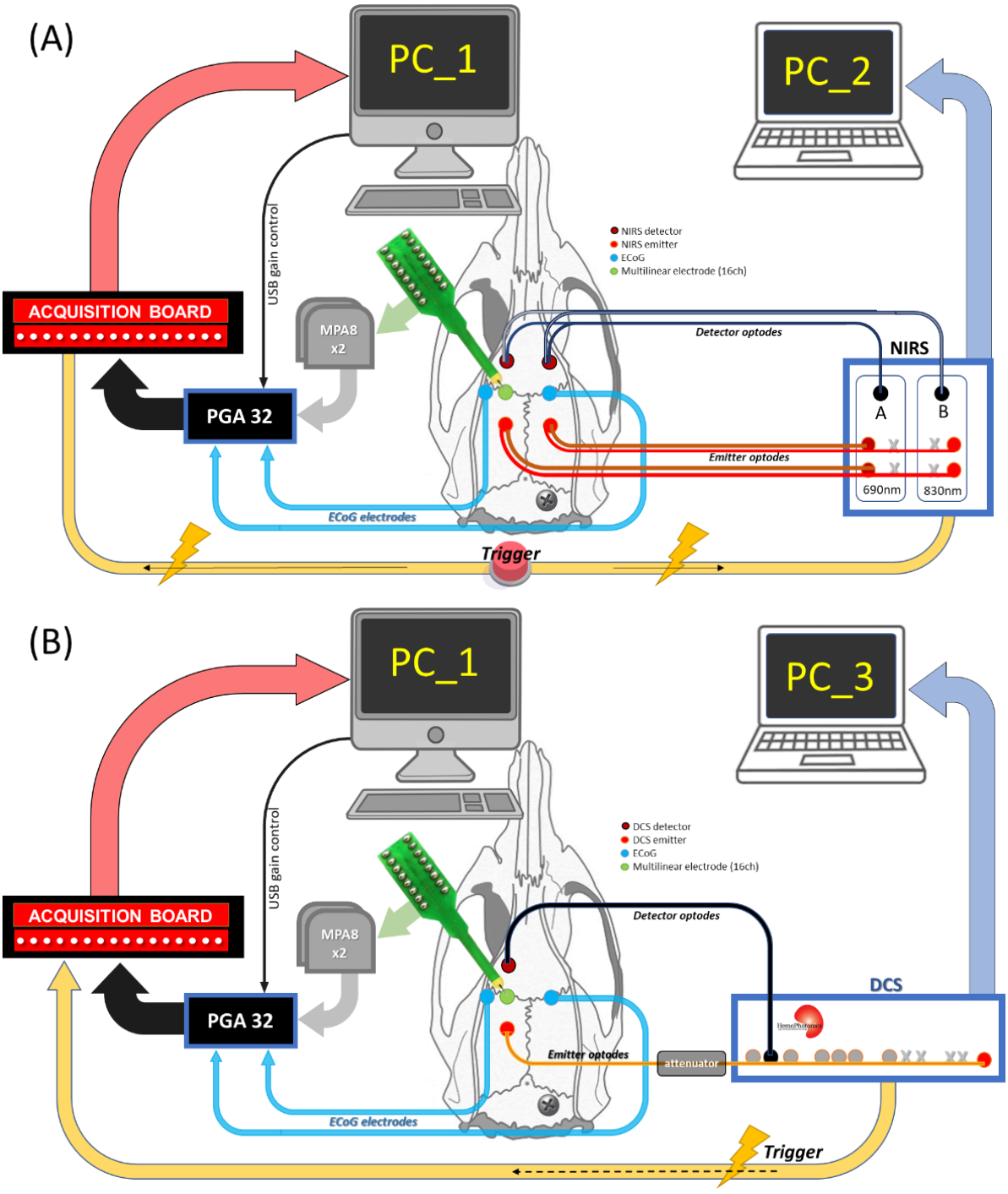

Figure 2.13. Schemas of the two acquisition methods with the MLE used. **(A)** Schema of the NIRS system and the MLE. The distribution of the different sets of emitters and detectors are represented. The trigger is an external button that produces a common artifact in both devices. The PGA receives the ECoG signals from the MLE and its digitalized at the acquisition board to send it to the PC_1. The NIRS device digitalizes the data and send it to the PC_2. **(B)** Schema of the DCS system and the MLE. The distribution of the detector and the emitter optodes with the attenuator are represented. The data is digitalized in the DCS system, and it is sent to the PC_3. The acquisition board of MLE and DCS systems is synchronized by a trigger produced by the DCS system.

2.6. Data analysis

2.6.1. Electrophysiological data analysis

To evaluate the changes in electrical, hemodynamic, and cellular configuration around IISs, the first step was to define time zero (T0). The MLE channel's signal closest to the surface of the cortex was used to identify the IIS peaks, and their times were defined as a T0. As commonly observed in penicillin rat models (Rossokhin *et al.*, 2014), the shape of the IISs consists of a sharp negative peak followed by a positive slow wave. T0 of IISs was extracted by downsampling the signal (from 20 kHz to 1 kHz) and then applying a finite impulse response (FIR) bandpass filter (1-35 Hz) to avoid unnecessary frequencies. The IISs were then detected semi-automatically and clustered using a template-matching technique (*Spike2*, CED). Just the IIS shapes with >80 % inside template were accepted.

To characterize the dispersion of the IIS onsets, just the IISs with an inter-spike interval (ISI) >500 ms was selected, was performed the coefficients of variation (CV) to define the rhythmicity of the firing rate in each rat. CV = $(\sigma / \bar{x})\cdot 100\%$, where σ is the standard deviation of the IIS firing rate and $\bar{x}$ the mean of the IIS firing rate. To understand if exist a role between low or high ISI on the number of the neuronal population involved in creating an IIS, the normalized IIS peak amplitude contrasted to ISI times was performed for each rat. A heat map spot density was developed using all the results achieved in the previous step to highlight the relationship between the normalized IIS peak amplitude and the ISI values in all the rats.

To generate a global view of the IISs shapes presents in all the subjects, the LFP signal of the superficial channel was averaged for each rat. No filtering was applied to investigate any variations or calculate their average amplitude, with and without 1.5 seconds of isolation. This isolation was performed for a better analysis of the pre-spike period, non-overlapping IIS epochs lasting 3 sec (-1.5; +1.5 sec) to avoid or at least minimize the effects between IISs.

The LFP power changes surrounding IISs were quantified by averaging their root mean square (RMS) ± 1.5 s around each T0 for each rat independently. The result of averaging the superficial channel was placed in contrast to the deeper one. Their difference was evaluated to know when the changes in the treated LFP signal became significant; for that reason, a Bonferroni corrected t-test was applied on the LFP (baseline - 800 to - 600 ms before the T0).

The underlying inter-laminar trans-synaptic current flows were mapped by CSD analysis (Nicholson & Freeman, 1975; Mitzdorf, 1985) using the *CSDplotter* MATLAB toolbox (Pettersen *et al.*, 2006) on the

signals (LFP) of the MLE. CSD analysis determines somatic or dendritic spatiotemporal synaptic activation in the form of depolarizing current sinks (Schaefer *et al.*, 2015).

To understand the role of the single-unit activities in the IISs, a spike sorting was carefully performed using an amplitude threshold (*Spike2*) on the bandpass filtered data (FIR filter 300-3000 Hz). An optimal threshold (>3 standard deviations) was applied to isolate the units properly from the background noise. Moreover, the refractory period (2 ms) was respected and principal component analysis (PCA) with the *k*-means algorithm applied.

To explore the spectral changes and correlation in the time-frequency domain, a wavelet coherence analysis was performed along paired channels of the MLE probe. The coherence values were emphasized. An average of the extraction of 200 windows (T0 ±1.5 s) for each subject was then performed for each rat. Then, z-score normalization was applied and the grand-average for all the results calculated. To extract significant variations in the coherence between deep and superficial channels, a time-frequency window was selected between (-1 to +1 sec; 5 to 9 Hz) with lower coherence values, and a t-test was performed with a baseline selected between -1.5 and -1 sec (5 to 9 Hz).

The TFR analysis was performed to describe phase-locked and non-phase-locked variations in neuronal activity occurring surround the IISs, for frequencies between 4 and 50 Hz. The same non-overlapping IIS epochs lasting 2 sec were considered for each IIS. The analysis of the ECoG signal was compared to the baseline segment, lasting 400 ms (−800 to −600 ms before T0). TFR analysis was performed on the window between −800 and + 800 ms around T0. This methodology was performed according to the procedures described by Hoechstetter et al. (Hoechstetter *et al.*, 2004). The TFR was calculated for each IIS epoch for all 16 contacts of the MLE. Frequencies were sampled (Gaussian filter) in 2-Hz steps, and windows were sampled in 25-ms steps, corresponding to a time-frequency resolution of ±2.83 Hz and ±39.4 ms for each time-frequency bin (full width at half maximum). In addition, TFRs were expressed as the relative power change relative to baseline activity for a time-frequency bin compared to the mean power over the baseline epoch for that frequency. This procedure generated TFRs containing phase-locked as well as non-phase-locked responses.

2.6.2. Optical data analysis

2.6.2.1. Cerebral hemodynamic activity

The modified Beer-Lambert law (McNaught *et al.*, 1997) were calculated to identify the concentrations of HbO_2 and HbR, based on the changes of absorption between two wavelengths (690 and

830nm), and performed by MATLAB-based Homer2 toolbox (https://homer-fnirs.org/). Total Hemoglobin (HbT) concentrations were calculated by summating the HbO_2 and HbR concentrations.

To avoid baseline slower drifts and cardiac artifacts, the hemodynamic signals were band-pass filtered (0.08 - 0.3 Hz, fourth-order, zero-phase-lag Butterworth filter). To quantify the hemodynamic changes, surround the IIS T0 in both brain hemispheres, a 40-sec window of HbO_2 and HbR concentrations data (±20 sec around T0) was averaged. The variations in hemoglobin occurring around the IIS were compared to the baseline segment (from −20 to −10 sec before T0).

2.6.2.2. Fast-optical signal

To calculate FOS, it needs to eliminate the noise, the cardiac artifacts, and the respiratory artifacts without shifting the signal delay. A high-pass zero-phase sixth-order low-pass and third-order Butterworth filters were used to remove respiratory artifacts from 2 to 20 Hz. Baseline correction from -800 to -600 ms was then applied. An independent component analysis (ICA) algorithm plus one classification method was applied to all filtered signals to almost eliminate cardiac artifacts. The periods (-800/+800 ms) surround the T0 of IISs were carefully chosen and then averaged. The t-test was performed with are significant difference of responses from baseline ($p < 0.05$).

2.6.2.3. Cerebral blood flow activities

The T0 of each IIS was selected as the zero time-point for the analysis of the regional CBF responses (rCBF). The hemodynamic response function (HRF) is a model that indirectly reflects neuronal activity in response to an event. The HRF shape with random noise, and the T0 times can be processed by linear convolution to extract a clear hemodynamic signal through relative close IISs (Osharina *et al.*, 2017). To create a similar calculation for the CBF, time-delayed impulses placed in intervals of 200 ms from 20 sec before to 20 sec after the T0 were placed in sets of data in a designed matrix XFIR. The objective was to determine the weight of each column of FIR that best explained the rCBF signal measured by the DCS system. Statistical significance was performed to know the precision of the parameter estimates along with the rCBF response function ($p < 0.001$).

To know the HRF components' changes in amplitude and latency, the deconvolution procedure was performed with a moving window of 200 IISs with an ISI of >1.5 sec to minimize the effect of the previous IIS on the hemodynamic response. The size of the moving window for 200 IISs was found to be optimal to keep the variability of the shape of the hemodynamic response related to IISs. The moving window was performed from the first IIS with a step length of one IIS. The noise covariance matrix was not calculated,

and the dynamic technique was applied to keep the slow variability in shape, amplitude, and latency of IISs with the moving average of IISs over time (Aarabi *et al.*, 2017).

2.7. Problem (s) encountered, and resolution (s) provided

Some problems that appear from the thesis starting point up to now were the next:

The first recordings were with a Deltamed® (Natus Europe GmbH) device, which is a clinical EEG system that measures ECoG, ECG and breathing. To move from this system to the more complex MLE was complex and had problems in the assembly and preamplification position and the channel mapping. These problems, after some recordings, were identifying them and providing solutions, like the integration of the physiological measures to the system, repositioning the preamplifiers and creating a new trigger in order to sync the NIRS with MLE system (November 2016).

During the different recordings and posterior data analysis, the MLE setup had a problem from the first recordings. Some noise was added at the signal than didn't allow us to see the data clean enough. In the way to solve it, we went to one laboratory at Grenoble (February of 2017) to improve our knowledge of how to recognize the noise in a similar setup to ours and how to solve it. After that productive visit, we add to our system a Faraday cage to don't allow the noise to get access to the system. From to find out a good one for our setup up to we receive it, it took around three months because it had some troubles of packaging and transportation from another Grenoble's laboratory to Amiens.

The signal had a better view after use our probe inside the Faraday cage, but our improved point of view about noise detection makes us question about than our Signal to Noise Ratio (SNR) still could be improved. For that reason, after reading different papers and ask some colleagues of other labs, we moved the multielectrode's reference from the neck-muscle to one surgical-screw placed in the occipital-bone surface, and it solved the problem (December 2017). Another way to continue improving the recordings, it was thanks to checking our multielectrode probe carefully could had a little loose during the recording, to solve it we change the probe's arm for another which is screwed directly to the adapter's probe (ADPT-NN-16) and wire it to the ground (March 2018) (Figure 2.14).

The ECoG and ECG channels did not record a clear signal. This problem was solved by editing the schema of the electrode's reference cable at the 15-pin SubD connector (September 2018).

All recordings were done by a *CED1401-3* interface, which one uses a private software. The issue was to transfer all the data recorded (neuronal and physiological) to *MATLAB* software to analyzing it. That software (*Spike2*) allows us to export it to *MATLAB,* but each time that we want to transfer it took us

a lot of time, and we lose part of the information integrity; even to synchronize the data it becomes hard. The solution was to produce our own code to transfer the data directly to MATLAB; it means that each new channel (filtered, virtualized, etc.) created in *Spike2* software could be used directly on MATLAB. It was not easy, but now it can easily import data without any troubles (it was a long-term problem and was solved in January 2018).

The recordings with DCS are improved to human clinical research but not for our protocol. DCS system has a powerful laser that is even capable of saturating the detectors. On the rat skull, the emitter and detectors don't have enough space to be placed for a correct acquisition. For that reason, before we could start any recording, it was mandatory to use a specialized attenuator to have the best signal of the blood flow (November 2018).

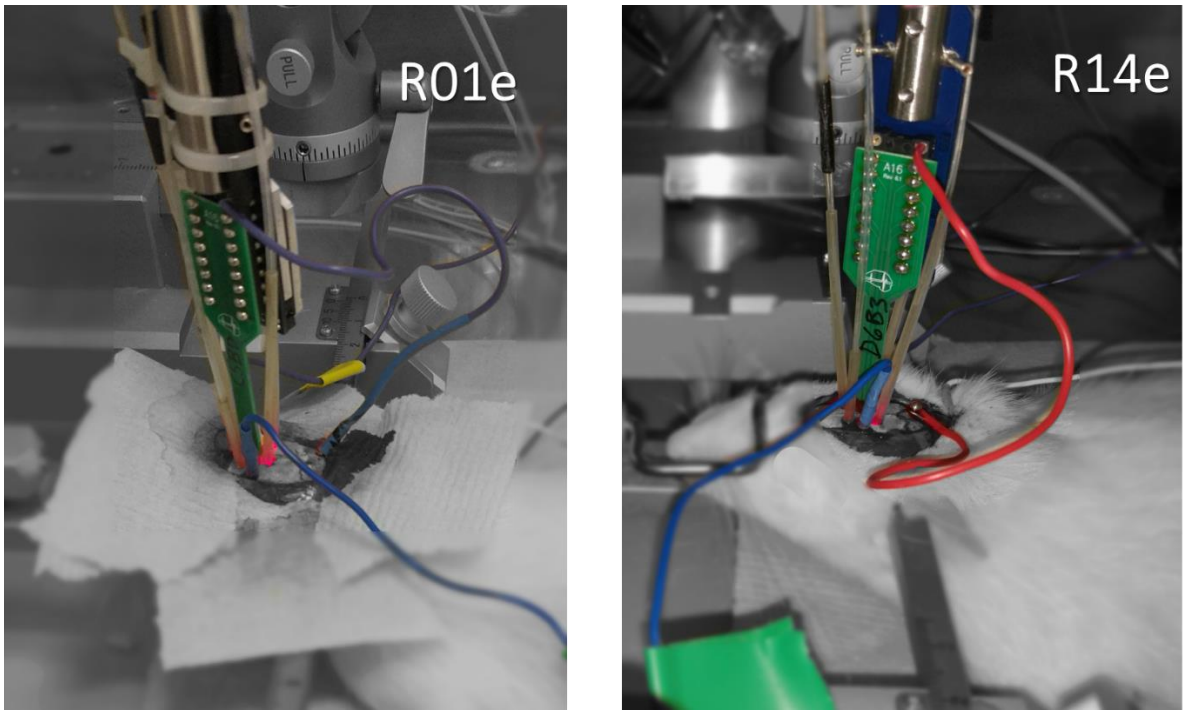

Figure 2.14. Photos of two rats (R01e before than R14e), highlighting the NIRS optodes and MLE+ECoG system in color, to show the evolution of the setup. The R01e setup had MLE subjected by plastic flanges, and the reference electrode touches the cerebellum; The R14e setup had a screwed subjection of MLE to the stereotaxic arm, and its reference is screwed at the occipital bone.

CHAPTER

3

Results: *What triggers the interictal epileptic spike? A multimodal multiscale analysis of the dynamic of synaptic and non-synaptic neuronal and vascular compartments using electrical and optical measurements*

Cristian Arnal-Real[1], Mahdi Mahmoudzadeh[1], Mana Manoocheri[1], Mina Nourhashemi[1], and Fabrice Wallois[1]

Adresse[1]: Inserm U1105, GRAMFC, CURS, Université de Picardie Jules Verne, Amiens, France

Keywords: hemodynamic, multiunit activity, pre-spike, non-synaptic, extracellular space, wavelet coherence, time frequency analysis, current source density, fast optical imaging, cerebral blood flow.

Acknowledgments: This work was funded by the European Regional Development Fund and the Picardie region under the project SPIKE.

3.1. Key points

- A multimodal multiscale analysis (ECoG, LFP-MUA, NIRS, DCS) was performed on penicillin-induced interictal epileptic spikes in rats

- Hemodynamic activities are modified well before (5s) the interictal spike (IIS)
- Between the cortical layers, interactions are modified approximately 1 s before the IIS
- The onfiguration of the cell membranes is modified approximately 0.5 s before the IIS
- Our results highlight the complex interactions that occur before the IIS at different scales and in different compartments (synaptic, non-synaptic, and vascular)

3.2. Abstract

Interictal spikes (IISs) may result from a disturbance of the intimate functional balance between various neuronal (synaptic and non-synaptic), vascular, and metabolic compartments.

To better characterize the complex interactions within these compartments at different scales we developed a simultaneous multimodal-multiscale approach and measure their activity around the time of the IIS. We performed such measurements in an epileptic rat model (n=43). We thus evaluated (1) synaptic dynamics by combining electrocorticography and multiunit activity recording in the time and time-frequency domain, (2) non-synaptic dynamics by recording modifications in light scattering induced by changes in the membrane configuration related to cell activity using the fast optical signal, and (3) vascular dynamics using functional near-infrared spectroscopy and, independently but simultaneously to the electrocorticography, the changes in cerebral blood flow using diffuse correlation spectroscopy.

The first observed alterations in the measured signals occurred in the hemodynamic compartments a few seconds before the peak of the IIS. These hemodynamic changes were followed by changes in coherence and then synchronization between the deep and superficial neural networks in the 1 s preceding the IIS peaks. Finally, changes in light scattering before the epileptic spikes suggest a change in membrane configuration before the IIS.

Our multimodal, multiscale approach highlights the complexity of (1) interactions between the various neuronal, vascular, and extracellular compartments, (2) neural interactions between various layers, (3) the synaptic mechanisms (coherence and synchronization), and (4) non-synaptic mechanisms that take place in the neuronal network around the time of the IISs in a very specific cerebral hemodynamic environment.

3.3. Introduction

Epilepsy is a common disorder of the central nervous system that affects approximately 0.6% of the global population (Banerjee et al., 2009, Anon, 2019; Feigin et al., 2019), making it an important public health issue. Many aspects of its pathophysiology are still poorly understood and current knowledge is often fragmented. Epilepsy, whether in animals or humans, can be investigated by neuronal (electroencephalography (EEG), electrocorticography (ECoG), magnetoencephalography (MEG), unit activity (UA), multiunit activity recording (MUA), Intracellular recordings), hemodynamic (functional magnetic resonance imaging (fMRI), functional near infrared spectroscopy (fNIRS), intrinsic optical imaging (IOI), etc.), structural (magnetic resonance imaging (MRI)), metabolic (positron emission tomography (PET), single photon emission computed tomography (SPECT)), and semiological information. Two phases are commonly distinguished in epilepsy, the ictal phase and the interictal phase.

The ictal phase is characterized by clinical or subclinical seizures, the diagnosis of which is electro-clinical, often combining EEG analysis and a clinical report of the semiology of the seizures.

The interictal phase, between seizures, is mainly studied by analyzing brain dysfunction by EEG. The interictal phase is characterized by certain electrical signatures of the dysfunctioning underlying networks, such as transient pathological graphological elements, including interictal spikes (IIS), poly-spikes, and spike waves, associated or not with disorganization of the background brain activity. The occurrence of IIS within epileptic networks is generally related to changes in the excitability threshold by the interaction of synaptic (excitatory and/or inhibitory) and non-synaptic ([K+], ephaptic conduction, cellular environment, etc.) mechanisms that propel the neural network to transient hypersynchronization (De Curtis & Avanzini, 2001). Certain types of epilepsy have a structural origin, whereas others result from the dysfunction of neural networks related to genetic, metabolic, or vascular origins and/or neuronal communication (Scheffer et al., 2017). Such interictal events are considered to result from synaptic and non-synaptic mechanisms, leading to cognitive and sensorimotor dysfunction associated with disorganization of the neuronal communication between different cortical and subcortical structures (Castro-Alamancos, 2000; De Curtis & Avanzini, 2001; Castro-alamancos et al., 2007). It is still unknown why an interictal spike (IIS) emerges at a specific time and not another.

We hypothesize that the emergence of interictal epileptic spikes results from a disturbance of an intimate functional balance between various neuronal (synaptic and non-synaptic), vascular, and metabolic compartments.

(1) **Synaptic compartment**: Epileptic spikes are underpinned by complex neuronal inhibitory and excitatory interactions between deep and superficial cortical layers (Castro-Alamancos, 2000). These interactions can be analyzed by multi-unit activity (MUA) recordings, which allow assessment of the ion fluxes between sinks and sources across the various cortical layers (Castro-Alamancos, 2000; Ulbert et al., 2004). The analysis of multi-unit activity can be carried out by the same multielectrode recordings and highlights the characteristics of various unitary activities associated with the epileptic spikes recorded at the cortical surface. Such measurements highlight the complexity of the involved neuronal activation/inhibition (Keller et al., 2010). The neurons that participate in epileptic spikes are characterized by a paroxysmal depolarization shift (PDS) of 40 to 400 ms (Matsumoto & Marsan, 1964) at the plateau, to which action potentials are added (Hotka & Kubista, 2019). They are generated and facilitated by the emergence of an initial rebound linked to the prior activation of inhibitory interneurons, located in the deeper layers, that produce high frequency oscillations tens of milliseconds before the PDS (Cobb et al., 1995; De Curtis & Avanzini, 2001).

(2) **Non-synaptic compartment**: Non-synaptic disturbances are likely to contribute to IISs. Among various non-synaptic events (including communication across gap junctions) that facilitate neuronal activation during the IIS, neural activation causes cellular and glial swelling that can reduce the extracellular space (McBain et al., 1990; Andrew & Macvicar, 1994) and increase field interactions through ephaptic communication between neurons. Such shrinking of the extracellular space induces an increase in extracellular potassium levels (Jensen et al., 1994, 1996) that are observed during interictal spiking (De Curtis et al., 1998). This enhances membrane depolarization and intrinsic burst firing by reducing the ionic transmembrane driving forces during the activation of repolarizing potassium conductance and by shifting the reversal potential of inhibitory synaptic potentials toward more positive values (see de (De Curtis & Avanzini, 2001) for review). A number of studies have demonstrated that such cellular swelling can modify photon scattering and therefore be evaluated by the fast-optical signal (FOS) technique, which shows high temporal resolution (Gratton & Fabiani, 1998). The application of this technique to epileptic spikes has

allowed the demonstration of changes in light scattering (increase-decrease-increase), suggesting an increase-decrease-increase cycle of the extracellular space at the time around the IIS (-300, + 300 ms) (Manoochehri et al., 2017b).

(3) **Vascular compartment**: The neurovascular coupling induced by IISs has been widely studied and has shown that the duration and frequency of IISs modulate hemodynamic responses that can be measured in animals by intrinsic optical signals or in humans by fMRI (Osharina et al., 2010, 2017; Gotman & Pittau, 2011). The same is true for the increase in cerebral blood flow (CBF), which is also modified secondarily to an IIS, as observed by laser Doppler flow (LDF) (Saillet et al., 2016a). However, several studies have demonstrated hemodynamic changes (oxyhemoglobin (HbO2) and deoxyhemoglobin (HbR)) prior to epileptic spikes (5-6 s) in animals using fNIRS (Osharina et al., 2010, 2017) and in humans using fNIRS (Wallois et al., 2010) and fMRI (Hawco et al., 2007; Jacobs et al., 2009; Gotman & Pittau, 2011), suggesting that not only is there neurovascular coupling linked to activation of the IIS but also that cerebral hemodynamics are disturbed well before the IIS.

Questions to be addressed

Here, we developed a multimodal-multiscale approach to address several issues.

(1) The mechanisms (synaptic, non-synaptic, hemodynamic) that are likely to contribute to the emergence of epileptic spikes in a longer time frame than that of the early activation of inhibitory interneurons.

(2) The dynamics of the various compartments around the IIS.

(3) Whether such multimodal multiscale analysis can provide new information on the mechanisms that propel neurons to the hyperactivation and synchronization that results in an epileptic spike.

(4) The type of information time-frequency analysis, combined with wavelet coherence analysis, of the interaction between the different layers before the IIS can provide.

(5) Whether the complexity of the neuronal activation/inhibition described in human studies (Keller et al., 2010) can be observed in epileptic rats.

(6) Whether the previously described hemodynamic changes in HbO2 and HbR around the time of the IIS are associated with changes in CBF.

(7) Whether individual neuronal activity modifies their rate of discharge simultaneously with the hemodynamic changes that occur prior to the epileptic spikes recorded at the surface.

(8) The neuronal and hemodynamic environment in which changes in cellular configuration occur.

(9) Whether such simultaneous changes in cell configuration have a neuronal or hemodynamic counterpart.

Multimodal approach

We developed a multimodal approach to study the various compartments in epileptic rats to address these issues using techniques that offer good time resolution. This multimodal multi-scale approach allows a better understanding of the emergence of interictal epileptic spikes as signatures/biomarkers of epileptic disorders.

(1) We evaluated the **synaptic** dynamics (i.e. analysing the activity of the epileptic neuronal network) by combining ECoG and multi-unit activity recordings of different cortical layers. We further developed a time-frequency analysis (TFR) of the local field potential (LFP), consisting of an analysis of the current source density (CSD) and wavelet coherence analysis of the neuronal interaction between different layers, together with an analysis of the rate of discharge of unitary recordings.

(2) We evaluated the **non-synaptic** dynamics, specifically changes in the extracellular space, by recording modifications in light scattering induced by changes in the membrane configuration related to cell activity using the FOS technique.

(3) We evaluated the **vascular** activity (hemodynamic changes around the IIS) by simultaneously recording the changes in HbO2 and HbR using fNIRS and, independently but simultaneously to ECoG, the changes in CBF using diffuse correlation spectroscopy (DCS) recordings.

Our main objective was to characterize the concomitance of the neuronal, hemodynamic, and/or cellular configuration changes that occur around the IIS using a multimodal multi-scale approach. Our multimodal approach follows clinical practice by building a body of evidence from all clinical,

structural, hemodynamic, and metabolic data using paraclinical examinations such as EEG, MEG, SEEG with MUA, MRI, fMRI, PET, and SPECT and sometimes by combining these analyses (EEG / fMRI , SPECT / fMRI, EEG / MRI, PET / CT-Scan, PET / MRI) with semiological information.

3.4. Materials and Methods

3.4.1. Animals

Recordings were made on 43 male adult Sprague-Dawley (Blackthorn, Bicester, UK) rats (260 and 550 g) using a multimodal-multiscale approach (Table 1). The rats were housed in a temperature-controlled room with a regular light/dark cycle and fed standard rat chow and tap water *ad libitum*. The protocol was approved by the Ethics Committee of the French Ministry of Research (ref: APAFIS#1464-2015081710033478). Every effort was made to limit the number of rats and their suffering.

Table 1. Number of rats for each protocol.

Protocol	Nb. of Recordings	Weight
ECoG + NIRS	13	403.92
ECoG+ MLE + NIRS	11	428.21
MLE (alone)	4	537.50
ECoG + MLE + DCS	15	348.27
Total	43	

3.4.1.1. Animal preparation

Each rat was weighed and anesthetized using urethane (1.25-1.5 g/kg) with a single intraperitoneal injection. The body temperature and respiratory and heart rates were monitored during the experimental procedure to follow the vital signs of the rats and the level of anesthesia. Tracheotomy was not required since respiratory rate was not altered during the recording period. Approximately 1 h after the injection, the surgical protocol was started. Part of the scalp was removed and the animal was placed in a stereotaxic frame to expose the skull. A 10 x 15-mm field of bone was exposed, the periosteum removed, and eight craniotomy holes (diameter of 1.5 – 2 mm) drilled at determined coordinates (Figure 1a). A small incision was carefully made on the dura mater for each hole to insert the multielectrode and optical probes. Care was taken to avoid any damage to vessels and surrounding tissues during probe insertion.

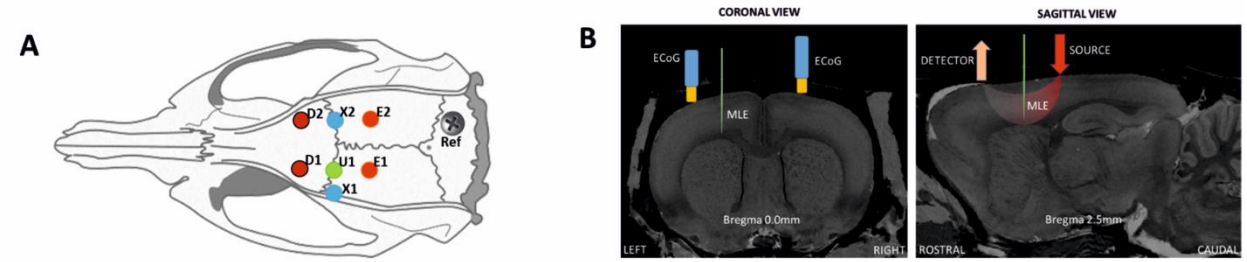

Figure 1. Schematic representation of the location of ECoG and optical probes on a rat head. (A) Positions for optical probes, MLE, and ECoG electrodes in the rat cortex: D1 and D2, detectors of the spectrometers (anterior-posterior (AP) 2.5 mm medial-lateral (ML) 2.5 mm); E1 and E2, correspond to the position of emitter 1 (ipsilateral) and emitter 2 (contralateral). ECoG electrodes (X1 at AP 0 mm ML 3.5 mm; X2 at AP 0 mm ML 2.5 mm); and U1, multi-site linear electrode (AP 0 mm ML 2.5 mm), with its reference. (B) Coronal and sagittal views in the MRI atlas for Sprague-Dawley rats (Papp et al., 2014). Left side: the MLE and ECoG electrodes at Bregma 0.0 mm, coronal slice. Right side; detector and light source optode placement with MLE, sagittal slice (Bregma 2.5 mm).

MLE electrodes were placed at half the distance between the emitters and detectors to probe the trough of the banana shape made by the photon pathway. The position of the MLE was the same as the penicillin G injection site (U1). First, to minimize errors related to probing different neuronal populations, the ECoG electrodes, which were always present, were located as close as possible to the MLE site as a control measurement. The distance between the MLE and ECoG holes was only a few millimeters. The position of EcoG electrodes are therefore not completely symmetric. For injection and MLE electrode placement, the EcoG has to be slightly moved laterally. Although, EcoG were only used as control for the LFP recorded on the most superficial MLE channel that was used as an "ECoG" like electrode for further analysis and for the zero signal alignment of the different multimodal measurements (peak of the IIS). Second, the injected penicillin G probably spread to adjacent areas. Third, it is well known that an IIS recorded at the surface (EEG and to a lesser extent ECoG) are supported by a relatively wide area of synchronized neurons. It is therefore very likely that the region involved in the epileptic discharge recruited neurons located in a relatively wide area encompassing the structures probed by the various modalities. Because ECoG and the most superficial electrodes provide the same information (see the following figure), the most superficial channel of the MLE was used as the reference electrode instead of the ECoG electrode. This allows using the same sampling rate and facilitates the further analysis.

Three electrocardiogram (ECG) electrodes were positioned (two in the skin of the front paws and one in the skin of the left-rear paw) to monitor the vital signs of the animals. A piezoelectric device was placed beneath the ventral side of the rat (close to diaphragm) to monitor respiration. A body

temperature of 36 to 38ºC was maintained by inserting a rectal thermometer connected to a proportional integral derivative (PID) to control a heating pad. At the end of the experiment, the rats were killed by urethane overdose following the guidelines for animal euthanasia of the animal facility.

3.4.2. Penicillin injection

Penicillin blocks GABAA receptors (Rossokhin et al., 2014), which mainly participate in rapid inhibitory neurotransmission. A dose of penicillin G (Sigma) was applied to the cortex through the hole located over the left hemisphere (anteroposterior (AP) 0 mm and medial-lateral (ML) 2.5 mm from Bregma) to evoke IISs. The dura mater of the hole was removed to faciliate drug absorption by the neural tissue and a volume of 6 to 8 µL (1000 – 1500 units) penicillin was expulsed mechanically by a glass micropipette (Hamilton®) and allowed to flow over the cortical surface. The doses of penicillin were determined based on values obtained from the literature (Matsumoto & Marsan, 1964; Soukupová et al., 1993; Akdogan et al., 2008; Silfverhuth et al., 2011). Recordings started 20 min before infusion and continued for 3 to 4 h after. The first IISs appeared approximately 4 to 8 min after administration, their firing rate increasing over approximately 20 min. If IISs were not induced by the initial dose of penicillin, an additional dose of 2 µL was administrated.

3.4.3. Data acquisition

Data were recorded by a combined multimodal multiscale approach using multi-site linear electrodes (MLE), ECoG, functional fNIRS, FOS, and DCS. An external TTL trigger was used between the electrophysiological (MLE, ECG, ECoG, respiration, body temperature) and hemodynamic measurement systems (fNIRS, FOS, DCS) to synchronize the recording devices. All recordings were performed in a dark room and monitored in an adjacent room to not interfere with the acquired signal.

3.4.3.1. Electrophysiological measurement (MLE, ECoG)

The 16-site MLE (A1x16-5mm-150-177, NeuroNexus) was inserted 2.5 to 3 mm at an angle of 90º to the cortical surface to record the entire columnar cortex (6 layers) (Figure 1b). Each MLE (33-µm shaft diameter) spanned a cortical column, with the base in layer I and the tip in layer VI, with 16 individual recording sites (177 µm2) spaced 150 µm apart. Introduction of the device was

carefully performed to avoid any neuronal damage caused by excessive insertion speed and damage to the MLE by any bone sliver from the trepanation. The condition of the electrodes was verified before each experiment and they were cleaned as required with an enzymatic detergent. The reference electrode was inserted through the right part of the occipital bone, through a stainless-steel screw. The MLE probe was mounted on a probe holder attached to a manual micro-manipulator (WPI, World Precision Instruments) grounded to a Faraday-cage. After MLE probe insertion, the ECoG monopolar gold-plated electrodes were inserted into the appropriate holes almost perpendicular to the cortical surface, with a reference needle electrode inserted in the neck muscle. The MLE and ECoG signals were then amplified by a multi-channel system setup and acquired by a CED 1401 (Cambridge Electronic Design Ltd.) acquisition-board interface. The MLE and ECoG signal sampling rates were set to 20 kHz and 1,024 Hz per channel, respectively. The raw signal of the deeper MLE channel was filtered online (300 - 3000 Hz, IIR filter) to monitor the multi-unit activity during each recording.

3.4.3.2. Optical measurements (fNIRS, FOS, DCS)

The optical measurement for monitoring changes in light absorption (changes in [HbO2] and [HbR]) were performed by fNIRS (Imagent□, ISS Inc.), whereas changes in light scattering (changes in membrane properties) were performed by FOS (Imagent□, ISS Inc.). The near-infrared (NIR) intensity fluctuations were measured by DCS (Neuro-Monitor-FloMo, Hemophotonics SL, Spain).

3.4.3.2.1. Cerebral hemodynamics (fNIRS) and changes in cellular configuration (FOS)

The fNIRS system is a frequency-domain spectrometer, with emitters modulated at 110 MHz. The sampling frequency of the detectors was set to 156.25 Hz to gain access to changes in light absorption (fNIRS) and light scattering (FOS). The cerebral hemodynamic activities were measured by fNIRS by placing one pair of optical fiber light emitters (each pair with 690 nm and 830 nm wavelengths) caudally from Bregma AP -2.5 mm to ML 2.5 mm over both hemispheres. Their respective optical fiber light detectors were placed rostrally from Bregma AP +2.5 mm to ML 2.5 mm over both hemispheres. The optodes were inserted into the holes and secured perpendicularly to the cortical surface. A distance of 5 mm was set between each emitter and

detector pair to probe a banana-shaped photon trajectory corresponding to the desired deepness of 1.7 mm (one-third of the emitter-detector distance (Pogue et al., 1995)).

3.4.3.2.2. Cerebral blood flow (DCS)

A DCS device was used to invasively quantify changes in CBF. The DCS measures blood flow by optical modality using intensity fluctuations of NIR light (Nourhashemi et al., 2016). The light scattered by the movement of red blood cells inside the vessels cause temporal fluctuation of the detected light intensity. The time lag of such fluctuations is quantified by the intensity-time autocorrelation function of the detected light (Durduran et al., 2010a). The correlation diffusion equation is applied to fit the autocorrelation function to calculate a CBF index (CBFi) (Durduran et al., 2010b). Neuro-monitor-FloMo (Hemophotonics SL, Spain) consists of a narrow-band CW laser (785 nm, Crystalaser Inc., NV) with a long coherence length (> 50 m), with fast photon-counting avalanche photodiodes (APD) (SPCM-AQR-14-FC, Pacer Components Inc., UK) and a channel autocorrelator board (Flex03OEM-4CH, Correlator Inc., NJ). In our setup, one emitter-detector pair was positioned on the left hemisphere cortex (at the same holes as for the fNIRS) and fixed at 90º. An adjustable light attenuator was added at the laser source output to avoid DCS detector saturation. The DCS sampling frequency was set tothe maximum sampling rate available of 2.5 Hz (e.g. 1 sample every 0.46 s)., The ECoG-fNIRS and ECoG-DCS co-recordings were performed in two separate sessions due to optical crosstalk between the two optical measurement devices (i.e. fNIRS and DCS).

3.4.4. Data analysis

3.4.4.1. Electrophysiological data

We wished to evaluate the changes in electrical, hemodynamic, and cellular configuration around the IIS. Thus, the first step was to define T0. The IIS peaks were identified using the signal of the MLE channel closest to the surface of the cortex. As commonly observed in penicillin rat models (Holmes et al., 1987; Vongerichten et al., 2016), the shape of the IISs consists of a sharp negative peak followed by a positive slow wave. Time zero (T0) was defined as the peak of each IIS. T0 was extracted by downsampling the signal (from 20 kHz to 1 kHz) and then applying a finite impulse response (FIR) bandpass filter (1-35 Hz). The IISs were then detected (Spike2, Cambridge Electronic Design, CED). IISs were detected semi-automatically and clustered using a template-matching technique (Spike2). All IISs with < 80% of the points inside the template were rejected.

We selected the population of IISs that fulfilled the objective of the analysis of the 500-ms pre-spike period (baseline between -800 to -600 ms) by characterizing the firing rate, inter-spike interval (ISI), and spike amplitude. First, the dispersion of the firing rate of the IIS was evaluated by calculating the coefficients of rhythmicity of the firing rate for each rat. $CV = (\sigma / \bar{x}) \cdot 100\%$, where σ is the standard deviation of the IIS firing rate and $\bar{x}$ the mean of the IIS firing rate. The impact of the time interval between two spikes (ISI) on the proportion of the neuronal population involved in the generation of the IIS (amplitude) was evaluated by contrasting the ISI against the amplitude of the IIS for each rat. Then, the individual amplitude was normalized to develop a heat map to highlight the spot density of the relationship between the normalized amplitude and the ISI values to group all the rats in a single analysis. Kolmogorov–Smirnov tests were used on the histograms to clarify the tendency of the normalized peak voltage and the ISI from 0 to 5 s.

Non-overlapping IIS epochs lasting 3 s (-1.5; +1.5 s) were considered for each IIS set to avoid, or at least minimize, the effect of the previous IIS.

The LFP signal of the superficial channel was averaged for each rat. No filtering was applied in order to investigate all variations or calculate their average amplitude, with or without the 1.5 s of isolation. The underlying inter-laminar trans-synaptic current flows were mapped by current-source density (CSD) (Nicholson & Freeman, 1975; Mitzdorf, 1985) analysis using the CSDplotter MATLAB toolbox (Pettersen et al., 2006) on the LFP signals. CSD determines somatic or dendritic spatiotemporal synaptic activation in the form of depolarizing current sinks (Schaefer et al., 2015).

Power changes of the neuronal activity related to the IISs were quantified by averaging the root mean square (RMS) of the LFPs ± 1.5 s around T0 for each rat independently. Finally, all data were averaged and the difference between the superficial and deep channels evaluated.

A Bonferroni corrected t-test was applied to the LFP (baseline - 800 to - 600 ms before the IIS peak) to evaluate the point at which the changes in LFP signal became significant.

Single unit activity was carefully sorted using an amplitude threshold (Spike2) on the filtered data (bandpass FIR filter 300-3000 Hz) An optimal threshold (>3 standard deviations) was applied to isolate the events correctly from the background noise. Moreover, the refractory period (2 ms) was respected and principal component analysis (PCA) with the k-means algorithm applied.

A wavelet coherency was applied to each possible pair of MLE recording probe sites to investigate the spectral perturbations and correlation in the time-frequency domain. The coherence values were highlighted and their phase amplitude plotted with arrows. An average analysis, based on the extraction of 200 windows (T0 ±1.5 s) for each rat, was then performed and averaged for each rat. Then, z-score normalization was applied and the grand-average for all the results calculated. To extract significant changes in the cohenrence between deep and supeficial channels, a time-frequency window was selected between (-1 to +1 s; 5 to 9 Hz) with lower coherence values and a t-test was performed with a baseline selected between -1.5 and -1 s (5 to 9 Hz).

3.4.4.2. Time-Frequency representation (TFR)

Time-frequency analysis was performed for frequencies between 4 and 50 Hz to characterize phase-locked and non-phase-locked changes in neuronal activity that occurred around the IISs during each selected epoch. The same non-overlapping IIS epochs lasting 2 s were considered for each IIS. The TFRs of ECoG activity were compared to the baseline segment, lasting 400 ms (−800 to −600 ms before T0 of each IIS). Time-frequency analysis was performed on the window between −800 and + 800 ms around T0. TFR was performed according to the procedures described by Hoechstetter et al. (Hoechstetter et al., 2004) and implemented in BESA Research®. The time-frequency representation was calculated for each IIS epoch for all 16 contacts of the MLE. Frequencies were sampled (Gaussian filter) in 2-Hz steps and windows were sampled in 25-ms steps, corresponding to a time-frequency resolution of ± 2.83 Hz and ±3 9.4 ms for each time-frequency bin (full width at half maximum). In addition, TFRs were expressed as the relative power change from baseline activity for a time-frequency bin compared to the mean power over the baseline epoch for that frequency, TFR = {P(t,f)−Pbaseline(f)}/Pbaseline(f) x 100 where P(t,f) = power at time t and frequency f and Pbaseline(f) = mean activity at frequency f over the baseline epoch. This procedure yielded TFRs containing phase-locked as well as non-phase-locked responses.

3.4.4.3. Optical data analysis

3.4.4.3.1. Cerebral hemodynamic activity

The concentrations of HbO2 and HbR were calculated using the modified Beer-Lambert law (McNaught et al., 1997), based on the difference of absorption between two wavelengths (690 and

830nm), with the MATLAB-based Homer2 toolbox (https://homer-fnirs.org/). Hemoglobin (HbT) concentrations were calculated by summing the HbO2 and HbR concentrations.

The HbO2 and HbR concentrations were band-pass filtered (0.08 - 0.3 Hz, order 4, zero-phase-lag Butterworth filter) to reject very slow drift of the baseline and cardiac artifacts. Hemodynamic changes around IIS activity in the ipsilateral and contralateral hemispheres were studied by deconvolution within a 40-s window of hemoglobin concentration data (±20 sec around T0). The changes in HbO2 and HbR occurring around the IIS were compared to the baseline segment (lasting −20 to −10 s before T0).

3.4.4.3.2. Fast-optical signal

Compared to other physiological signals, FOS is so small that it cannot be observed directly. These signals need to be separated from the noise, for which the signal may be several orders of magnitude larger. Cardiac artifacts are the most common and powerful physiological artifacts that affect optical signals. Respiratory artifacts were eliminated without shifting the signal delay using sixth-order low-pass and third-order high-pass zero-phase Butterworth filters to filter the signal between 2 and 20 Hz. Baseline correction from -800 to -600 ms was then performed. Cardiac artifacts were eliminated by applying an independent component analysis (ICA) algorithm plus one classification method to all filtered signals, almost eliminating such noise. The epochs (-800/+800 ms) around the peak of the T0 spikes were selected and then averaged. Finally, time bins were designated with a significant difference of responses from baseline ($p < 0.05$) by applying t-tests.

3.4.4.3.3. Cerebral blood flow activities

First, all recorded IISs on ECoG data were detected automatically. The negative peak (T0) of each IIS was detected as the zero time-point for the analysis of the regional CBF responses (rCBF) associated with the IISs. ISIs were defined as the time-course of IIS sequences. The hemodynamic response function (HRF) is a model that indirectly reflects neuronal activity in response to an event. In general, a measured hemodynamic signal can be modeled as the linear convolution between the explicit timing of events and a specific shape of the HRF, with additive noise (Figure 2a) (Osharina et al., 2017). Then, to estimate the HRF of CBF, we used a form of the FIR design matrix XFIR composed of sets of time-delayed impulses separated by intervals of 200 ms from 20

s before to 20 s after the spike peak. The purpose was to determine the weight of each column of XFIR that best explained the rCBF signal measured by the DCS system (y).

$$y = X_{FIR} \cdot \beta_{FIR}$$

where β_{FIR} are the weights of each column of the FIR design matrix.

We set the values of β_{FIR} by minimizing the sum of the squared errors (SSE) between the FIR model and the actual measured rCBF signal (y) as follows:

$$SSE = \sum_{i}^{N} \left(y^{(i)} - X_{FIR}^{(i)} \right)^2$$

$$\beta_{FIR} = (X_{FIR}^T X_{FIR})^{-1} X_{FIR} y$$

where X_{FIR}^T is the transpose of the design matrix (Figure 2b). The grand average of the weighted basis functions was calculated over the entire rCBF response function time-course. The accuracy of the parameter estimates across the rCBF response function was measured by the statistical significance ($p < 0.001$).

As a complementery analysis, the variability of the amplitude and latency of the HRF components was investigated by applying the dynamic approach of the deconvolution procedure using a moving window of 200 IISs. A moving window of 200 IISs was found to be optimal for maintaining the variability of the shape of the hemodynamic responses related to IISs. The moving window was applied from the first spike in the ECoG recording with a step length of one spike (Figure 2c). As in the FIR model, the noise covariance matrix was not estimated and the dynamic technique was applied to accommodate the slow variability in shape, amplitude, and latency of the IISs using the moving average of the IISs over time. In addition to the choice of the deconvolution method for the analysis of hemodynamic activity (see below), a minimum ISI of 1.5 s was selected to further minimize the effect of previous spikes on the hemodynamic response (Aarabi et al., 2017).

The changes in DCS around the IIS were compared to the baseline segment (−20 to −10 ms before T0).

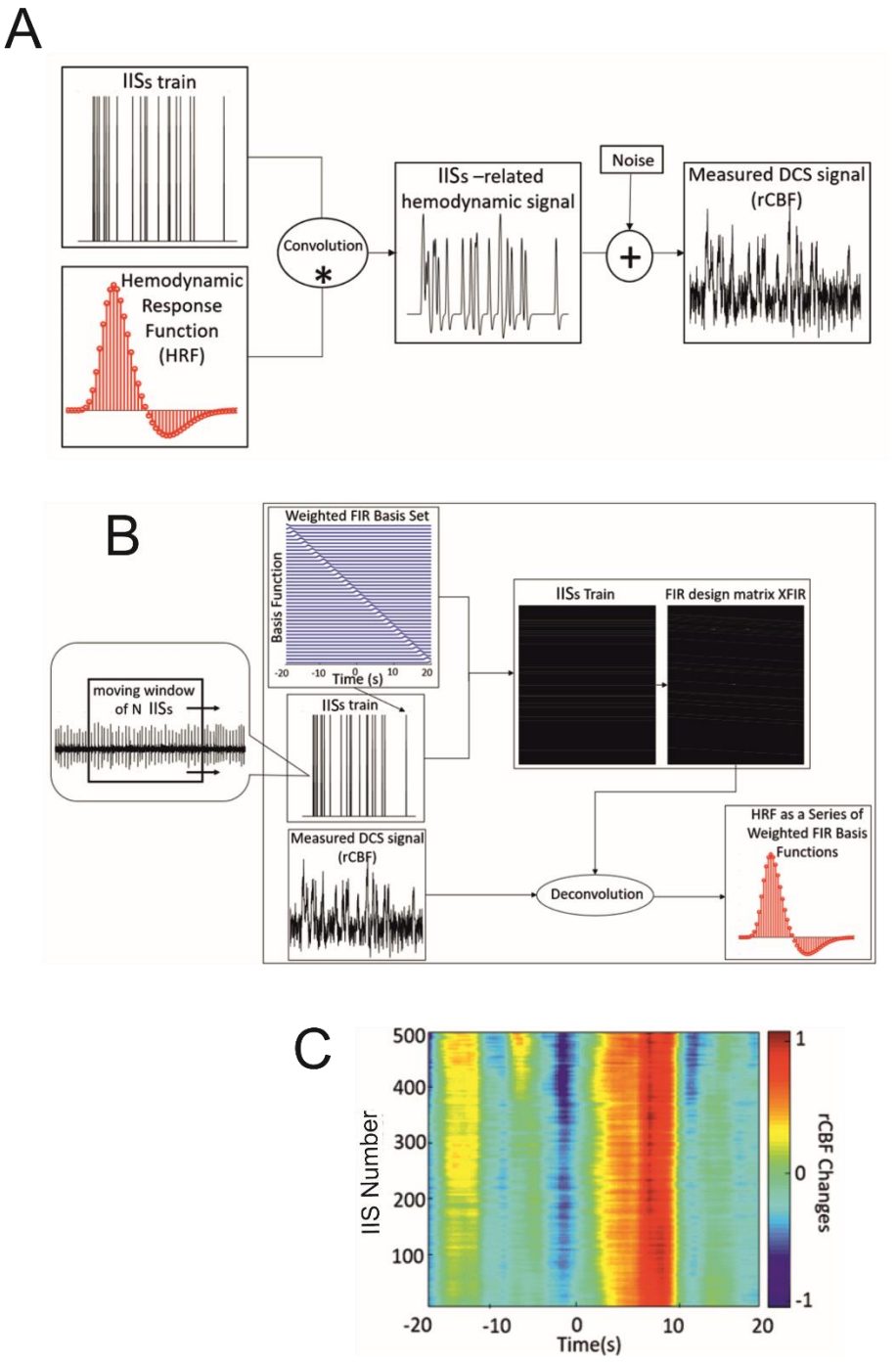

Figure 2. (A) Linear convolution between an IIS train and the canonical HRF. (B) Deconvolution between the measured hemodynamic response and FIR design matrix X_{FIR}, which is composed of sets of time-delayed impulses separated by intervals of 200 ms (from −20 to 20 s) around the spike peaks. Dynamic approach of the deconvolution method used for IIS averaging (with a moving window of *n* IISs) and estimation of the hemodynamic response. (C) Time-course of rCBF changes for one rat using the dynamic FIR method.

3.5. Results

IISs were successfully induced by penicillin injection in all rats. The brain activity before the injection of penicillin was similar in all rats, characterized by the absence of IISs and a background activity dominated by low frequencies (1 to 3 Hz). The IISs appeared 4 to 8 min after penicillin injection. In total, 32 hours were recorded, and 38,627 IISs sorted in 20 rats recorded with MLE (1,931 ± 947 IISs).

3.5.1. IIS characterization

IISs were easily reproducible and generated spike sequences with similar shapes and amplitudes. They were characterized by a large-amplitude rapid component of 50 to 100 ms that was usually followed by a slow wave, with a duration of 200 to 500 ms (Kooi, 1966; Chatrian et al., 1974). ISIs were in the same range as previously reported (Osharina et al., 2017). The coefficient of rhythmicity was below 25% for 13 of 20 rats (Table S1). The coefficient of rhythmicity stayed below 35% for all but one of the seven remaining rats (84.2%). The average of all selected IISs for the 20 rats showed a duration of 2.7 ± 1.3 s and a peak amplitude of 1,066 ± 473 µV (Figure 3B). Most of the spikes had an ISI of < 5 s. We therefore selected the IISs with ISIs of < 5 s for each rat. We then selected 700 IISs that fit this condition for each rat to avoid a population effect related to a different number of IISs in different rats. In total, 13,300 IIS were used for further analysis. The amplitudes and firing-rates were not normally distributed (Figure 3A) (Kolmogorov–Smirnov test $p < 0.001$). The histogram peak values of the normalized amplitudes and ISI values (0.7, 2.16 s, respectively) were positively skewed for the ISI distribution (S = 0.54) and negatively skewed for the normalized amplitude (S = -0.41), emphasizing the non-normal distribution of the data. A correlation analysis was carried out between the normalized amplitudes and related ISIs (Figure 3A). The interquartile range values for the ISIs were between 1.71 and 2.9 s and 0.48 to 0.73 for the normalized amplitudes. The density analysis showed that 26.31% of IISs (3,554 of 13,300 IISs) fit within the interquartile range of the amplitudes and ISIs. The density of the points was maximum around the peak values of the histogram of the normalized ISIs and amplitudes (> 90%) (Figure 3A).

The correlation pattern between the ISIs and amplitudes varied between rats. In several rats (n = 5), the distribution was bimodal, with the first peak of the ISIs between 300 and 750 ms, with a relatively higher amplitude than that of the ISIs occurring after nearly 1 s (Figure 3B, rat 18),

which could correspond to polyspikes. In this case, a delay of 1 s likely corresponded to a refractory period observed after these polyspikes. In most cases, the bimodal distribution was less obvious and could change during the course of the recording (Figure 3B, rat 10). Finally, only spikes with an ISI > 1.5 s were selected for further analysis to provide a homogenous population of IISs (excluding polyspikes) and reduce the impact of too closely preceding IISs, which could possibly affect the analysis of the pre-spike period (-320 ms, based on our previous study (Manoochehri et al., 2017b)).

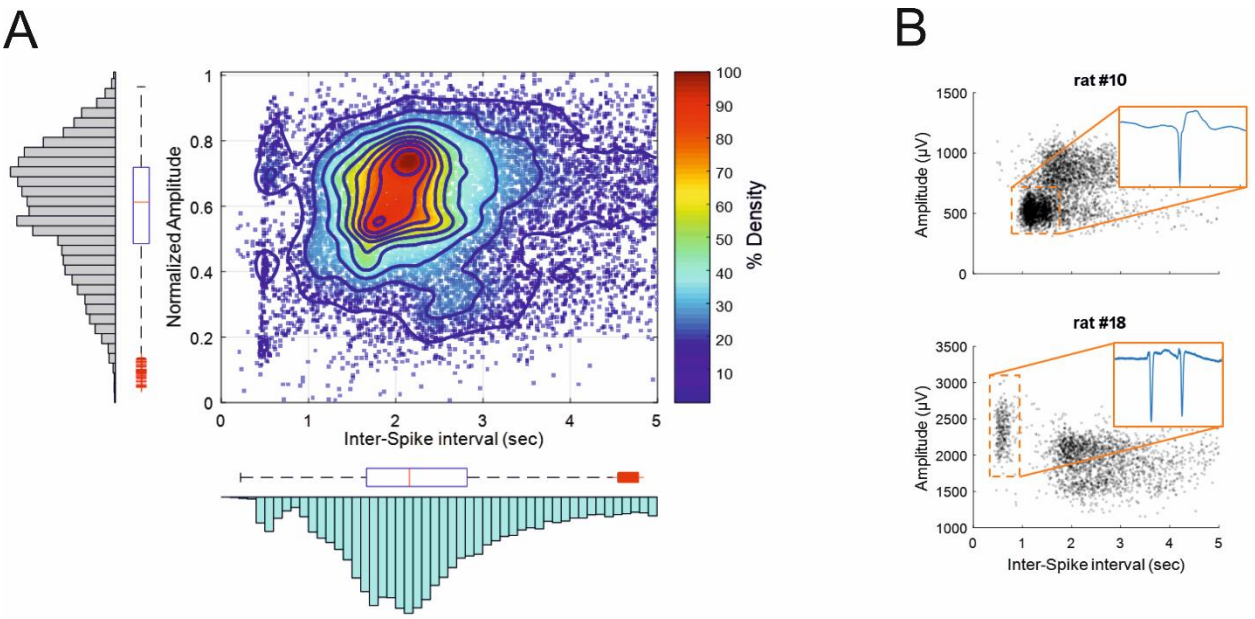

Figure 3. IISs are plotted depending on the time interval between each IIS (Interspike interval (ISI)), related to the normalized amplitude measured at the maximum amplitude of the peak. (A) The color plot shows the density (%) of 13,300 IISs at determined times and amplitudes in 19 rats. The histogram and boxplot statistics are placed next to the axis from which the data were extracted. Red "+" corresponds to outliers. (B) Representations of two rats with different IIS firing rates and voltages.

3.5.2. Ion-fluctuations surrounding the IISs

We evaluated the ion fluctuations surrounding the IIS (pre, during and after the spike) by extracting the characteristics of the LFP activities from 4,000 IISs (200 IISs per rat, for 20 rats) that fulfilled the condition of 1.5 s of isolation (to reduce the impact of closer IISs on the pre-spike period.

Ion sinks. Five rats showed an ion sink, restricted to the deeper channels, between -200 and -100 ms in the pre-spike period and starting before T0, visible in single IIS epochs after averaging. Three rats showed an ion sink between -100 and -50 ms in the deeper layers. All rats showed a

significant ion-sink between -50 and + 50 ms, corresponding to the time of MUA discharge (Figure 4 and 5), extending to deeper channels (n = 18) or restricted to superficial channels (n = 2). Finally, 13 rats showed a final ion sink in the deeper layers between 50 and 100 msec.

Ion sources. In 13 rats, we observed high source values in the middle and deepest layers (V and VI) between the two previous sinks at approximately 25 ms, corresponding to the peak of the MUA discharge (layers V-VI). Source values were measurable in deeper and superficial channels in the raw data and after averaging for all recordings (n = 20) in the period from 170 to 250 ms and were attributable to the slow-wave of the IIS.

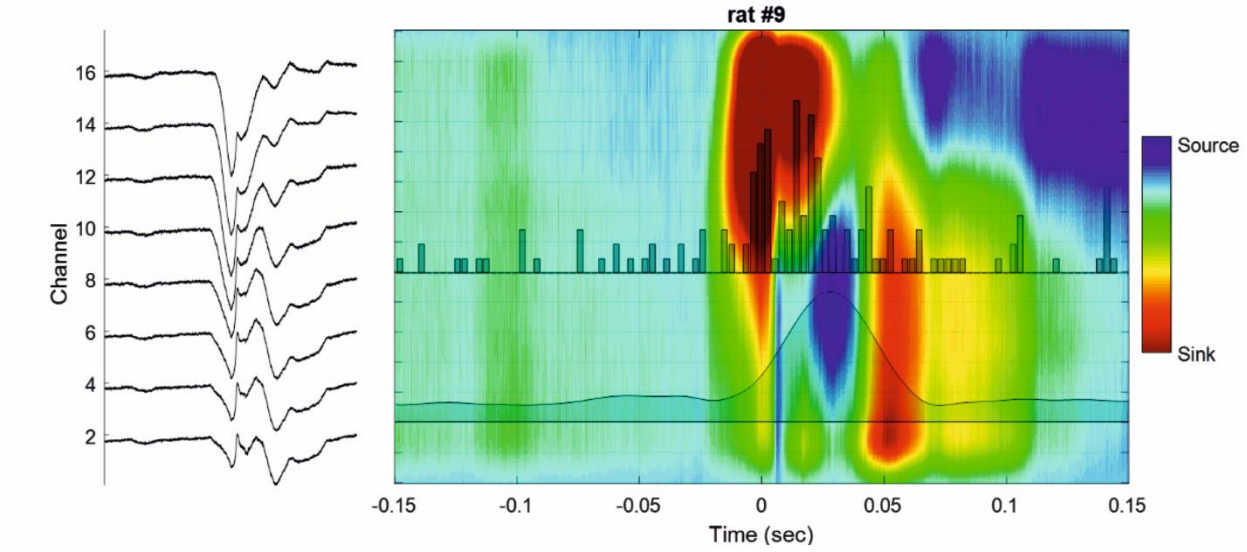

Figure 4. Cortical analysis of the current source density (CSD) during a single IIS. Left: LFP of a selected IIS at different recording depths. Right: Current source density analysis of the signal of the global unit activity (LFP shown on the left side) with superimposed unit activity histograms (Channel 16). The averaged multiunit activities (MUA) of all the channels are superimposed on the colormap.

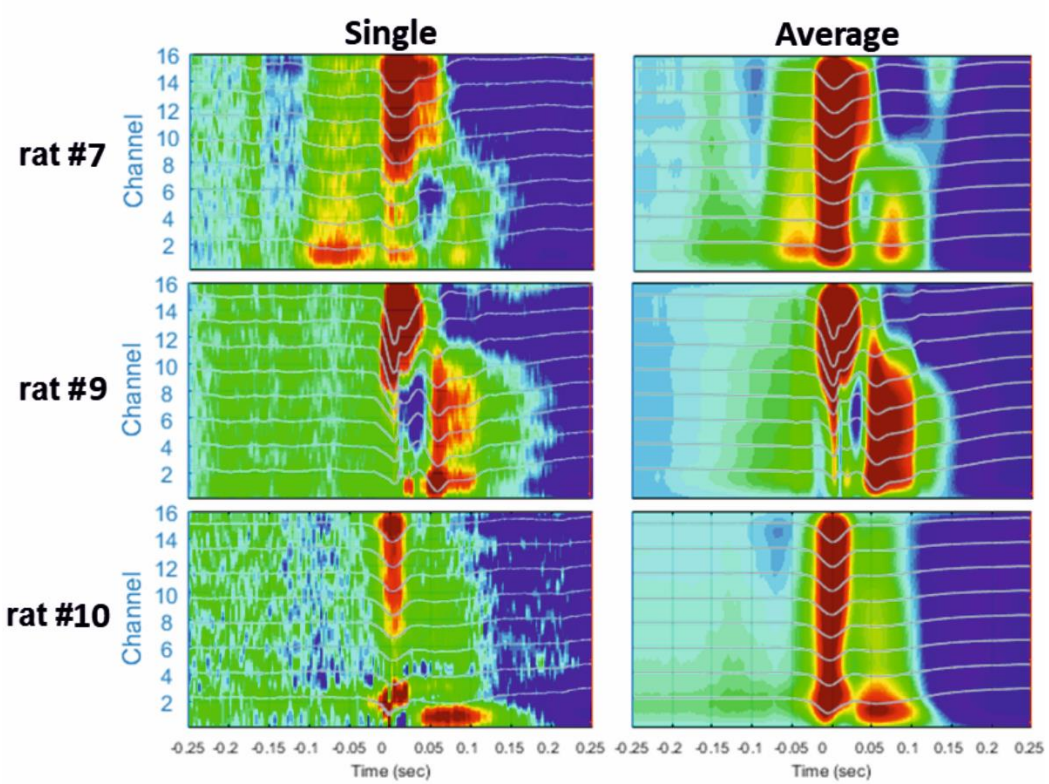

Figure 5. Examples of different CSD analyses of raw signals surrounding a single IIS (*left*) and after averaging 200 IISs (*right*). The LFP signals are superimposed on the color maps (T0 corresponds to the peak of IIS).

3.5.3. Differences in the LFP between superficial and deep layers during the pre-spike period

We evaluated whether there were any changes in the LFP occurring in the pre-spike period by anaylzing the temporal dynamics of the power of the LFP, with a particular focus on the difference in the RMS of the signals between the superficial and deep channels.

The grand average of the LFP activities of the superficial and deep channels were calculated from the peaks of the superficial channel (T0) and the standard deviations calculated for 26,641 IISs.

Analysis of the difference in the RMS between the averaged signals during the pre-spike period showed differences in the power of the signals from the superficial (Layers I and II) to deep layers (Layer VI). From -400 to -50 ms, the average RMS of the deeper channels was higher than that of the superficial channels (mean of 131.2%, $p < 0.01$) (Figure 6C). At -50 ms, the RMS of the superficial and deeper channels increased abruptly towards T0. At T0, the amplitude of the RMS reached higher values for the superficial than deeper channels (107%, $p < 0.01$) (Figure 6A and B). We observed only one peak for the superficial layer, whereas we observed a double peak (W

shape) for the deeper layer in 15 of 20 rats. The peak of the deeper layer ocurred a few milliseconds before that of the superficial layer. The W shape in the deeper layer was associated with a delay in the return to baseline, with the zero-power occurring earlier for the superficial layer (superficial: 75 ms, deeper: 111 ms). This period was followed by a slow wave in both layers, in which the peaks appeared to shift and the RMS power was significantly higher for the deeper than superficial layers (22 ms and 37.4%). The RMS returned to baseline at approximately 0.5 s. This was followed by a late significant component of small amplitude, which ended at approximately 1.5 s.

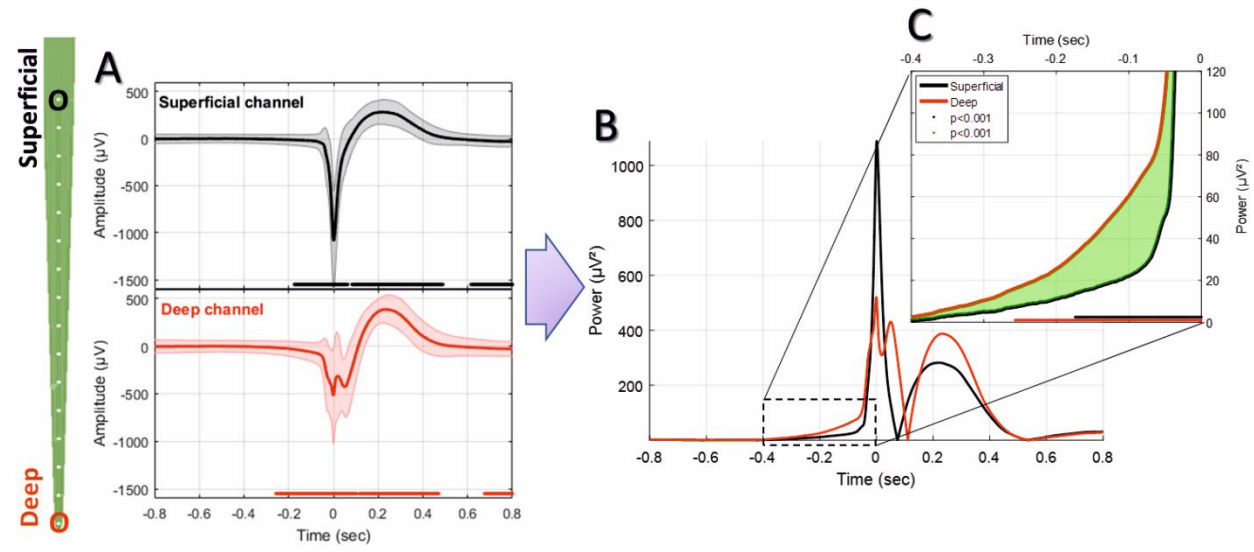

Figure 6. (*A*) Average LFP for superficial and deep channels recorded with the MLE probe with an ISI of 1.5 s (26,660 IISs). **(*B*)** Superposition of the average power of the superficial and deep channel signals. **(C)** Enlargement of the pre-spike period, highlighting the difference (in green) between the RMS signals of deep and superficial channels. The red and black solid lines indicate significant differences from the baseline for deep and superficial channels, respectively (-800 to -600 ms) ($p < 0.001$).

3.5.4. Time-frequency analysis of the LFP recorded at different depths along the multisite linear electrode (MLE)

We analyzed the TFR at the various electrode sites from the average of the LFP recordings acquired in 20 rats at each electrode site. The LFP signals at different depths showed a significant ($p < 0.02$) symmetric pattern around the IIS (ISI = 1.5 s), characterized by a decrease-increase-decrease of the spectral power. The first decrease in power started approximately 200 ms before the IIS peak (Figure 7A and B), followed by an increase in the power spectrum around the peak of the IIS (-100 to +100 ms), notably in the frequency range between 10 and 25 Hz. We also observed a non-significant boot shape between 100 and 400 ms in the low-frequency range (0-10 Hz) for both the deepest and superficial channels. Following the IIS, we observed heterogeneous decreases in power in various frequencies at up to 800 ms. Such sequences of decrease-increase-decrease in the power frequency occurred all along the electrode at different depths.

We minimized the average TFR of the deeper channel by that of the superficial channel to better analyze the difference between the deep and superficial layers (Figure 7C). During the pre-spike period, the decrease in the power frequency was similar for both the deep and superficial layers, with no significant differences when the deeper channels were minimized by the most superficial channel. During the spike period, there was a large difference around the IIS (-100 to + 100 ms) between the deep and superficial layers for the low frequencies (0-15 Hz), whereas there were robust differences in the post-spike period (200 to 800 ms) for frequencies > 25 Hz.

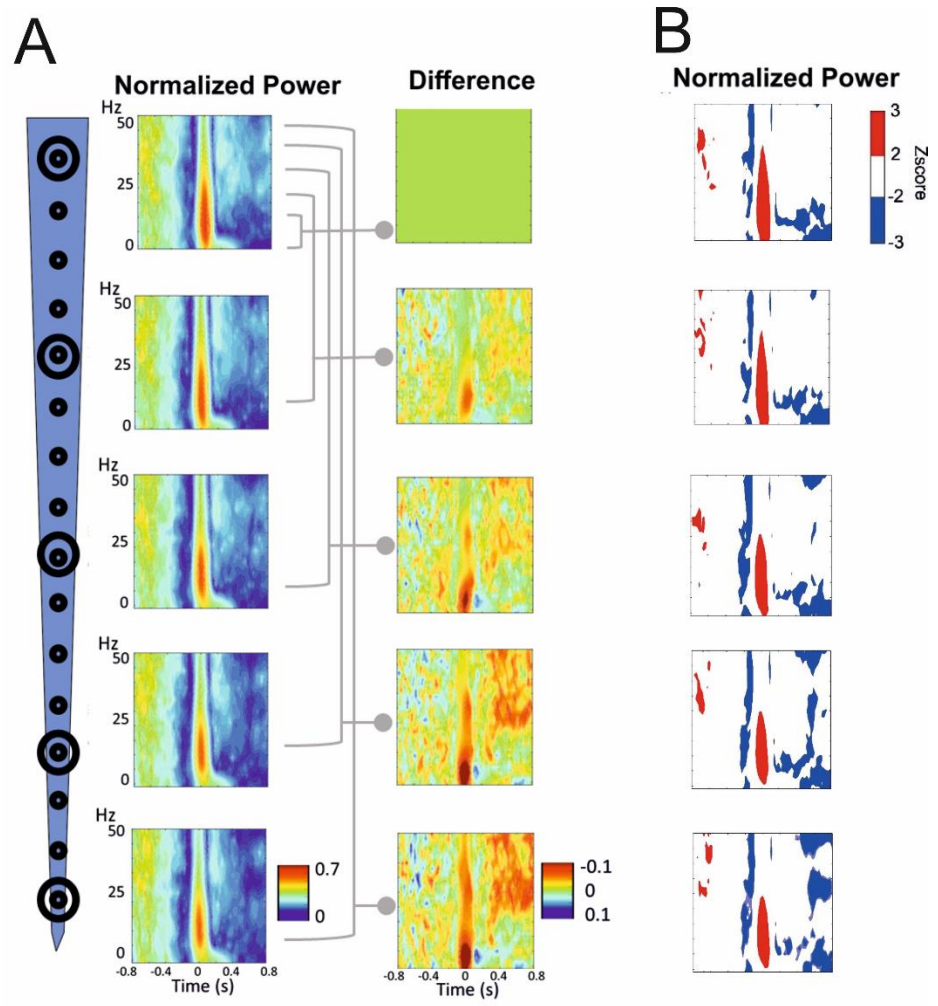

Figure 7. Time-frequency response (TFR) was performed around the peak of IIS (T0). ***(A)*** Normalized grand-average TFR power for different channels at different depths. The power differences between each of the four channels versus the most superficial channel are plotted on the right. ***(B)*** Z-score normalized results, highlighting the pattern of decrease-increase-decrease in the power frequency surrounding the IIS. An increase in synchrony is represented in red. A decrease in synchrony is plotted in blue.

3.5.5. Signal coherency along the MLE

We analyzed the dynamics of the coherency between the deep and superficial layers for the frequency. We selected the best combination of electrodes to extract the dynamics of the changes in signal coherency using the largest contrast between the deep and superficial electrodes among the 112 combinations per rat. Wavelet coherence analysis was first performed on a time window of 10 s. We observed similar significant ($p < 0.05$) patterns of low coherency values around the IIS in the rats (Figure 8 A and B), with a decrease in coherency, likely corresponding to a

decorrelation, surrounding the IIS in an “earring” (Figure 8A) or “tent” (Figure 8B) shape associated with the peak of the IIS.

We then individually averaged and normalized the coherency results for each rat (200 IISs (1.5 s ISI) per rat, for 18 rats) and calculated a grand-average based on each rat coherency (in total, 3,600 IISs were analyzed) (Figure 8C). The wavelet coherence analysis revealed a relatively symmetric pattern around the IIS, characterized by a decrease-increase-decrease in the coherency between the deep and superficial layers. More specifically, it showed an “earring” or “tent” shape, with a decrease in coherency starting at a low frequency (4Hz) at -1000 ms towards a decrease in coherency at a higher frequency (40 Hz) while approaching the peak of the IIS (near T0), which, after T0 (symmetrically up to T0) involved progressively lower frequencies (at 4 Hz) out to 1,000 ms. Comparison of the coherency values of the frequencies between 10 and 4 Hz to those of the baseline (-1.4 to -1.2 s of T0) showed significant changes ($p < 0.05$) in the pre-IIS period from -680 to -370 ms (Figure 8C). After T0, we observed significant changes between 0 and +800 ms.

There was a nested increase in coherencies at 12 to 20 Hz between the deep and superficial channels, with a maximum at around 100 ms. The decrease in coherency in the post-IIS period was more pronounced than that in the pre-IIS period.

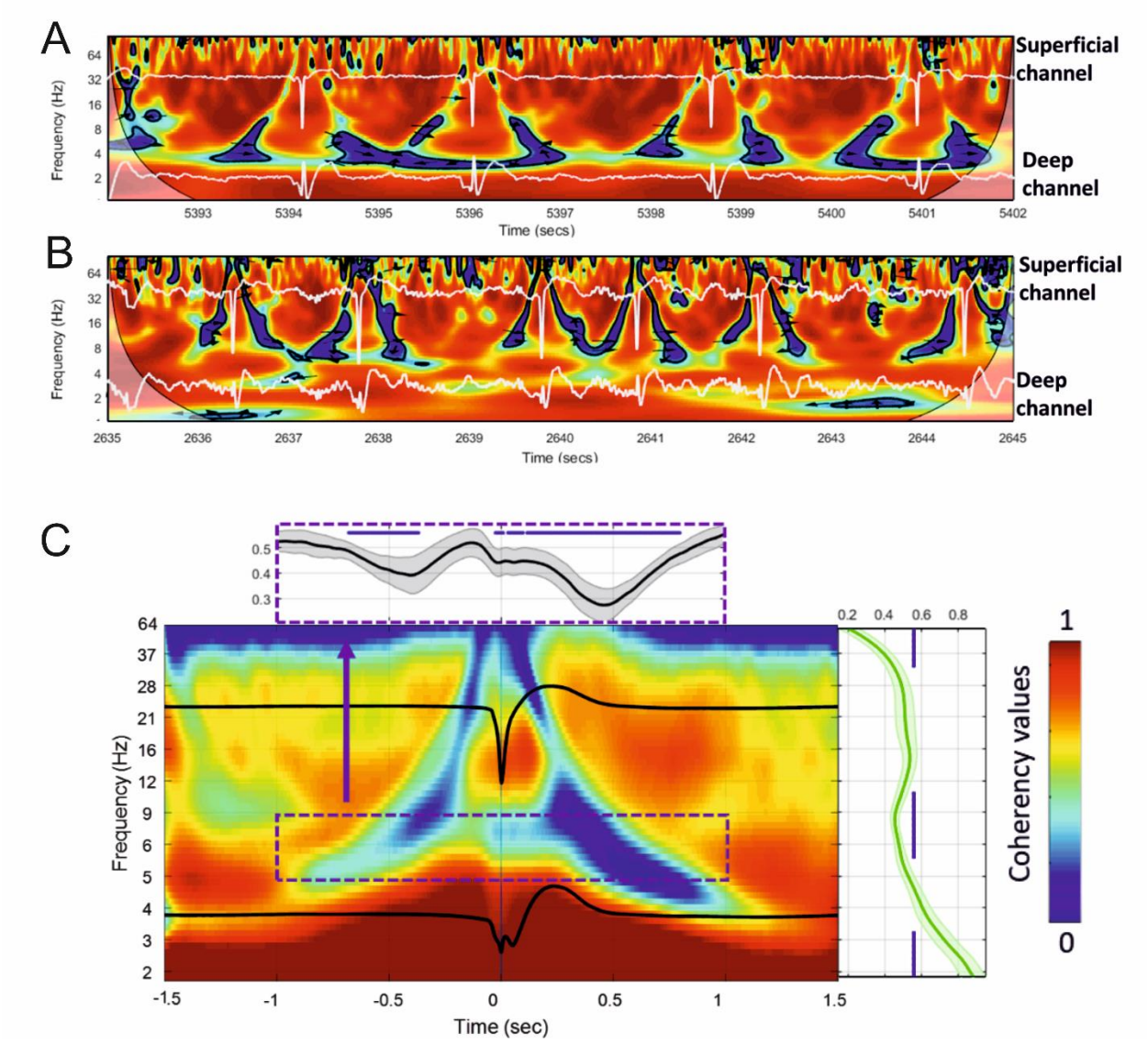

Figure 8. ***(A & B)*** Wavelet coherence analysis plot applied to the superficial and deeper channels of the MLE for a 10-s window for two rats. Red represents high coherency and blue low coherency between the superficial and deeper channels. Deep and superficial channels are over-plotted in white in each figure. The significant low coherency values, calculated by the Montecarlo method ($p < 0.05$), are shown inside each contour plot (in black). ***(C)*** Grand-average of 18 rats for 200 extracted wavelet windows aligned to T0 of 3,600 IISs. The subplots show the mean and standard deviation of the coherency values for all rats. Right: mean coherency values over the frequency axis. Top: mean coherency values over the time axis.

3.5.6. IIS vs. Unit activity

We recorded various types of firing activity for the motor cortex. We generally observed the best unit-activity signal for electrodes sampling layer VI. Each of the 19 rats selected for unit-activity firing analysis developed similar IISs on the ECoG (~3 units per rat, total 57). The IIS was

characterized by a biphasic wave, with a first peak of approximately 70 ms in duration, followed by a slow wave that peaked at approximately 200 ms, lasting 400 to 500 ms (Figure 9A). Based on the ECoG, we defined several periods around the IIS (Figure 9A) similar to those of previous studies (Saillet et al., 2016b): Period 1, the late pre-spike period (LPP), extending from the baseline (-700 ms) to -200 ms; Period 2, the early pre-spike period (EPP), extending from -200 to -35 ms; Period 3 (S1), the rising part of the spike (-35 ms to T0); Period 4 (S2), the falling edge of the spike (T0 to +35 ms); Period 5 (SW1), the rising part of the slow-wave (from 35 to 200 ms); Period 6 (SW2), the decaying part of the slow wave (from 200 ms to the end of the slow wave (between 400 and 600 ms; and Period 7 (R), the return to baseline that occurred after the slow wave recorded on the ECoG.

We classified different types of units based on this segmentation (Table 2). The most salient observations can be summarized as follows. For Period 1, we did not observe large differences in the discharge of unit-activity relative to baseline. Depending on the rat, the firing rate decreased (2 rats, 2 units) during this period relative to baseline, increased (2 rats, 3 units) (Figure 9B, cases 1 and 2), or did not change (15 rats, 52 units). During Period 2, some units (11 rats, 21 units) started to discharge 200 ms before the onset of the rapid rise of the spike, whereas the activity of others (2 rats 4 units) decreased (Figure 9B, cases 3 and 4). During Period 3, the increase of the firing rate was maximal for most of the units (16 rats, 54 units) (Figure 9B, case 5). During Period 4, some units reached their maximal discharge (Figure 9B, case 7), but for most, the firing rate started to decrease symmetrically to that of Period 3 (Figure 9B, case 6). In one case, the firing rate decreased relative to baseline during Periods 3 and 4. During Period 5, the firing rate was similar to baseline (17 rats, 40 units), significantly lower (6 rats, 11 units), or significantly higher (6 rats, 6 units) (Figure 9B, cases 9 and 8). During Period 6, the activity again increased relative to baseline (9 rats, 11 units) (Figure 9 B, case 10), decreased (3 rats, 4 units), or did not change (19 rats, 42 units).

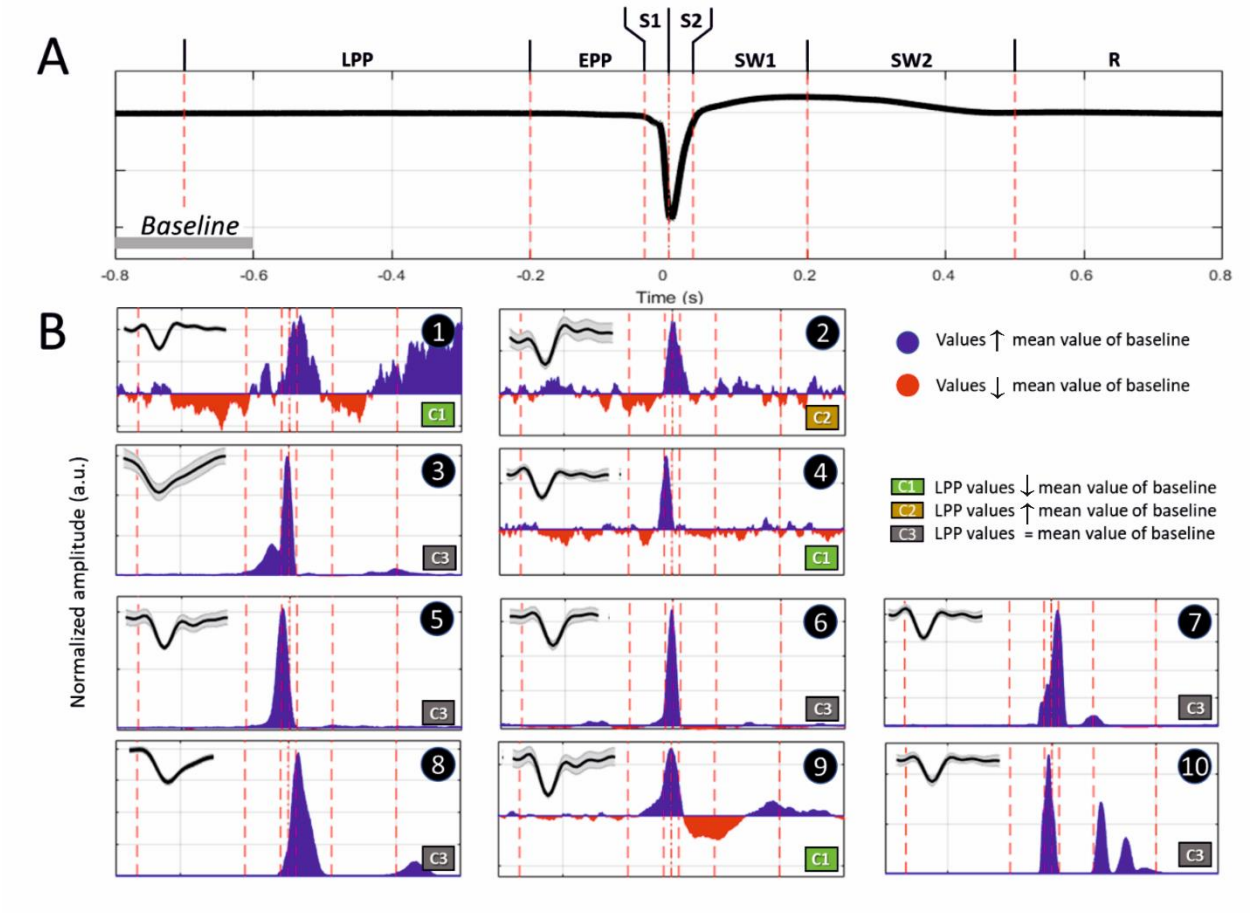

Figure 9. (A) Representation of an IIS, highlighting the reference periods (discontinuous vertical red lines at -700, -200, -35, 0, +35, +200, and +500 ms), with T0 corresponding to the peak of the IIS. (B) representative examples of differences in spike discharges occurring in the different periods (Inlet, shape of the unit activity with its standard deviation): Period 1 (LPP, -700 to -200 ms), B1 and B2; Period 2 (EPP, -200 to -35 ms), B3 and B4; Period 3 (S1, -35 to 0 ms), B5; Period 4 (S2, 0 to +35 ms), B7; Period 5 (SW1, +35 to +200 ms), B8 and B9; and Period 6 (SW2, +200 to +500 ms), B10. Period 7 (R, return to baseline). The blue and red areas represent values that are higher or lower than those of the mean of the baseline (-800 to -600 ms). The classification was performed according to the firing rate of Period 1. Class 1 (C1), increase; Class 2 (C2), decrease; and Class 3 (C3), no change.

In summary, focusing on the temporal dynamics of unit activity that were modulated during the pre-spike periods, unit-activity increased during the spike (Periods 3 and 4), regardless of the pattern of discharge during Periods 1 and 2. The discharge of unit activity during the post-spike periods was more complex and consisted of either an increase, decrease, or no change, with no specific relationship with the discharge patterns during the pre-spike periods.

Table 2. Classification of neuronal responses surrounding the interictal spikes.

UA firing pattern assigned number	UA firing with similar pattern	LPP (-700 to -200 ms)	EPP (-200 to -35 ms)	S1 (-35 to 0 ms)	S2 (0 to 35 ms)	SW1 (35 to 200 ms)	SW2 (200 to 400-600 ms)	R (Return to baseline)
1	12	-	-	↑	↑	-	-	-
2	10	-	↑	↑	↑	-	-	-
3	3	-	-	↑	↑	-	↑	-
4	2	-	↑	↑	-	-	-	-
5	2	-	-	↑	-	-	-	-
6	1	-	-	↑	↑	-	↑	↑
7	1	-	-	↑	↑	↓	↓	↑
8	1	-	↑	↑	↑	↓	-	↑
9	1	-	↓	↑	-	↓	-	↓
10	0	-	-	-	-	-	-	-
11	0	-	↑	↑	↑	↑	-	-
12	0	-	-	↑	↑	↑	-	-
13	0	-	-	-	↑	↑	-	↑
14	0	-	↑	↑	↑	↓	↑	↑
15	0	-	↓	↑	↑	-	-	-
16	0	-	-	↑	↑	↑	↑	↑
17	0	-	↑	↑	↑	↓	↑	-
18	0	-	-	↓	↓	-	-	↓
19	0	↑	↑	↑	↑	↓	-	↑
20	0	↑	-	↑	↑	↑	-	-
21	0	↑	-	↑	↑	-	↑	-
22	0	-	-	↑	↑	↓	↑	-
23	0	↓	↑	↑	↑	↑	↓	↑
24	0	↓	↓	↑	↑	↓	↓	↓

The symbols used to represent the firing rate of unit activity (UA) correspond to the change from baseline (-800 to -600 ms): increase (↑), decrease (↓), or no change (-) for the following periods classified depending on the time of IIS onset (set to T0): late pre-spike period (LPP), extending from the baseline (-700 ms) to -200 ms; the early pre-spike period (EPP), extending from -200 to -35 ms; the rising part of the spike (S1), from -35 ms to T0; the falling edge of the spike (S2), from T0 to +35 ms; the rising part of the slow-wave (SW1), from 35 ms to 200 ms; the decaying part of the slow-wave (SW2), from 200 ms to the end of the slow-wave (between 400 and 600 ms); and the return to baseline (R).

3.5.7. Hemodynamic responses for IISs: Changes in HbO_2, HbR, HbT, and CBF

We analyzed the hemodynamic activity of 18 rats (10 rats: ECoG + NIRS, 8 rats: MLE + NIRS), using a total of 17,995 IIS events (Figure 10). The pre- and post-IIS changes in oxy- and deoxyhemoglobin concentrations showed a similar pattern for all rats, in agreement with our previous results (Osharina et al., 2010, 2017).

Considering the baseline to be between 10 and 20 s before T0, changes in HbO2 (increase) and HbR (decrease) were recorded between -10 and -2 s (Figure 10A). Although the increase in CBF

was not significant, an increase in CBF variability was observed. From -2 s before T0, we recorded a significant and simultaneous decrease in HbO2 and CBF and a significant increase in HbR. The decreases in HbO2 and CBF peaked a few hundred milliseconds before T0, whereas the peak of HbR was reached a few hundred milliseconds after T0. This corresponds to a negative blood oxygenation level-dependent (BOLD) signal. Then, HbO2 and CBF simultaneously significantly increased, with a peak occurring at approximately 3 s after T0, whereas HbR significantly decreased, with a trough at 7 s after T0. This corresponds to a positive BOLD signal. Then, HbO2 and CBF simultaneously significantly decreased until 8 s after T0, whereas HbR once again increased, with a peak at 10 s. This corresponds to a second negative BOLD signal. Considering the baseline to be between 0 and -2 s (Figure 10B), the first negative BOLD signal was masked, but the rest of the pattern was superimposable over that described with the baseline between -10 and -20 s before T0, although the amplitudes of the peaks and troughs were less pronounced.

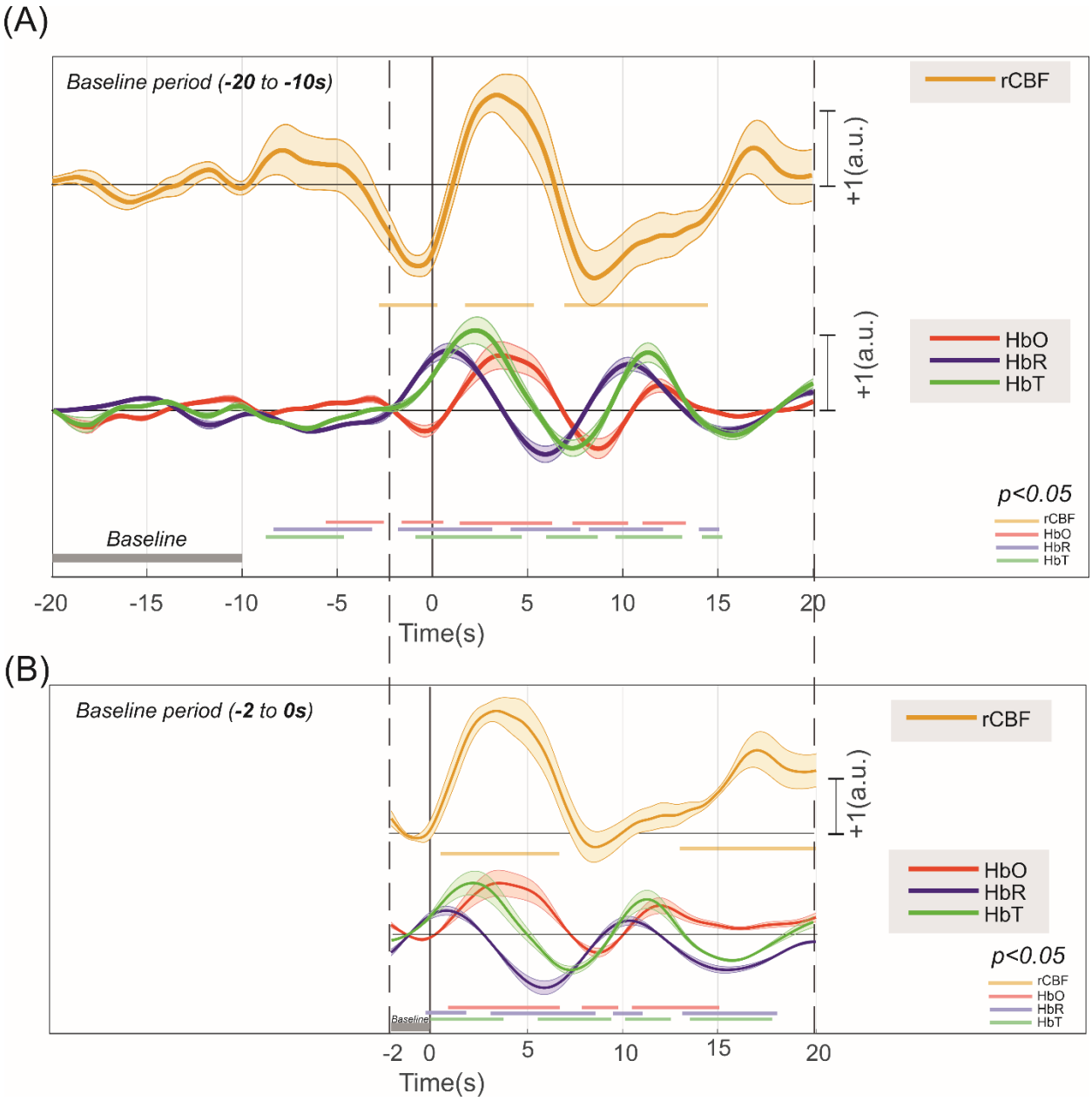

Figure 10. Deconvolution of the hemodynamic response of [HbR], [HbO_2], [HbT], and rCBF that occurs around an IIS (n = 17,995), with their significance ($p < 0.01$) drawn at the bottom in their respective colors. A: with the baseline at -20 to -10 s, B: with the baseline at -2 to 0 s.

3.5.8. Changes in the extracellular space at the onset of IISs

FOS results were broken down into several periods according to the fluctuations of the intensity of detected scattered photons that occurred around the IISs (n =7,908) (Figure 11). The period from -320 to -200 ms revealed a significant increase in detected light intensity ($p < 0.05$) from baseline (-800 to -600 ms) in six rats. Subsequently, the detected light intensity reached its peak

and then decreased until reaching the zero line at -100 ms. From -100 to T0, the intensity of the detected light continued to significantly drop. Then, a sharp increase in detected light intensity occurred from T0, crossing the zero line at 70 ms and reaching its maximum at 160 ms. Finally, the signal progressively decreased up to 360 ms.

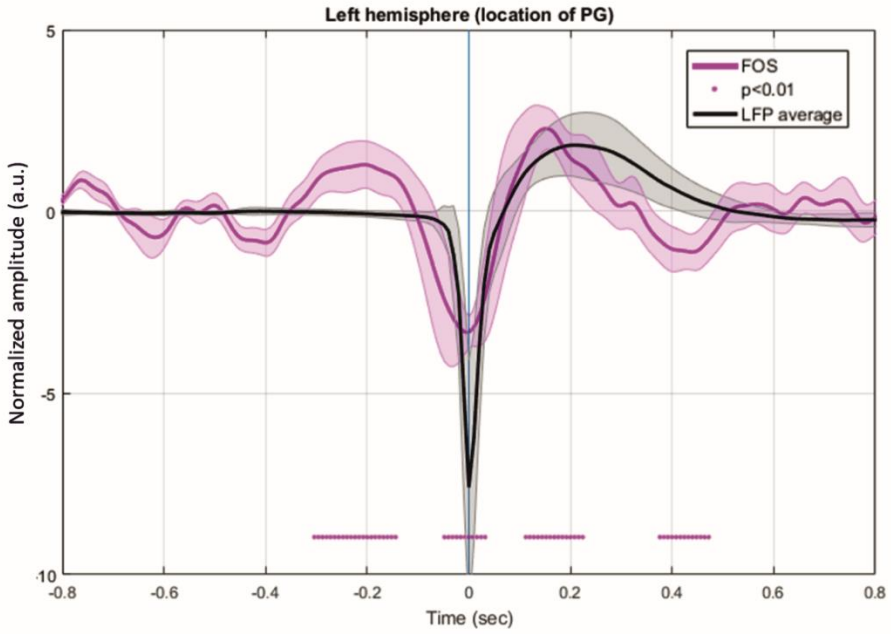

Figure 11. Grand-average of FOS for six rats. The red bar indicates the significant differences from baseline (-800 to -600 ms) ($p < 0.05$). Note the swing between increase-decrease-increase in light scattering during the simultaneously recorded LFP. Changes in light scattering preceded any changes in LFP by 400 ms.

3.6. Discussion

In the present study, we focused on simultaneous changes in neural and vascular activity and the membrane configuration of neural cells around the IIS, especially those preceding the IIS by a few hundred milliseconds. These changes were preceded and followed by complex alterations within the spike onset zone (injection zone) which corresponds to the region where epileptic spikes start and from where they propagate (Khoo et al., 2018). The mechanisms involved have not yet been fully elucidated. They cannot be explained solely by synaptic interactions, gap junctions, or ephaptic conduction involved in intrinsic membrane oscillations. The proposed mechanisms for the emergence of IISs only partially explain the observed alterations. A multimodal multiscale approach that combines ECoG, LFP, MUA, fNIRS, FOS, and DCS at a mesoscopic level allows multiscale analysis of the neuronal, (unitary and assembly of neurons and astrocytes),

hemodynamic, and non-synaptic mechanisms that contribute to the emergence of IISs. This approach provides further insight into the complex interactive mechanisms that propel the dynamics of the neuronal network to an IIS.

The first alteration in the measured signals that we observed was in the hemodynamic compartments (HbO2, HbR, CBF) a few seconds before the peak of the IIS. These hemodynamic changes were followed by changes in coherence and then synchronization between the deep and superficial neural networks in the 1 s preceding the IIS peaks. Finally, changes in light scattering that occurred before the epileptic spikes support a change in membrane configuration before the IIS.

The main results obtained for the different modalities, ordered from events that are the farthest to those are the closest to T0, are summarized in Figure 12.

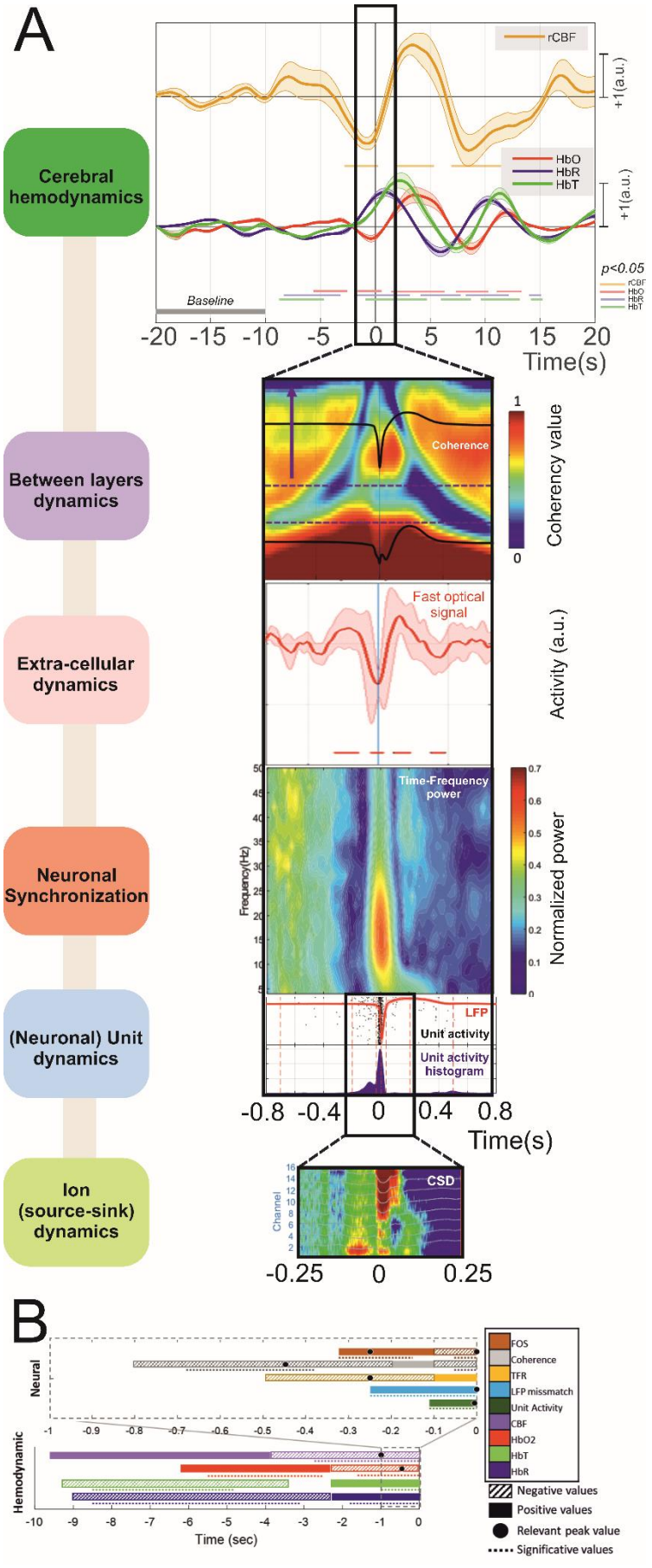
A
Cerebral hemodynamics
Between layers dynamics
Extra-cellular dynamics
Neuronal Synchronization
(Neuronal) Unit dynamics
Ion (source-sink) dynamics
rCBF
+1(a.u.)
HbO
HbR
HbT
+1(a.u.)
p<0.05
Baseline
-20 -15 -10 -5 0 5 10 15 20
Time(s)
Coherence
1
0
Coherency value
Fast optical signal
Activity (a.u.)
Time-Frequency power
Frequency(Hz)
0.7
0.6
0.5
0.4
0.3
0.2
0.1
0
Normalized power
LFP
Unit activity
Unit activity histogram
-0.8 -0.4 0 0.4 0.8
Time(s)
CSD
Channel
-0.25 0 0.25
B
Neural
Hemodynamic
-1 -0.9 -0.8 -0.7 -0.6 -0.5 -0.4 -0.3 -0.2 -0.1 0
-10 -9 -8 -7 -6 -5 -4 -3 -2 -1 0
Time (sec)
FOS
Coherence
TFR
LFP missmatch
Unit Activity
CBF
HbO2
HbT
HbR
Negative values
Positive values
Relevant peak value
Significative values

Figure 12. (A) The main results can be summarized as ***i) Cerebral hemodynamics:*** The hemoglobin concentration changes significantly from: -8.5 (↓[HbR] ↓[HbT]) and -5.5 s (↑[HbO_2]). Blood flow decreases significantly from -2.5 s (peak at -1 s). The hemoglobin concentration changes significantly from -2 s (↓[HbO_2] peak at -0.5 s, ↑[HbR] peak at +1 s) and -1 s (↑[HbT] peak at +2.5 s). ***ii) Between-layer dynamics:*** The spectral coherence decreases significantly between the superficial and deep layers from -680 to -370 ms for frequencies from 4 to 10 Hz (peak at -450 ms). ***iii) Extra-cellular dynamics:*** The scattered light intensity increases significantly from -320 to -150 ms (shrinking of neuronal cells). The scattered light intensity decreases significantly from -100 to +70 ms (swelling of neuronal cells). ***iv) Neuronal synchronization:*** Spectral synchronization is deregulated from -500 to -100 ms. ***v) (Neuronal) Unit dynamics:*** LFP signals change significantly from -260 ms for the deeper and -175 ms for the superficial layers. The neuronal firing rate increases significantly from -100 to +50 ms. ***vi) Ion (source-sink) dynamics:*** There are changes in the ion source/sink from -200 ms. **(B)** Summary of all the results based on the increasing or decreasing values of the hemodynamic and neural activities during the pre-IIS period. The colors and patterns of the bars are explained in the legend on the right. The bars represent the average values (positive or negative) and the dotted lines the significant periods for each analysis.

3.6.1. Hemodynamic data

Methodology

We tried to minimize the influence of closely-spaced IISs (i.e. overlapping of the hemodynamic response) by using the deconvolution method, which can efficiently estimate the hemodynamic response of a randomly-spaced event (Glover, 1999; Aarabi *et al.*, 2017). Although the general dynamics were similar, we observed slight differences in the pre-spike period in the hemodynamic responses to IISs using conventional averaging (Osharina *et al.*, 2010) or the deconvolution method (Osharina *et al.*, 2017). Deconvolution analysis is only minimally dependent on spike timing (Osharina *et al.*, 2010, 2017; Aarabi *et al.*, 2017). Inline, using fMRI, a pre-spike BOLD-positive response was reported in epileptic patients with IISs at a rate of 5 to 130/20 min, with a mean of 43.8/20 min, making it unlikely that the initial BOLD effect resulted from the previous IIS (Jacobs *et al.*, 2009).

We chose a baseline distant from the IIS (-20 to -10 s) rather than one next to it (-2 to -0 s) to evaluate changes in the dynamics of the various domains that occur before the IIS. A baseline close to the IIS makes an *a priori* assumption about the direction of neurovascular coupling. A baseline that covered all the data (Jacobs *et al.*, 2009) would have been a possible alternative but possible instability in systemic parameters (i.e. due to anesthetic drugs, etc.) during the duration of the recordings would have introduced uncontrolled variability to the baseline. However, analysis of the hemodynamic response using different baselines did not change the shape or timing of the

hemodynamic responses (HbO_2, HbR and CBF) but rather enhanced the measured changes that occurred before the IISs and the dynamics of the various slopes.

Hemodynamic changes during the pre-spike period

We identified complex changes in the hemodynamic parameters, which started to be significant approximately 8 s before the peak of the IIS (Phase I), in agreement with previous studies performed by fNIRS on rats (Osharina *et al.*, 2010, 2017) and humans (Bourel-Ponchel *et al.*, 2017). Our results are also consistent with those reported by fMRI and optical imaging studies of epileptic patients and animals showing that hemodynamic changes can occur during the pre-spike period (Gotman *et al.*, 2004; Mäkiranta *et al.*, 2005; Jacobs *et al.*, 2007, 2009; Moeller *et al.*, 2008; Grouiller *et al.*, 2009; Masterton *et al.*, 2010; Wallois *et al.*, 2010; Schwartz *et al.*, 2011; Pouliot *et al.*, 2012; Zhang *et al.*, 2014; Bourel-Ponchel *et al.*, 2017). This confirms that changes in hemodynamic activity start before the IIS, before any visible changes of electrocortical signals (Schwartz *et al.*, 2011). Hemodynamic responses to IIS have also been studied via intrinsic optical signals (Schwartz & Bonhoeffer, 2001; Suh *et al.*, 2005; Ma *et al.*, 2009) and laser Doppler flow (Vanzetta *et al.*, 2010). In these studies, the *a priori* assumption was made that the IIS itself would induce the hemodynamic response. Linear and non-linear modulations of the CBF dynamics were thus demonstrated from the IIS using laser Doppler flow (Vanzetta *et al.*, 2010).

Phase I: positive neurovascular coupling

With no *a priori* assumptions about the direction of the relationship between the neuronal and vascular system and using a baseline distant from the IIS, the very initial changes corresponded to low positive neurovascular coupling with (1) an increase in HbO_2, (2) a decrease in HbR, and (3) a slight increase in CBF, which was not significant but for which the variability increased. This is consistent with the positive BOLD signal described in a fMRI study (Jacobs *et al.*, 2007) and in our previous fNIRS studies (Osharina *et al.*, 2010, 2017). Although not considered to be significant by fNIRS, they were consistently observed in ipsi- and contra-lateral spikes and a different epileptic rat model (bicuculline vs penicillin G) (Osharina *et al.*, 2010, 2017). The increase in variability is intriguing, as it suggests either a decrease in the strength of control of CBF (i.e. changes in autoregulation of CBF) (Tewolde *et al.*, 2015; Saillet *et al.*, 2016*b*) or variability of the inputs into the CBF controller. Neither synaptic (ECoG, MUA, Coherence, Unit activity) nor non-synaptic (FOS) events were recorded during this very initial step.

Phase II: hypoxic stress for the surrounding neuronal network

From 5 s before the IIS, CBF decreased concomitantly with a decrease in HbO_2 and an increase in HbR, resulting in an increase in HbT, corresponding to an initial negative BOLD signal. Our results are concordant with the CBF response measured by laser Doppler flow experiments (Vanzetta *et al.*, 2010). When the baseline was close to zero, a small initial decrease in CBF was consistently observed before T0 (Vanzetta *et al.*, 2010). We observed a similar pattern of response with fNIRS and DCS, associated with a short initial decrease in CBF, using a similar baseline, between -2 and 0 s. Regardless of the baseline used, these results suggest the presence of hypoxic stress in the surrounding neuronal network that lasts for 4 s, ending 1 s before the IIS peak, which likely participates in the set of events (see below) that contribute to changes in the dynamics of the surrounding neuronal activity. This may correspond to the early decrease in hemoglobin oxygenation, called the 'epileptic dip', when using intrinsic optical signals (Suh *et al.*, 2005; Bahar *et al.*, 2006; Ma *et al.*, 2009). It should be noted that such a CBF and HbO_2 trough is concomitant to the onset of the changes in (1) spike discharge of certain neurons evaluated by LFP and MUA, (2) synchronization and coherencies between different cortical layers, and (3) neural membrane properties evaluated by FOS (see below).

Phase III: Positive BOLD signal (simultaneous increases in CBF and HbO_2)

Starting from the peak of the trough of HbO_2 and CBF (approximately -500 ms before the IIS peak), CBF increased concomitantly with the increase in HbO_2 and decrease in HbR. This corresponds to the classical positive BOLD signal in response to an IIS (Osharina *et al.*, 2017). In this classical model of neurovascular coupling in response to neuronal recruitment, such as during an IIS, a switch in the interaction between the neuronal and vascular systems occurs, during which the vascular dynamics (HbO_2 and CBF) become linearly and nonlinearly modulated by neuronal activity (Vanzetta *et al.*, 2010). Consistent with this model, simulated data (Voges *et al.*, 2012) support the idea that the characteristics of the CBF may also depend on the ISIs, as well as the duration of spike discharge (Geneslaw *et al.*, 2011) or its frequency (Saillet *et al.*, 2016*b*).

Concomitantly to the increase in CBF, a decrease in PO_2 has been reported, indicating that the increase in CBF may be temporarily unable to meet the high metabolic demands of the IIS when they occur at high frequency (0.5 Hz), as in the present study (Geneslaw *et al.*, 2011).

Phase IV: negative BOLD signal

The hemodynamic signals (HbO_2, HbR, and CBF) are modulated for 15 s. Such long-lasting modulation has not been described by laser Doppler flow, in which the data were smoothed with a 1.5-Hz Fourier filter (Vanzetta *et al.*, 2010) but corresponded to the simulated BOLD signal when various neural mass model spike shapes were simulated (Voges *et al.*, 2012).

Given the dynamics of the neurovascular coupling, with a peak of HbO_2 and CBF occurring 4 s after neuronal activation of the IIS, this negative BOLD signal, peaking at almost 8 s, likely reflects changes in the dynamics of the neuronal/astrocyte network. A second significant increase in HbO_2 and CBF above the baseline occurred at 12 s. According to Sotero and Trujillo-Baretto (Sotero & Trujillo-Barreto, 2007, 2008), there are two ways to induce a decrease in the BOLD signal: either the strong domination of inhibition or a decrease in excitation. The latter case would consist of the "deactivation" of the BOLD signal, resulting from decreasing neuronal activity (Buxton *et al.*, 2004). Alternatively, autonomous oscillation of the vasculature dynamics (elasticity), with a vascular undershoot, should not be completely ruled out, even if the shape of the HbO_2 and HbR curves (out of phase) argue for coupling with neuronal activity. Glial cells should also be considered; their membrane potential is known to be mainly affected by the extracellular potassium ion concentration. In penicillin-induced epileptic rats, they show strong transient depolarization concomitant with spikes in the EEG. These depolarizations reach their maximum value within 100 ms and repolarize over a period lasting between 1.5 and 7.0 s (Brueh *et al.*, 1995), meaning that astrocytes are depolarized concomitantly with the peak of CBF.

Such modulations of HbO_2 and CBF may explain certain apparently contradictory results (positive versus negative BOLD signals) when using a method with poor temporal resolution (on the order of 1 s), such as fMRI (Bénar *et al.*, 2006; Salek-Haddadi *et al.*, 2006; Gotman *et al.*, 2006).

The question arises as to what extent these cerebral hemodynamic modulations are sustained by synaptic and non-synaptic activities.

3.6.2. Electrophysiological data

The pre-spike period

No changes were observed by ECoG during phases I and II (until -1 s). However, we observed more-or-less concomitant neuronal and cellular changes during phase III, resulting from hypoxic

stress. The first dynamics to be modified were the changes in spectral coherence between the deep and superficial layers, which occurred symmetrically around the IIS (-1 to +1 s), simultaneously with the rising slope of CBF and HbO_2 levels.

We estimated the cross-correlation between oscillations in different cortical layers (deep vs. superficial layers) by applying time-frequency domain wavelet analysis. Wavelet-coherence analysis allows quantification of the similarity of the time-frequency (correlation) between the LFP and MUA activities of different channels (Ito *et al.*, 2014; Senzai *et al.*, 2019). Our results suggest changes in the interactions between different layers that start 1 s before the IIS, at the reversal of CBF from its trough. We observed a concomitant decrease or increase in unit discharge activity from -0.8 s before the IIS peak in some unitary recordings, suggesting that this decrease in correlation (decorrelation) may be associated with a change in the pattern of neuronal firing. This is somewhat earlier than what was described by Keller et al. (Keller *et al.*, 2010), who observed a decrease in the firing rate of some neurons (2 of 12) from -0.5 s in adult epileptic patients using intracerebral recordings. However, it is consistent with the presence of early changes in the MEG signal (up to 1 s before the peak of the IIS), implying that there are complex alterations in neuronal activity within a relatively large ensemble of neurons that occur well before the IIS (Zwiener *et al.*, 2000). Although we failed to observe any changes in the CSD during this period, differences in the RMS of the power of the LFP were observed between deep and superficial layers. This contributes to the body of evidence for early changes in interactions between superficial and deep layers of the cortex.

Neuronal activity changes start from the increase in CBF. We identified three classes of changes in unit activity (Class 1: increased unit activity, Class 2: decreased unit activity, Class 3: no modulation of unit activity). This is comparable to what has been previously described in epileptic patients (Keller *et al.*, 2010). Wavelet-coherence and RMS between the deep and superficial layers continue to be concomitantly modified, along with the change in coherence, moving to higher values. In agreement with a previous study (Keller *et al.*, 2010), at approximately -300 ms, changes in neuronal activity resulted in a decrease in TFR (7 of 20 rats), which did not show any differences between deep and superficial layers. In 4 of 20 rats, the CSD showed a tendency to dip 250 ms before the IIS peak in the deep layers of the cortex, showing that changes in ion flow started along certain neuronal cell extensions before the onset of the IIS. Altogether, this highlights the

complexity of the interactions within the epileptic network prior to an IIS. This occurs together with a change in the extracellular space, as characterized by the FOS.

Analyzing the FOS provides information on non-synaptic mechanisms involved in the emergence of the IIS. Changes in the optical properties of the neuronal tissue consisted of an increase in light detection, corresponding to a decrease in scattering, suggesting the shrinking of neurons or astrocytes, resulting in an increase in the extracellular space (Manoochehri *et al.*, 2017*b*) and thus a decrease in the bioavailability of various molecules. Such a change in light scattering before the IIS has been observed in both rats (Manoochehri *et al.*, 2017*b*) and epileptic patients with frontal lobe IISs (Manoochehri *et al.*, 2017*a*).

The spike period

As CBF increases together with HbO_2 levels, the firing rate of the neurons increase, although a decrease has not been observed (Keller *et al.*, 2010). In agreement with the previous study, the increase in the power spectra suggest an increase in activation and synchronization of local neuronal activity (Buzsáki *et al.*, 2012; Matsumoto *et al.*, 2013). Upon approaching T0, the decrease of coherency (i.e. decorrelation in the frequency domain) between the superficial and deep layers progressively shifted from lower to higher frequencies

Starting a few milliseconds before the IIS, analysis of the CSD showed constant spreading of sink activity from layers I -II to III (at the IIS onset), concomitant or not with a source in layers V and VI at the peak of the IIS, followed by a second source in layers V to VI (post-IIS), in complete accordance with the results of Castro-Alamancos (Castro-Alamancos, 2000) and Ulbert et al., (Ulbert *et al.*, 2004). This also highlights the complexity of the interactions between the layers (Barth *et al.*, 1989) and is consistent with the idea that different types of excitatory/inhibitory neurons/interneurons are solicited during the IIS (Barth *et al.*, 1989).

During the spike period, a decrease in light detection/increase in light scattering is consistent with the swelling of activated neuronal cells (neurons and or glial cells), resulting in a reduction of the extracellular space and thus an increase in the bioavailability of extracellular molecules that is specific to the site of injection (as this was not observed on the contralateral side) (Manoochehri *et al.*, 2017*b*).

The post-spike period

This period is concomitant with the peak of CBF and HbO_2. Based on ECoG, this period can be divided into two periods: Period 5-SW1, corresponding to the ascending part of the slow-wave [0-+300 ms], and Period 6-SW2, corresponding to the descending slope of the slow-wave, between +300- +500 ms. Concomitant with the ascending portion of the slow-wave (SW1), the neuronal activity either increased, decreased, or did not change relative to baseline, again suggesting complex interactions involving different types of neurons (excitatory or inhibitory) that participate in generating the slow-wave (Saillet *et al.*, 2016*b*). Initially, at the beginning of the slow wave, a sink in the superficial channels may support the participation of vertical inhibition of the deeper channels in some cases (Elger & Speckmann, 1983). During the peak of the slow wave, the TFR showed a global decrease (Manoochehri *et al.*, 2017*b*; Bourel-Ponchel *et al.*, 2017)), except at low frequencies, for which a boot shape was observed, in agreement with previous studies performed in epileptic patients (Bourel-Ponchel *et al.*, 2017). Simultaneously, the spatiotemporal pattern of the sink arising from layers IV to II–III gives the visual impression of continuous propagation, in perfect accordance with the results of Ulbert et al. (Ulbert *et al.*, 2004).

It is noteworthy that light detection increased around the peak of the slow-wave, suggesting a second round of shrinking of neurons and/or astrocytes concomitant with the slow-wave, as previously observed in rats and epileptic patients (Manoochehri *et al.*, 2017*b*, 2017*a*). Such shrinking of neurons may result in an increase of the extracellular space and a decrease in the bioavailability of molecules.

In Period 6-SW2, the firing rate of unit activity either increased, decreased, or did not change during the descending slope of the slow-wave, suggesting the participation of these neurons in the inhibitory process of the slow-wave (De Curtis & Avoli, 2016; Saillet *et al.*, 2016*b*). Simultaneously, the coherence between superficial and deeper channels once again decreased to lower frequencies and the light scattering returned to baseline. As the time increased from T0, the decrease of coherency (i.e. decorrelation in the frequency domain) between the superficial and deep layers progressively shifted from higher to lower frequencies.

3.6.3. Symmetric aspect

Changes in the neuronal and extracellular compartments appeared to be symmetric around the IIS, except for the hemodynamic changes. As previously observed by TFR (Keller *et al.*, 2010; Bourel-Ponchel *et al.*, 2017) or FOS (Manoochehri *et al.*, 2017*b*, 2017*a*; Wallois *et al.*, 2018), the

decorrelation between the superficial and deeper channels in the present study suggests an alternation of downstate-upstate-downstate. In summary, cellular shrinking-swelling-shrinking, or an increase-decrease-increase of the extracellular space, concomitant with a decrease-increase-decrease in the TFR at the same time that symmetric changes occur in the coherence between the superficial layers, is present around the IIS and during the increase in CBF and HbO_2 levels from their trough. Of course, the symmetry is not perfect because of the interactions between the various compartments, notably the impact of the characteristics of the IIS, the solicitation of different underlying types of neurons with different functionalities, and the changes in oxygen availability.

3.6.4. Causes and consequences

Synaptic and hemodynamic events

The first decrease in HbO_2 and CBF, also described in other studies (i.e. (Hawco *et al.*, 2007; Jacobs *et al.*, 2009; Vanzetta *et al.*, 2010), as well as the first increase in HbO_2 and CBF (the present study and (Osharina *et al.*, 2010, 2017)) have no counterparts in the synaptic and non-synaptic compartments.

We thus propose two hypotheses: (1) the neurogenic hypothesis: changes in the neuronal dynamics were not visible because they involved non-neuronal activity or that of astrocytes, which do not develop an electrical signature (Osharina *et al.*, 2010, 2017); (2) the hemo-neural hypothesis: hemodynamics may affect neural activity through direct and indirect mechanisms (i.e. the hemodynamics alter the gain of local cortical circuits) (Moore & Cao, 2008). Consistent with this hypothesis, Moore and Cao (Moore & Cao, 2008) suggested that functional hyperemia, the "overflow" of blood to a brain region during neural activity, provides a spatially and temporally correlated source of regulation, modulating the excitability of the local neuronal circuit (Moore & Cao, 2008).

Alternatively, slight changes in spontaneous vascular (and/or hemodynamic) oscillations in an atmosphere of interictal hypermetabolism in the epileptic focus, as observed in focal penicillin-induced epilepsy in rats (Witte *et al.*, 1994), may be the initial cause, with an initial relative hypoxic stress that triggers complex synaptic and non-synaptic events. This in turn may induce neurovascular coupling that might modulate the hemodynamic oscillations.

Non-synaptic events

Neuronal excitability can be altered by changes in the volume and ions of the extracellular space (Jefferys, 1995; Hochman, 2012). Aside from the non-synaptic events likely to occur in the early phase of the hemodynamic changes, including changes in autoregulation that occur in situations of hypermetabolism, the non-synaptic events occurring near the IIS were highlighted by changes in the optical properties. Non-synaptic events co-occurred with the increase in CBF and HbO_2, which may alter the oxygen partial pressures within the neuronal tissue and thus the dynamics of oxygen exchange. Such non-synaptic events occurred between -300 and +300 ms around the IIS, with a swing between shrinking-swelling-shrinking of the cellular compartments, including neurons and/or astrocytes. We previously have discussed the relationship between the changes in optical properties and structural changes in neural tissues (see (Manoochehri *et al.*, 2017*b*).

Briefly, neuronal activity is associated with the movement of ions across and around the membrane, resulting in the surface electrical response and changes in the osmolarity of the intracellular and extracellular compartments. This, in turn, may affect the scattering properties of the media. Neuronal activation and its correlative cell swelling have been shown to induce a decrease in scattering, resulting in a decrease in the FOS signal (Cohen, 1973; Rector *et al.*, 1997; TASAKI, 1999; Yao *et al.*, 2003; Akkin *et al.*, 2004; Lee & Kim, 2010). Conversely, an increase in light scattering or the FOS signal is considered to result from cell shrinking (Hill, 1950; Poe *et al.*, 1996). The initial increase in detected light intensity, likely corresponding to cell shrinking, was associated with areduction increase of the extracellular space that occurred together with (1) a decrease in neuronal synchronization, as evaluated by the TFR, (2) a decrease in coherencies between the superficial and deep layers at low frequencies, and (3) various changes (decrease, increase, no change) in unitary activity (the present study; (Keller *et al.*, 2010). Such a reduction of the extracellular space may result in a decrease in the bioavailability of extracellular glutamate and potassium (Dudek *et al.*, 1990). Such mechanisms would reinforce the effect of transient membrane hyperpolarization induced by the activation of local inhibitory interneurons, occurring prior to the rebound effect that immediately induces the hypersynchronization of the principal cells responsible for the IIS (Cobb *et al.*, 1995). The decrease in light intensity, likely corresponding to cell swelling, was associated with a decrease of the extracellular space that occurred during hypersynchronization. This reduction in the extracellular space likely enhances ephaptic conduction and electrolyte (notably K+) and neurotransmitter concentrations, which could modify local excitability and facilitate synchronization and the local formation of IISs (Somjen, 2004).

Concomitantly, the firing rate increased and the decorrelation between the various layers shifted to higher frequencies. Finally, the second increase in light intensity, corresponding to cell shrinking, was associated with an increase in the extracellular space. This would facilitate the disengagement of neurons from pathological synchronization and was related to a decrease in decorrelation between the cortical layers, a decrease in the spectral power, and the occurrence of the slow-wave of the LFP, while unit activity either decreased, increased, or did not change.

Limitations

Performing multimodal analysis requires the use of various imaging modalities that have different measuring scales and temporo-spatial resolution. This may introduce a bias in the analysis of the results when comparing the different modalities. Due to the complexity of performing simultaneous recordings, it is not always possible, notably for optical imaging, for which cross talk between different devices prevents simultaneous measurements. Performing multimodal monitoring is also challenging, because it can be difficult to maintain the stability of each recording over a long period, notably because of (1) the difficulty in maintaining a correct level of anaesthesia, (2) technical issues (noisy data), and (3) changes in IIS morphology during the recording. We paid particular attention to probe similar brain structures and placed the electrical and optical probes as close as possible to each other for the recordings of the various modalities, but it was impossible to place them in exactly the same position. Our main objective in this first study was to characterize complex interactions between the different neuronal and hemodynamic and extracellular compartments. Further study are required to investigate the specificity according to the different IIS patterns and to the type of epilepsy in different species. Despite the use of several multidimensional methods, which have still their own limitations, the biological process behind the interictal spikes were not completely monitored and require further studies, notably at the celular level.

3.7. Conclusion

This multimodal (ECoG-MLE-fNIRS-FOS-DCS) study also describes the neuronal, hemodynamic and membrane configuration changes observed in epileptic rats in response to endogenous hypersynchronization related to IIS. The intimate mechanisms supporting the concomitant changes during epileptic spikes deserve further in vitro analysis at the cellular level.

This multimodal approach highlights the complexity of spatio-temporal interactions between different cortical layers. It also shed new light on the specific hemodynamic and non-synaptic environment dynamics which initialize the neuronal changes that propels neurons to hypersynchronization of the interictal epileptic spike.

3.8. Competing interests

The authors have no competing interests to declare

3.9. Data availability statement

The data that support the findings of this study are available on request from the corresponding author. The data are not publicly available due to privacy or ethical restrictions.

3.10. Supplementary information

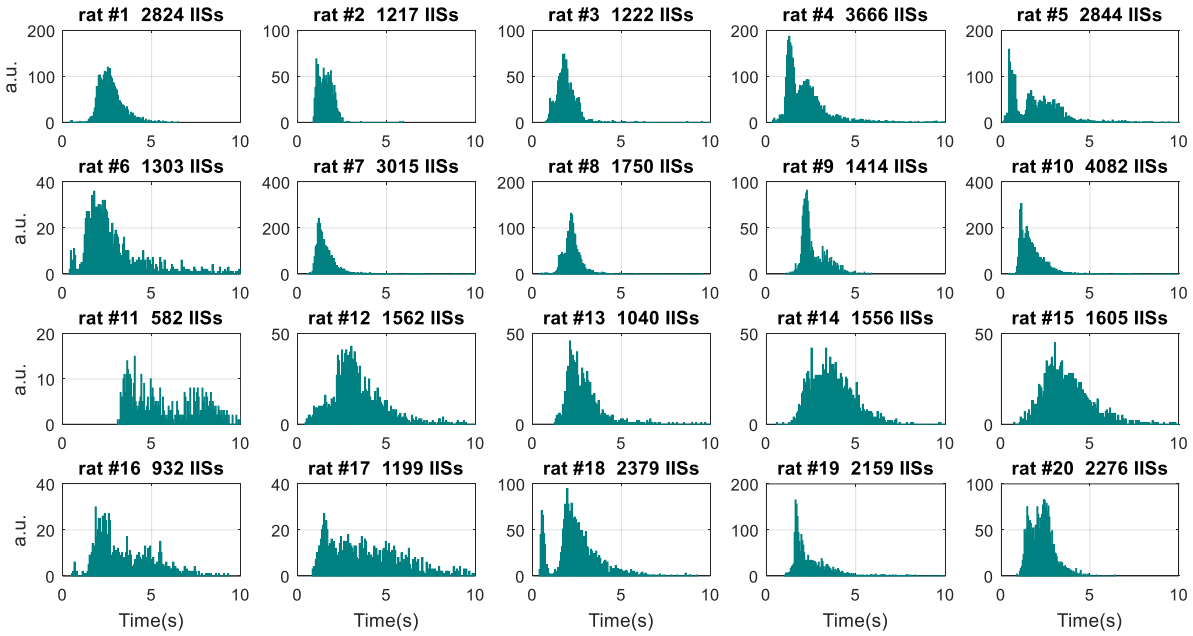

Figure S1. Inter-spike interval between the IISs of 20 rats. The rat code-name is shown at the top of each figure and the number of IISs used. The Y-axis represents the value of the counting bars and the X-axis the time between each pair of IISs.

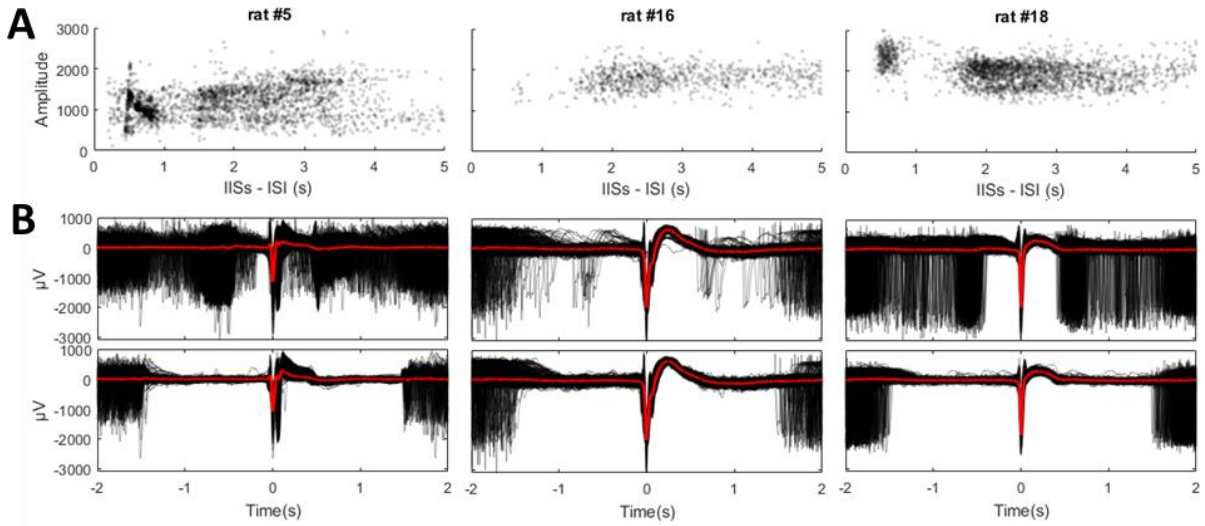

Figure S2. Representations of three rats for which there is an impact by an interspike interval below 1 s. (A) The scatter plots represent the amplitude compared to the interspike interval of the previous IIS. (B) Overplotts for which 0 is the time of the maximum amplitude of the IIS. At the *top*, overplots without any isolation time. At the *bottom*, the IIS signals overplotted after 1.5 sof isolation between their onset.

Table S1. Extended information for the interictal spikes for each rat.

Rat	Num of IIS	Duration recordings in seconds	Minimal distance ISI	Maximal distance ISI	IIS per second	Average ISI	Num events ISI >1.5sec	IIS per minute	Std IIS per minute	Mean onset µVolt	Std onset µVolt	CV of firing in %
#1	2824	7720	0.48	6.54	0.37	2.73	2788	21.95	2.87	1026.24	211.20	13.07
#2	1217	1948	0.93	5.97	0.62	1.60	360	37.47	2.22	1245.21	269.39	5.93
#3	1222	2417	0.80	18.34	0.51	1.98	779	30.33	5.97	623.00	132.24	19.68
#4	3666	8373	0.41	43.51	0.44	2.28	1758	26.27	7.54	400.68	96.76	28.69
#5	2844	5670	0.20	11.42	0.50	1.99	778	30.09	8.37	1090.02	351.03	27.81
#6	1303	6387	0.42	189.16	0.20	4.91	997	12.24	10.31	729.87	340.19	84.21
#7	3015	5342	0.64	76.68	0.56	1.77	849	33.86	12.03	716.25	276.61	35.54
#8	1750	3952	0.50	9.57	0.44	2.26	1643	26.57	1.96	520.05	137.34	7.39
#9	1414	3772	1.19	5.91	0.37	2.67	1402	22.49	3.49	1585.27	330.62	15.51
#10	4082	7269	0.49	11.09	0.56	1.78	1739	33.69	8.55	798.88	175.16	25.37
#11	582	3648	3.11	25.61	0.16	6.28	581	9.57	3.33	1442.03	187.92	34.80
#12	1562	5307	0.45	18.37	0.29	3.40	1343	17.66	4.54	712.65	273.08	25.72
#13	1040	3105	1.30	25.30	0.33	2.99	1006	20.10	4.44	571.57	97.14	22.08
#14	1556	5760	0.64	22.59	0.27	3.70	1543	16.21	2.14	629.22	186.65	13.19
#15	1605	6270	0.76	27.90	0.26	3.91	1567	15.36	3.31	1690.11	418.32	21.58
#16	932	3243	0.60	9.35	0.29	3.48	889	17.24	2.31	1854.30	264.93	13.39
#17	1199	5098	0.88	39.86	0.24	4.26	965	14.11	3.71	1656.72	296.63	26.30
#18	2379	6007	0.41	9.30	0.40	2.53	1816	23.76	3.67	1865.44	267.85	15.45
#19	2159	5417	1.09	10.20	0.40	2.51	2005	23.91	7.24	1031.82	225.80	30.27
#20	2276	5280	0.90	6.44	0.43	2.32	1833	25.86	3.87	1130.91	177.10	14.95
TOTAL	38627	101985	-	-	-	-	26641	-	-	-	-	-
Average	1931.35	5099.25	0.81	28.66	0.38	2.97	1332.05	22.94	5.09	1066.01	235.80	24.05
STD	947.36	1730.17	0.62	41.52	0.13	1.19	585.39	7.71	2.94	473.14	88.18	16.49

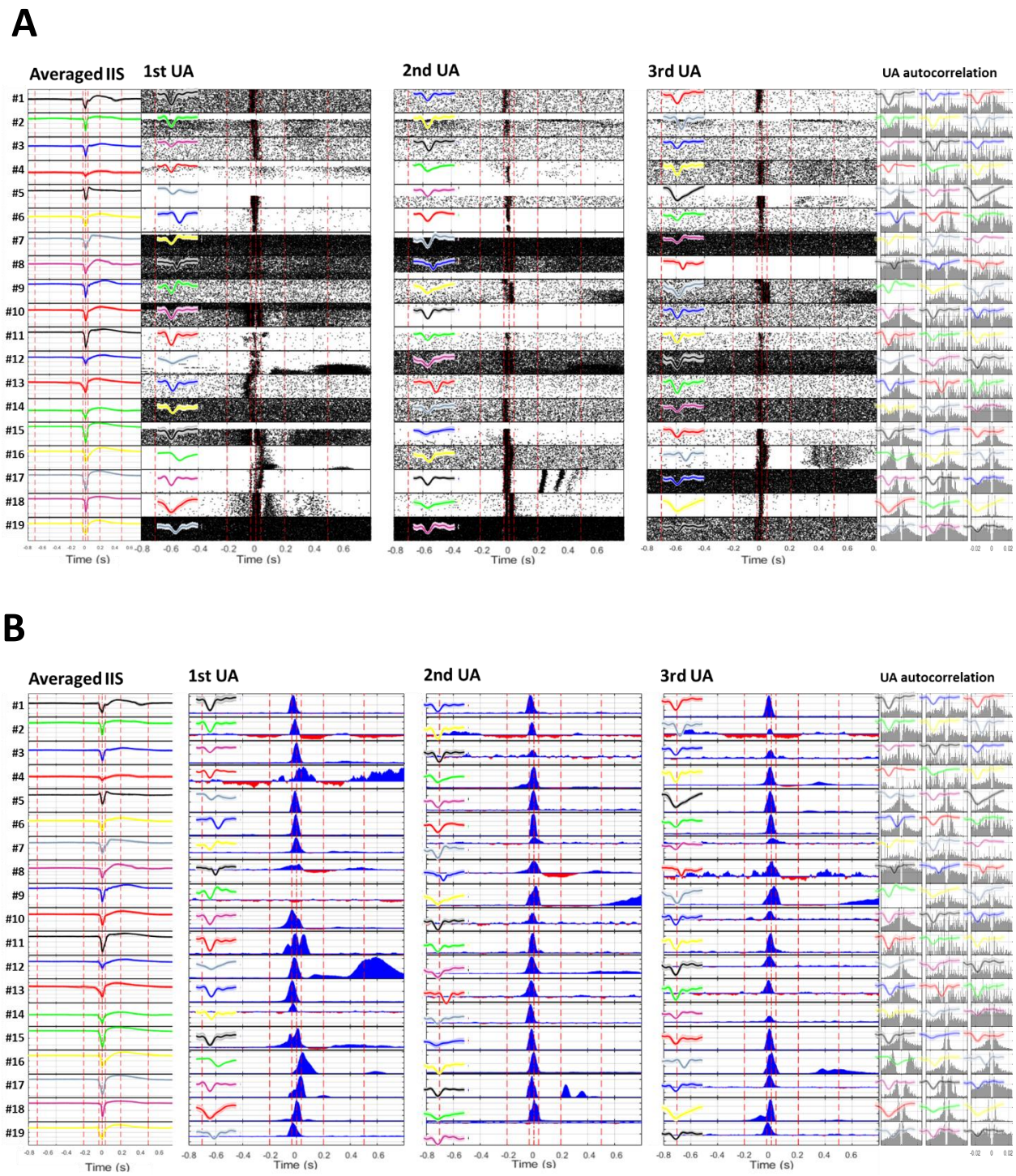

Figure S3. Overview of the unit activity analysis. Three unit activities (UA, plotted in color) were selected for each selected rat (code-name at *left* of **A** and **B**) and aligned to time-0 (maximum peak amplitude of the IIS). The representation for each UA firing was plotted in a raster (***A*** *middle*) or in a counting plot (***B*** *middle*). The autocorrelation for each UA is shown on the *right* (**A** and **B**). The blue and red areas represent values above and below those of the baseline, respectively (-800 to -600 msec).

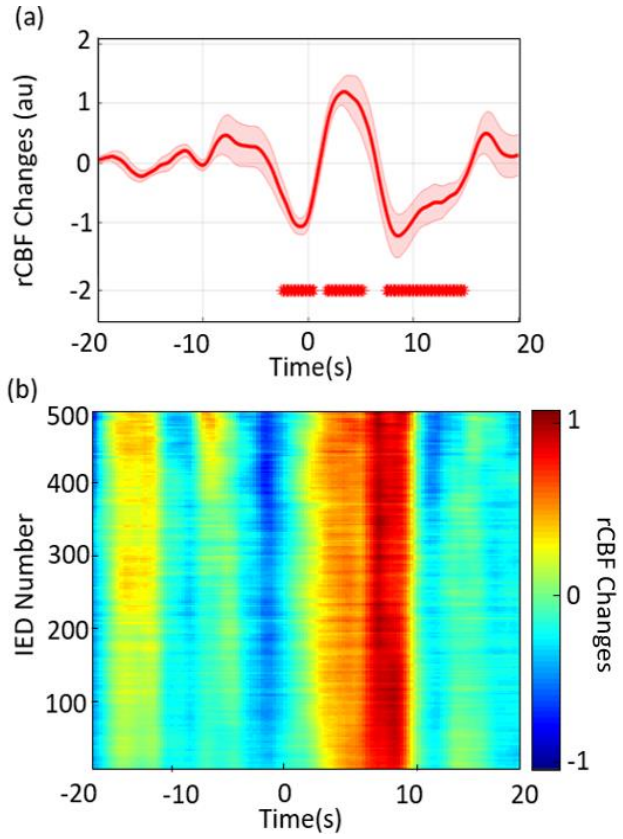

Figure S4. (a) Deconvoluted rCBF responses with the corresponding standard deviations (shaded error bars). The annotations (red stars) below the signal, showing the duration of the rCBF responses, were significantly different from those of the reference period (−20 to −10 s before the IIS peak, $p < 0.001$). **(b)** Time-course of rCBF changes for one rat using the dynamic FIR method.

3.11. References

Aarabi A, Osharina V & Wallois F (2017). Effect of confounding variables on hemodynamic response function estimation using averaging and deconvolution analysis: An event-related NIRS study. *NeuroImage* **155,** 25–49.

Akdogan I, Adiguzel E, Yilmaz I, Ozdemir MB, Sahiner M & Tufan AC (2008). Penicillin-induced epilepsy model in rats: Dose-dependant effect on hippocampal volume and neuron number. *Brain Research Bulletin* **77,** 172–177.

Akkin T, Davé DP, Milner TE & Rylander III HG (2004). Detection of neural activity using phase-sensitive optical low-coherence reflectometry. *Optics Express* **12,** 2377.

Andrew RD & Macvicar BA (1994). Imaging cell volume changes and neuronal excitation in the hippocampal slice. *Neuroscience* **62,** 371–383.

Anon (2019). WHO | Epilepsy: a public health imperative. *WHO*.

Bahar S, Suh M, Zhao M & Schwartz TH (2006). Intrinsic optical signal imaging of neocortical seizures: the ???epileptic dip??? *NeuroReport* **17,** 499–503.

Banerjee PN, Filippi D & Allen Hauser W (2009). The descriptive epidemiology of epilepsy-A review. *Epilepsy Research* **85,** 31–45.

Barth DS, Di S & Baumgartner C (1989). Laminar cortical interactions during epileptic spikes studied with principal component analysis and physiological modeling. *Brain Research* **484,** 13–35.

Bénar CG, Grova C, Kobayashi E, Bagshaw AP, Aghakhani Y, Dubeau F & Gotman J (2006). EEG-fMRI of epileptic spikes: Concordance with EEG source localization and intracranial EEG. *NeuroImage* **30,** 1161–1170.

Bourel-Ponchel E, Mahmoudzadeh M, Delignières A, Berquin P & Wallois F (2017). Non-invasive, multimodal analysis of cortical activity, blood volume and neurovascular coupling in infantile spasms using EEG-fNIRS monitoring. *NeuroImage: Clinical* **15,** 359–366.

Brueh C, Kloiber O, Hossman KA, Dorn T & Witte OW (1995). Regional Hypometabolism in an Acute Model of Focal Epileptic Activity in the Rat. *European Journal of Neuroscience* **7,** 192–197.

Buxton RB, Uludağ K, Dubowitz DJ & Liu TT (2004). Modeling the hemodynamic response to brain activation. In *NeuroImage*, pp. S220–S233. Academic Press.

Buzsáki G, Anastassiou CA & Koch C (2012). The origin of extracellular fields and currents-EEG, ECoG, LFP and spikes. *Nature Reviews Neuroscience* **13,** 407–420.

Castro-Alamancos MA (2000). Origin of synchronized oscillations induced by neocortical disinhibition in vivo. *Journal of Neuroscience* **20,** 9195–9206.

Castro-alamancos MA, Rigas P & Tawara-hirata Y (2007). Resonance (~10 Hz) of excitatory networks in motor cortex: Effects of voltage-dependent ion channel blockers. *Journal of Physiology* **578,** 173–191.

Cobb SR, Buhl EH, Halasy K, Paulsen O & Somogyi P (1995). Synchronization of neuronal activity in hippocampus by individual GABAergic interneurons. *Nature* **378,** 75–78.

Cohen LB (1973). *Changes in Neuron Structure During Action Potential Propagation and Synaptic Transmission*.

De Curtis M & Avanzini G (2001). Interictal spikes in focal epileptogenesis. *Progress in Neurobiology* **63,** 541–567.

De Curtis M & Avoli M (2016). GABAergic networks jump-start focal seizures. *Epilepsia* **57,** 679–687.

De Curtis M, Manfridi A & Biella G (1998). *Activity-Dependent pH Shifts and Periodic Recurrence of Spontaneous Interictal Spikes in a Model of Focal Epileptogenesis*.

Dudek FE, Obenaus A & Tasker JG (1990). Osmolality-induced changes in extracellular volume alter epileptiform bursts independent of chemical synapses in the rat: Importance of non-synaptic mechanisms in hippocampal epileptogenesis. *Neuroscience Letters* **120,** 267–270.

Durduran T, Choe R, Baker WB & Yodh AG (2010*a*). Diffuse optics for tissue monitoring and tomography. *Reports on Progress in Physics*; DOI: 10.1088/0034-4885/73/7/076701.

Durduran T, Zhou C, Buckley EM, Kim MN, Yu G, Choe R, Gaynor JW, Spray TL, Durning SM, Mason SE, Montenegro LM, Nicolson SC, Zimmerman RA, Putt ME, Wang J, Greenberg JH, Detre JA, Yodh AG & Licht DJ (2010*b*). Optical measurement of cerebral hemodynamics and oxygen metabolism in neonates with congenital heart defects. *Journal of Biomedical Optics* **15,** 037004.

Elger CE & Speckmann EJ (1983). Penicillin-induced epileptic foci in the motor cortex: Vertical inhibition. *Electroencephalography and Clinical Neurophysiology* **56,** 604–622.

Feigin VL et al. (2019). Global, regional, and national burden of neurological disorders, 1990–2016: a systematic analysis for the Global Burden of Disease Study 2016. *The Lancet Neurology* **18,** 459–480.

Geneslaw AS, Zhao M, Ma H & Schwartz TH (2011). Tissue hypoxia correlates with intensity of interictal spikes. *Journal of cerebral blood flow and metabolism : official journal of the International Society of Cerebral Blood Flow and Metabolism* **31,** 1394–1402.

Glover GH (1999). *Deconvolution of Impulse Response in Event-Related BOLD fMRI 1*.

Gotman J, Bénar C-G & Dubeau F (2004). Combining EEG and fMRI in Epilepsy: Methodological Challenges and Clinical Results. *Journal of Clinical Neurophysiology* **21,** 229–240.

Gotman J, Kobayashi E, Bagshaw AP, Bénar C-G & Dubeau F (2006). Combining EEG and fMRI: A multimodal tool for epilepsy research. *Journal of Magnetic Resonance Imaging* **23,** 906–920.

Gotman J & Pittau F (2011). Combining EEG and fMRI in the study of epileptic discharges. *Epilepsia* **52,** 38–42.

Gratton G & Fabiani M (1998). Dynamic brain imaging: Event-related optical signal (EROS) measures of the time course and localization of cognitive-related activity. *Psychonomic Bulletin and Review* **5,** 535–563.

Grouiller F, Vercueil L, Krainik A, Segebarth C, Kahane P & David O (2009). Characterization of the hemodynamic modes associated with interictal epileptic activity using a deformable model-based analysis of combined EEG and functional MRI recordings. *Human Brain Mapping* **31,** NA-NA.

Hawco CS, Bagshaw AP, Lu Y, Dubeau F & Gotman J (2007). BOLD changes occur prior to epileptic spikes seen on scalp EEG. *NeuroImage* **35,** 1450–1458.

Hill DK (1950). The volume change resulting from stimulation of a giant nerve fibre. *The Journal of Physiology* **111,** 304–327.

Hochman DW (2012). The extracellular space and epileptic activity in the adult brain: Explaining the antiepileptic effects of furosemide and bumetanide. *Epilepsia* **53,** 18–25.

Hoechstetter K, Bornfleth H, Weckesser D, Ille N, Berg P & Scherg M (2004). BESA source coherence: A new method to study cortical oscillatory coupling. *Brain Topography* **16,** 233–238.

Holmes O, Wallace MN & Campbell AM (1987). COMPARISON OF PENICILLIN EPILEPTOGENESIS IN RAT SOMATOSENSORY AND MOTOR CORTEX. *Quarterly Journal of Experimental Physiology* **72,** 439–452.

Hotka M & Kubista H (2019). The paroxysmal depolarization shift in epilepsy research. *International Journal of Biochemistry and Cell Biology* **107,** 77–81.

Ito S, Yeh FC, Hiolski E, Rydygier P, Gunning DE, Hottowy P, Timme N, Litke AM & Beggs JM (2014). Large-scale, high-resolution multielectrode-array recording depicts functional network differences of cortical and hippocampal cultures. *PLoS ONE* **9,** 105324.

Jacobs J, Kobayashi E, Boor R, Muhle H, Stephan W, Hawco C, Dubeau F, Jansen O, Stephani U, Gotman J & Siniatchkin M (2007). Hemodynamic responses to interictal epileptiform discharges in children with symptomatic epilepsy. *Epilepsia* **48,** 2068–2078.

Jacobs J, LeVan P, Moeller F, Boor R, Stephani U, Gotman J & Siniatchkin M (2009). Hemodynamic changes preceding the interictal EEG spike in patients with focal epilepsy investigated using simultaneous EEG-fMRI. *NeuroImage* **45,** 1220–1231.

Jefferys JGR (1995). Nonsynaptic modulation of neuronal activity in the brain: Electric currents and extracellular ions. *Physiological Reviews* **75,** 689–723.

Jensen MS, Azouz R & Yaari Y (1994). Variant firing patterns in rat hippocampal pyramidal cells modulated by extracellular potassium. *Journal of Neurophysiology* **71,** 831–839.

Jensen MS, Azouz R & Yaari Y (1996). Spike after-depolarization and burst generation in adult rat hippocampal CA1 pyramidal cells. *The Journal of Physiology* **492,** 199–210.

Keller CJ, Truccolo W, Gale JT, Eskandar E, Thesen T, Carlson C, Devinsky O, Kuzniecky R, Doyle WK, Madsen JR, Schomer DL, Mehta AD, Brown EN, Hochberg LR, Ulbert I, Halgren E & Cash SS (2010). Heterogeneous neuronal firing patterns during interictal epileptiform discharges in the human cortex. *Brain* **133,** 1668–1681.

Lee J & Kim SJ (2010). Spectrum measurement of fast optical signal of neural activity in brain tissue and its theoretical origin. *NeuroImage* **51,** 713–722.

Ma H, Zhao M, Suh M & Schwartz TH (2009). Hemodynamic surrogates for excitatory membrane potential change during interictal epileptiform events in rat neocortex. *Journal of neurophysiology* **101,** 2550–2562.

Mäkiranta M, Ruohonen J, Suominen K, Niinimäki J, Sonkajärvi E, Kiviniemi V, Seppänen T, Alahuhta S, Jäntti V & Tervonen O (2005). BOLD signal increase preceeds EEG spike activity - A dynamic penicillin induced focal epilepsy in deep anesthesia. *NeuroImage* **27,** 715–724.

Manoochehri M, Mahmoudzadeh M, Bourel-Ponchel E & Wallois F (2017*a*). Cortical light scattering during interictal epileptic spikes in frontal lobe epilepsy in children: A fast optical signal and electroencephalographic study. *Epilepsia* **58,** 2064–2072.

Manoochehri M, Mahmoudzadeh M, Osharina V & Wallois F (2017*b*). Shedding light on interictal epileptic spikes: An in vivo study using fast optical signal and electrocorticography. *Epilepsia*1–9.

Masterton RAJ, Harvey AS, Archer JS, Lillywhite LM, Abbott DF, Scheffer IE & Jackson GD (2010). Focal epileptiform spikes do not show a canonical BOLD response in patients with benign rolandic epilepsy (BECTS). *NeuroImage* **51,** 252–260.

Matsumoto H & Marsan CA (1964). Cortical cellular phenomena in experimental epilepsy: Interictal manifestations. *Experimental Neurology* **9,** 286–304.

Matsumoto JY, Stead M, Kucewicz MT, Matsumoto AJ, Peters PA, Brinkmann BH, Danstrom JC, Goerss SJ, Marsh WR, Meyer FB & Worrell GA (2013). Network oscillations modulate interictal epileptiform spike rate during human memory. *Brain* **136,** 2444–2456.

McBain CJ, Traynelis SF & Dingledine R (1990). Regional variation of extracellular space in the hippocampus. *Science* **249,** 674–677.

McNaught AD (comp.), International Union of Pure and Applied Chemistry O (United K eng & Wilkinson A (comp.) (1997). Compendium of chemical terminology. IUPAC recommendations.

Mitzdorf U (1985). Current source-density method and application in cat cerebral cortex: Investigation of evoked potentials and EEG phenomena. *Physiological Reviews* **65,** 37–100.

Moeller F, Siebner HR, Wolff S, Muhle H, Granert O, Jansen O, Stephani U & Siniatchkin M (2008). Simultaneous EEG-fMRI in drug-naive children with newly diagnosed absence epilepsy. *Epilepsia* **49,** 1510–1519.

Moore CI & Cao R (2008). The hemo-neural hypothesis: On the role of blood flow in information processing. *Journal of Neurophysiology* **99,** 2035–2047.

Nicholson C & Freeman JA (1975). Theory of current source density analysis and determination of conductivity tensor for anuran cerebellum. *Journal of Neurophysiology* **38,** 356–368.

Nourhashemi M, Mahmoudzadeh M & Wallois F (2016). Thermal impact of near-infrared laser in advanced noninvasive optical brain imaging. *Neurophotonics* **3,** 015001.

Osharina V, Aarabi A, Manoochehri M, Mahmoudzadeh M & Wallois F (2017). Hemodynamic Changes Associated with Interictal Spikes Induced by Acute Models of Focal Epilepsy in Rats: A Simultaneous Electrocorticography and Near-Infrared Spectroscopy Study. *Brain Topography* **30,** 390–407.

Osharina V, Ponchel E, Aarabi A, Grebe R & Wallois F (2010). Local haemodynamic changes preceding interictal spikes: A simultaneous electrocorticography (ECoG) and near-infrared spectroscopy (NIRS) analysis in rats. *NeuroImage* **50,** 600–607.

Pettersen KH, Devor A, Ulbert I, Dale AM & Einevoll GT (2006). Current-source density estimation based on inversion of electrostatic forward solution: Effects of finite extent of neuronal activity and conductivity discontinuities. *Journal of Neuroscience Methods* **154,** 116–133.

Poe GR, Rector DM, Kristensen MP & Harper RM (1996). Concurrent reflectance imaging and microdialysis in the freely behaving cat. *Journal of Neuroscience Methods* **65,** 143–149.

Pouliot P, Tremblay J, Robert M, Vannasing P, Lepore F, Lassonde M, Sawan M, Nguyen DK & Lesage F (2012). Nonlinear hemodynamic responses in human epilepsy: A multimodal analysis with fNIRS-EEG and fMRI-EEG. *Journal of Neuroscience Methods* **204,** 326–340.

Rector DM, Poe GR, Kristensen MP & Harper RM (1997). Light Scattering Changes Follow Evoked Potentials From Hippocampal Schaeffer Collateral Stimulation. *Journal of Neurophysiology* **78,** 1707–1713.

Rossokhin A V., Sharonova IN, Bukanova J V., Kolbaev SN & Skrebitsky VG (2014). Block of GABAA receptor ion channel by penicillin: Electrophysiological and modeling insights toward the mechanism. *Molecular and Cellular Neuroscience* **63,** 72–82.

Saillet S, Quilichini PP, Ghestem A, Giusiano B, Ivanov AI, Hitziger S, Vanzetta I, Bernard C & Bénar CG (2016*a*). Interneurons contribute to the hemodynamic/metabolic response to epileptiform discharges. *Journal of Neurophysiology* **115,** 1157–1169.

Saillet S, Quilichini PP, Ghestem A, Giusiano B, Ivanov AI, Hitziger S, Vanzetta I, Bernard C & Bénar CG (2016*b*). Interneurons contribute to the hemodynamic/metabolic response to epileptiform discharges. *Journal of Neurophysiology* **115,** 1157–1169.

Salek-Haddadi A, Diehl B, Hamandi K, Merschhemke M, Liston A, Friston K, Duncan JS, Fish DR & Lemieux L (2006). Hemodynamic correlates of epileptiform discharges: An EEG-fMRI study of 63 patients with focal epilepsy. *Brain Research* **1088,** 148–166.

Schaefer MK, Hechavarría JC & Kössl M (2015). Quantification of mid and late evoked sinks in laminar current source density profiles of columns in the primary auditory cortex. *Frontiers in Neural Circuits* **9,** 52.

Scheffer IE, Berkovic S, Capovilla G, Connolly MB, French J, Guilhoto L, Hirsch E, Jain S, Mathern GW, Moshé SL, Nordli DR, Perucca E, Tomson T, Wiebe S, Zhang YH & Zuberi SM (2017). ILAE classification of the epilepsies: Position paper of the ILAE Commission for Classification and Terminology. *Epilepsia* **58,** 512–521.

Schwartz TH & Bonhoeffer T (2001). In vivo optical mapping of epileptic foci and surround inhibition in ferret cerebral cortex. *Nature Medicine* **7,** 1063–1067.

Schwartz TH, Hong SB, Bagshaw AP, Chauvel P & Bénar CG (2011). Preictal changes in cerebral haemodynamics: Review of findings and insights from intracerebral EEG. *Epilepsy Research* **97,** 252–266.

Senzai Y, Fernandez-Ruiz A & Buzsáki G (2019). Layer-Specific Physiological Features and Interlaminar Interactions in the Primary Visual Cortex of the Mouse. *Neuron* **101,** 500-513.e5.

Silfverhuth MJ, Kortelainen J, Ruohonen J, Suominen K, Niinimäki J, Sonkajärvi E, Kiviniemi V, Alahuhta S, Jäntti V, Tervonen O & Seppänen T (2011). A characteristic time sequence of epileptic activity in EEG during dynamic penicillin-induced focal epilepsy - A preliminary study. *Seizure* **20,** 513–519.

Somjen GG (2004). *Ions in the brain : normal function, seizures, and stroke*. Oxford University Press.

Sotero RC & Trujillo-Barreto NJ (2007). Modelling the role of excitatory and inhibitory neuronal activity in the generation of the BOLD signal. *NeuroImage* **35,** 149–165.

Sotero RC & Trujillo-Barreto NJ (2008). Biophysical model for integrating neuronal activity, EEG, fMRI and metabolism. *NeuroImage* **39,** 290–309.

Soukupová S, Mikolášová R, Kubová H & Mareš P (1993). New model of cortical epileptic foci in freely moving developing rats. *Epilepsy Research* **15,** 27–33.

Suh M, Bahar S, Mehta AD & Schwartz TH (2005). Temporal dependence in uncoupling of blood volume and oxygenation during interictal epileptiform events in rat neocortex. *Journal of Neuroscience* **25,** 68–77.

TASAKI I (1999). Rapid Structural Changes in Nerve Fibers and Cells Associated with Their Excitation Processes. *The Japanese Journal of Physiology* **49,** 125–138.

Tewolde S, Oommen K, Donald ;, Lie YC, Zhang Y & Chyu M-C (2015). *Epileptic Seizure Detection and Prediction Based on Continuous Cerebral Blood Flow Monitoring-a Review*.

Ulbert I, Heit G, Madsen J, Karmos G & Halgren E (2004). Laminar Analysis of Human Neocortical Interictal Spike Generation and Propagation: Current Source Density and Multiunit Analysis In Vivo. *Epilepsia* **45,** 48–56.

Vanzetta I, Flynn C, Ivanov AI, Bernard C & Bénar CG (2010). Investigation of linear coupling between single-event blood flow responses and interictal discharges in a model of experimental epilepsy. *Journal of neurophysiology* **103,** 3139–3152.

Voges N, Blanchard S, Wendling F, David O, Benali H, Papadopoulo T, Clerc M & Bénar C (2012). Modeling of the neurovascular coupling in epileptic discharges. *Brain Topography* **25,** 136–156.

Vongerichten AN, Santos GS dos, Aristovich K, Avery J, McEvoy A, Walker M & Holder DS (2016). Characterisation and imaging of cortical impedance changes during interictal and ictal activity in the anaesthetised rat. *NeuroImage* **124,** 813–823.

Wallois F, Mahmoudzadeh M, Manoochehri M & Bourel-Ponchel E (2018). S15. Shedding lights on interictal epliepyic spikes: An animal and patient study. *Clinical Neurophysiology* **129,** e147–e148.

Wallois F, Patil A, Héberlé C & Grebe R (2010). EEG-SPIR chez les patients épileptiques. *Neurophysiologie Clinique* **40,** 281–292.

Witte OW, Bruehl C, Schlaug G, Tuxhorn I, Lahl R, Villagran R & Seitz RJ (1994). Dynamic changes of focal hypometabolism in relation to epileptic activity. *Journal of the Neurological Sciences* **124,** 188–197.

Yao X-C, Rector DM & George JS (2003). Optical lever recording of displacements from activated lobster nerve bundles and Nitella internodes. *Applied Optics* **42,** 2972.

Zhang T, Zhou J, Jiang R, Yang H, Carney PR & Jiang H (2014). Pre-seizure state identified by diffuse optical tomography. *Scientific Reports* **4,** 1–10.

Zwiener U, Eiselt M, Gießler F & Nowak H (2000). Relations between early prespike magnetic field changes, interictal discharges, and return to basal activity in the neocortex of rabbits. *Neuroscience Letters* **289,** 103–106.

CHAPTER

4

Conclusions and Perspectives

4.1. Conclusions

In this thesis, to evaluate the dynamic of the neurovascular unit considering the interactions between the neuronal, vascular networks, and the extracellular space occurring around the IISs, a multimodal approach is developed in epileptic rats with induced IISs. Changes in neuronal vascular and extracellular environment were monitored *in vivo* by simultaneous electrocorticogram (ECoG), multisite linear electrodes (MLE), Fast-Optical Signal, (FOS), Near-Infrared Spectroscopy (NIRS) Diffuse Correlation Spectroscopy, (DCS).

The first change detected before the IIS was in the hemodynamic compartments (HbO_2, HbR, rCBF) a few seconds before the peak of the IIS. These hemodynamic variations were followed by changes in coherence, and then the synchronization between the deep and superficial neural networks, one second before the IIS peaks. Then, changes in light scattering occurred few hundreds of milliseconds (800 msec) before the IIS which support the idea of a change in membrane configuration occurring before the epileptic spikes.

4.1.1. Objectives review

The first objective was to develop a multimodal multiscale approach in an *in vivo* model that would allow to record the dynamic of the neuronal (synaptic and non-synaptic) and vascular compartments. For this purpose, we implemented a setup that combine simultaneous recording of the neuronal compartment (ECoG, LFP, MUA, SUA), of the vascular compartment (fNIRS, DCS) and of the extra cellular space (FOS).

Such simultaneous recording using different modalities requires a step of synchronization between the different devices. To perform a simultaneous multimodal recording *in vivo* activity, the positioning of all the probes (electrodes, optical fibers, etc.) within a relatively small area, that is the rat skull is a second step which requires a lot of attention . Creating a setup almost from scratch for the electrophysiological recordings was challenging. For this reason, I had to create a series of scripts to extract meaningful data and to perform the required analysis of both electrophysiological and hemodynamic data.

The recordings between NIRS and DCS were first assumed to be carried out jointly. Nevertheless, this was not possible because of the different sampling rates used for fNIRS, FOS and DCS. The different analyzes were applied compartment by compartment and then the time series were compared between modalities.

4.1.2. Achievements

The main achievements of this thesis are the followings:

I. Carry out the detection of what occurs at the synaptic level in the cerebral cortex in rats, using techniques such as EEG, LFP MUA and SUA, at a multilayer level and simultaneously. Synchronizing the different devices for subsequent analysis of the synaptic activity related to the IIS.

II. The development of analyzes to better understand the dynamic of synaptic neuronal modulations remated to IIS and occurring at different cortical layers.

III. The development of analysis procedure to evaluate the dynamic of the different compartments at the synaptic, non-synaptic and vascular level around the IIS. We also focus on the time delay relationship of this dynamic with the peak amplitude of the IIS. This approach allows confirming results obtained from previous studies with similar experiments on hemodynamics and membrane configuration. It also provides some new information’s about the dynamic of CBF and the changes in signal coherence between different cortical layers

IV. It shows that the dynamic is modified in the different compartments well before any changes at the cortical level as monitored by the ECoG.

V. It allows comparing the simultaneous changes occurring in different compartments around the IIS.

The development of signal processing like wavelet coherence analysis, cross frequency coupling or time-frequency analysis also improve my skill in the analysis in bio signal processing

4.2. Perspectives

In this thesis a multitude of techniques have been reviewed for the development of these setup, detection, registration, and processing of IISs at the synaptic, non-synaptic and vascular levels of the involved neuronal tissue. Although there is still a long way to go before a complete understanding of this pathology that affects millions of people over the world. The IIS are only one part of the puzzle that is still unsolved, and therefore needs to be thoroughly studied. The understanding of the physiopathology of the IIS and of the mechanisms that propels neurons to the IIS necessitate an approach at different levels. Such approach opens new avenue and e new perspectives for treatment and prevention.

4.2.1. The effects of the local hypothermia on the neurovascular coupling (NVC) in Penicillin G (PG) model as a treatment for IIS

Currently the alternative of anti-epileptic drugs, in case of pharmaco-resistant epilepsy are, brain surgeries, stimulation procedures, as well as a ketogenic diet. Another alternative would be local hypothermia to reduce the metabolism within the epileptogenic zone that was effective in suppressing epileptic seizures (Baldwin *et al.*, 1956; Hill *et al.*, 2000).

Local cortical cooling as treatment of epileptic discharges (EDs) has recently become a focus of research. Some authors report on newly invented cooling setups that implement a thermoelectric (Peltier) chip in experimental neocortical seizures (Yang & Rothman, 2001; Yang *et al.*, 2003; Fujioka *et al.*, 2010; Fujii *et al.*, 2012).

The present results of this thesis confirmed the existence of changes in dynamics at synaptic, non-synaptic and vascular levels. The multimodal approach we developed Might be used to better understand at which level of the different compartments the cooling has an effect. It might be a decrease in the firing rate, in the interaction between the different layers, in the response of the vascular system or even in the changes in the extracellular space due to less neuronal activation and less neuronal swelling.

To evaluate the changes in the different levels of activity (i.e. synaptic, non-synaptic and vascular levels) it is necessary to develop a cooling setup. The cooling system probe might be similar to those used in previous studies (Figure 4.1) (Yang & Rothman, 2001; Yang *et al.*, 2003; Imoto *et al.*, 2006). To measure the slow and fast optical signals (fNIRS and FOS) and DCS the optic fiber placement will be the same as we used in Chapter 2. The use of MLE and ECoG will be placed depending of the final size of cooling system, preferably a design that allows the insertion of the MLE described in Chapter 2.

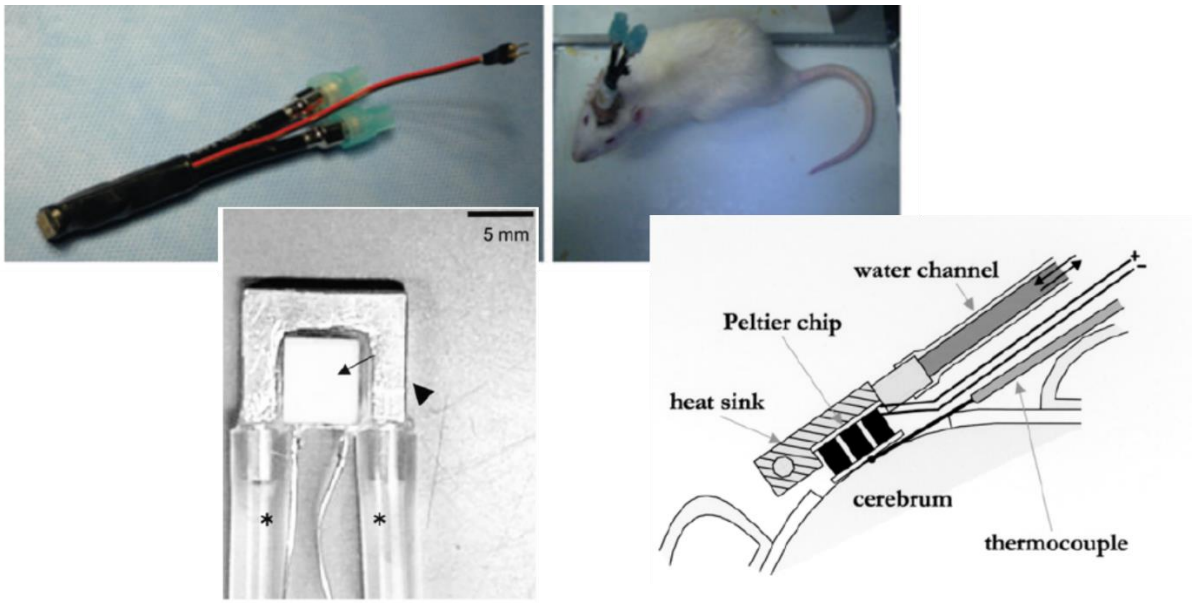

Figure 4.1. Example of the thermocouple used in rats (Imoto *et al.*, 2006; Fujii *et al.*, 2012)

Two groups will be analyzed: a control and an experimental group (Figure 4.2). The control group will be recorded with the cooling system procedure without epileptogenic drug. The experimental group will be recorded with the cooling system procedure with epileptogenic drug. Different levels of cooling are planned to define the optimal reduction of temperature that might modify the dynamic of one of the compartments around the IIS.

Within the hemodynamic compartment, the expected changes are a reduction in the rate of IIS, associated with less initial hemodynamic changes that might participate in less synchronization towards the IIS.

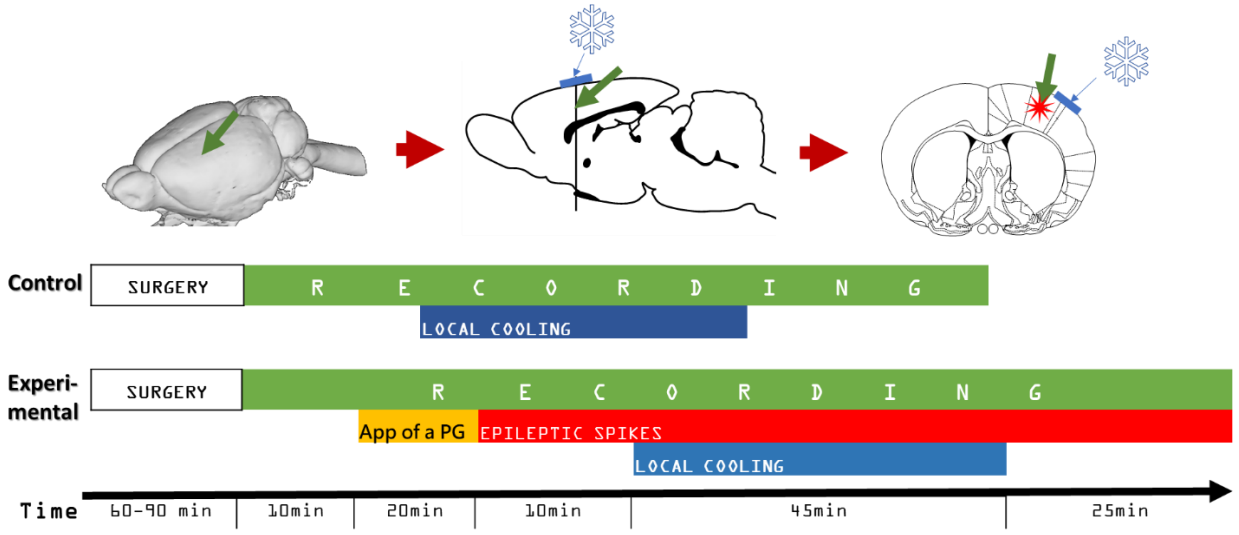

Figure 4.2. Schema of the 2 groups of recordings using cooling systems. On top, the exact cortical placement of the multi-site linear electrode (MLE) are marker in a green arrow, and injection of Penicillin G (PG) marked in a red asterisk. On bottom, the temporal sequences of the protocol for the brain measurements.

4.2.2. Study of the IIS interhemispheric propagation

Interestingly we might also have used multisite multielectrodes recordings to evaluate the spreading of the discharge at the different adjacent sites in the cortex (Castro-Alamancos, 2000; Wallois *et al.*, 2010; Proddutur & Santhakumar, 2016; Saillet *et al.*, 2016). Different configurations might be used to register more adjacent areas of the cortex (Saillet *et al.*, 2016) or with electrodes forming tetrodes for a better characterization of the unit activities (Blanche, 2005). The use of electrode/optode arrays covering a wider area of the cortical surface will provide a multimodal spatial representation of the interactions at the layer level in 3D, including a better representation of (1) the spatial spreading of the epileptic discharge, (2) the spatial hemodynamic changes, (3) the spatial extracellular changes, around the IIS. (Figure 4.3).

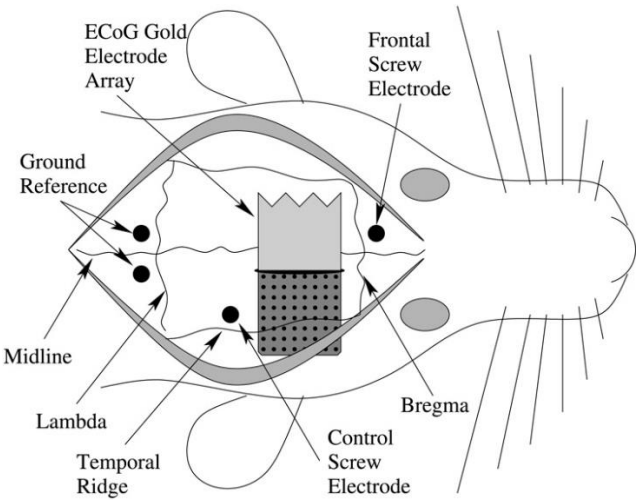

Figure 4.3. Example of one published protocol using ECoG array probe in rats (from Yeager *et al.*, 2008).

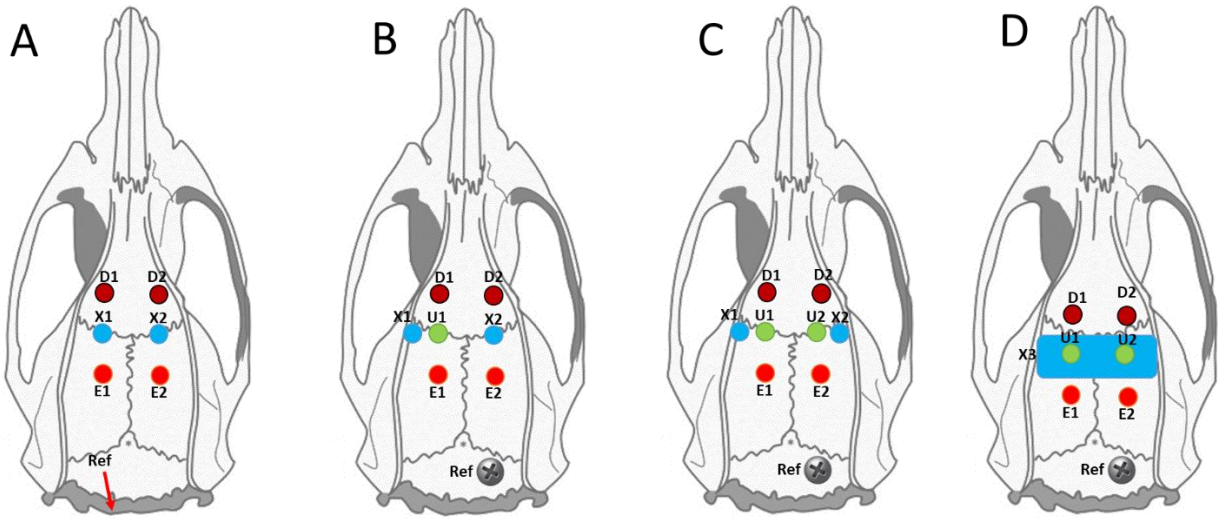

Figure 4.4. Past, present, and future probes placements on the different protocols of recordings. (A) Placements of previous papers (Osharina *et al.*, 2010, 2017; Manoochehri *et al.*, 2017). (B)Placement of the actual thesis proves. Where D1 and E1 are shared with DCS and NIRS optical probes. (C) Near future probe placements. (D) Near future probe placements, where X3 represent ECoG electrodes array. D1 and D2 are the NIRS detectors; E1 and E2 are the emitters of NIRS; U1 and U2 are the MLE location. X1, X2 and X3 are the ECoG probes; Ref. is the ground electrode placement.

CHAPTER

5

Supplementary information

5.1. Does the greater inter-spike interval create IISs with higher amplitude?

Objective

Based on the idea that in our IIS animal model a greater delay between IISs could lead to a greater amplitude of the IIs peaks, possibly due to a greater recovery of the transmitters involved at the neuronal level, the relationship between IIS interval and IIS amplitude was evaluated.

Data analysis

The voltages of each of the previously calculated IIS peaks were extracted and they were represented in figures where the voltage of the peaks was plotted on the Y-axis along the recording time in seconds of the different rats, in order to have an idea of how the peaks with higher voltage were distributed. Second, the ISI for each of the recorded IIS was calculated and plotted on histograms to observe how they were distributed in each rat. Finally, both data were linked to each other, assigning a value in millivolts to each time of T0, and represented in scatter plots. Subsequent analysis on linear regression such as polynomial curve fitting was applied to observe the trend. Finally, an analysis to find out the firing rate of the IISs was also carried out.

Results

The results showed that both the representation of the amplitude peaks, of the IISs, are not stable over time (Figure 1). The ISIs between the peaks of the IISs showed that they do not share a uniform distribution between the subjects (Figure 2). Both linear regression analysis and polynomial curve fitting analysis where performed and didn't show any conclusive results, then a restriction of ISIs >1 sec was applied due to the apparition of some IIS at 500ms. This second calculation of the linear regression did not return any conclusive results, on the other hand, the polynomial curve fitting analysis was successful in a pair of subjects, showing a greater amplitude with the larger ISI (Figure 3). The analysis on the firing rate of the IIS showed that the coefficient of variability of the firing rate remained below 35% with one important exception (85%) (Figure 4).

Discussion

In view of these inconclusive results, it cannot be assumed that the greater the distance between IIS the greater was the peak amplitude at T0, even if it was observed in rare cases.

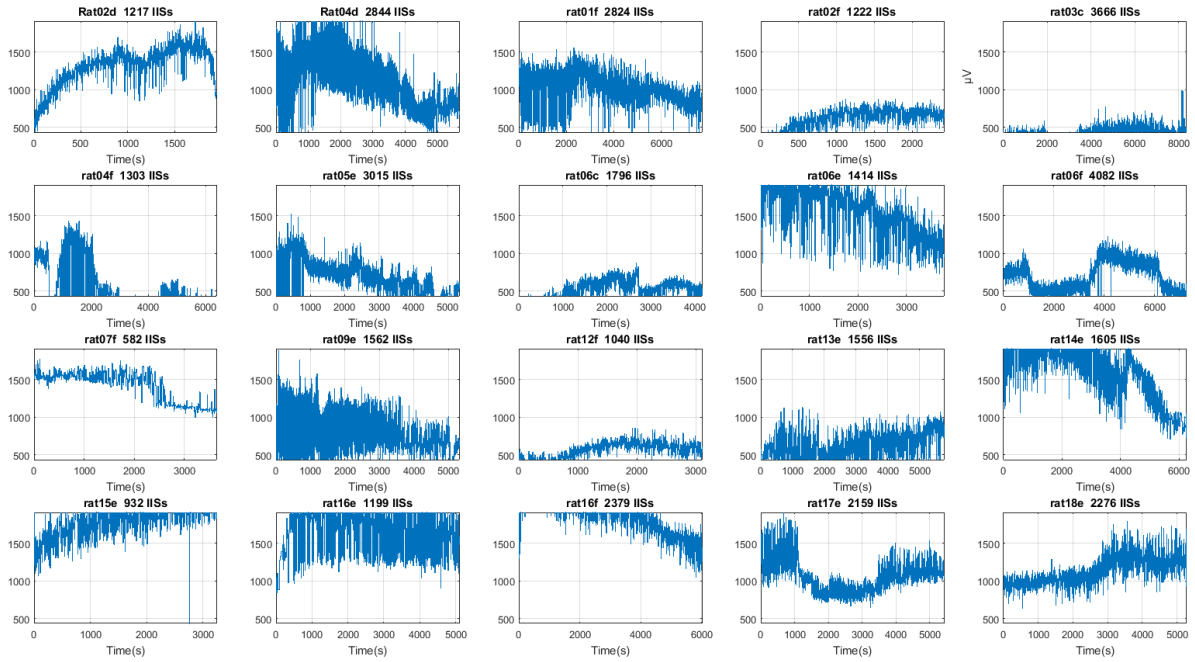

Figure 5.1. Voltage peak analysis along the recording of each rat.

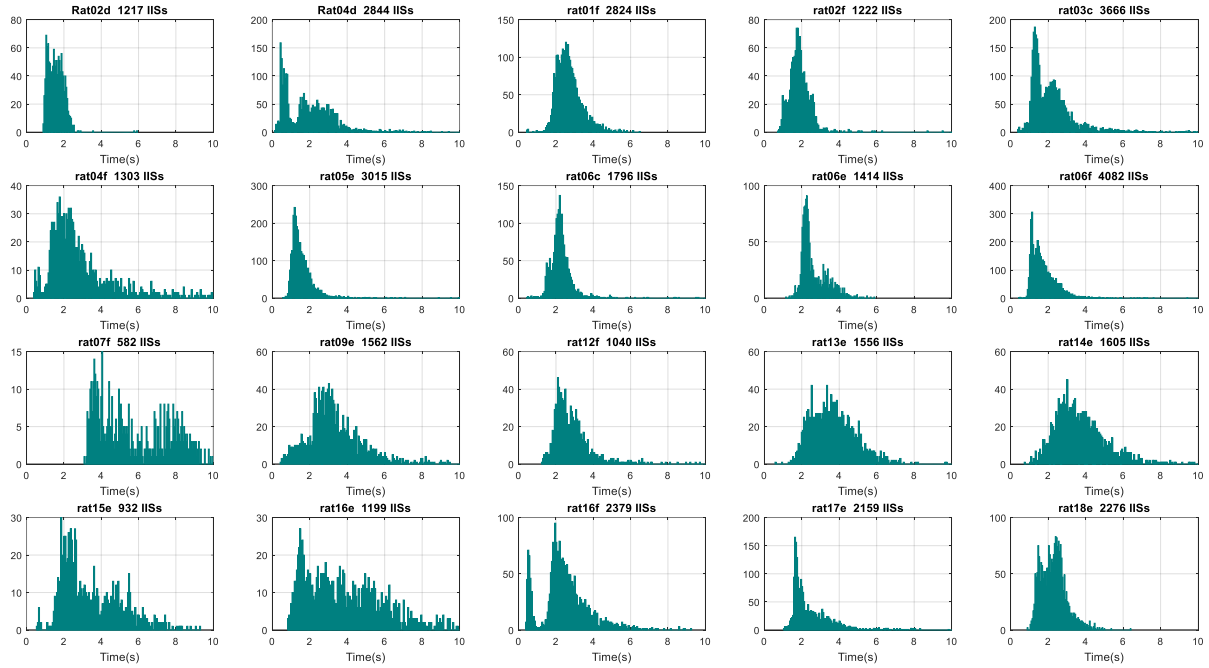

Figure 5.2. Inter-spike interval between the IISs of 20 rats. The rat code-name is shown at the top of each figure and the number of IISs used. The Y-axis represents the value of the counting bars and the X-axis the time between each pair of IISs.

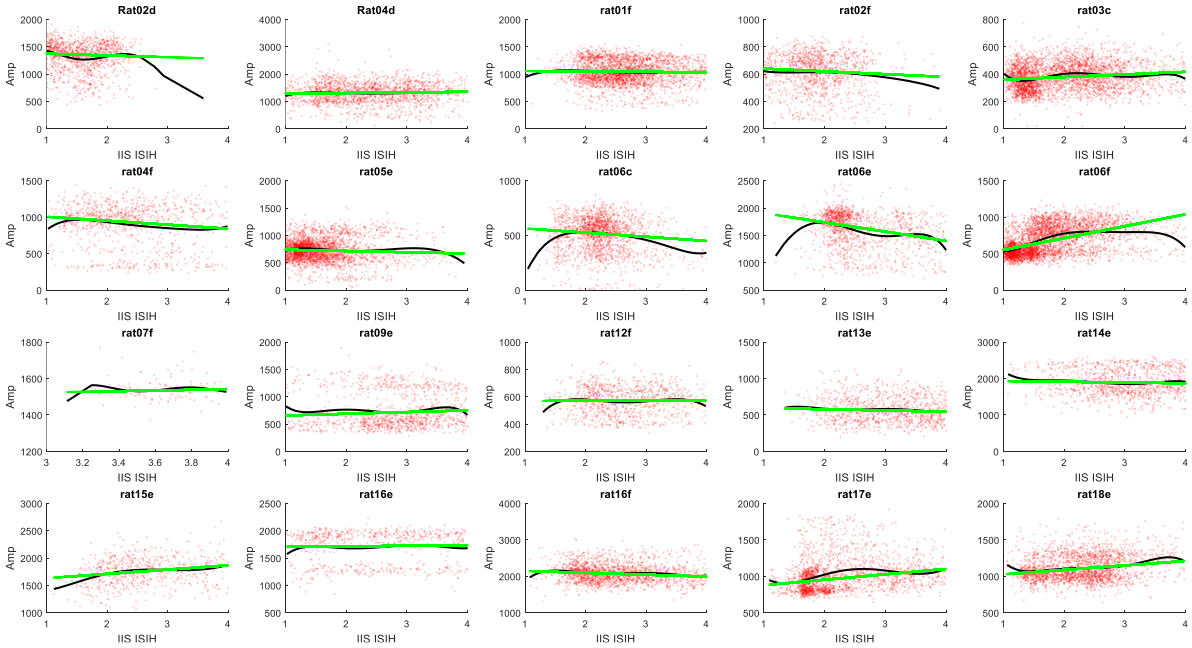

Figure 5.3. Scatter plot between the peak amplitudes and inter-spike interval times from 1 sec. The *green* lines represent the linear regression analysis, and the *black* line represent the polynomial curve fitting. Amplitude (Amp) in millivolts, IIS ISIH in seconds.

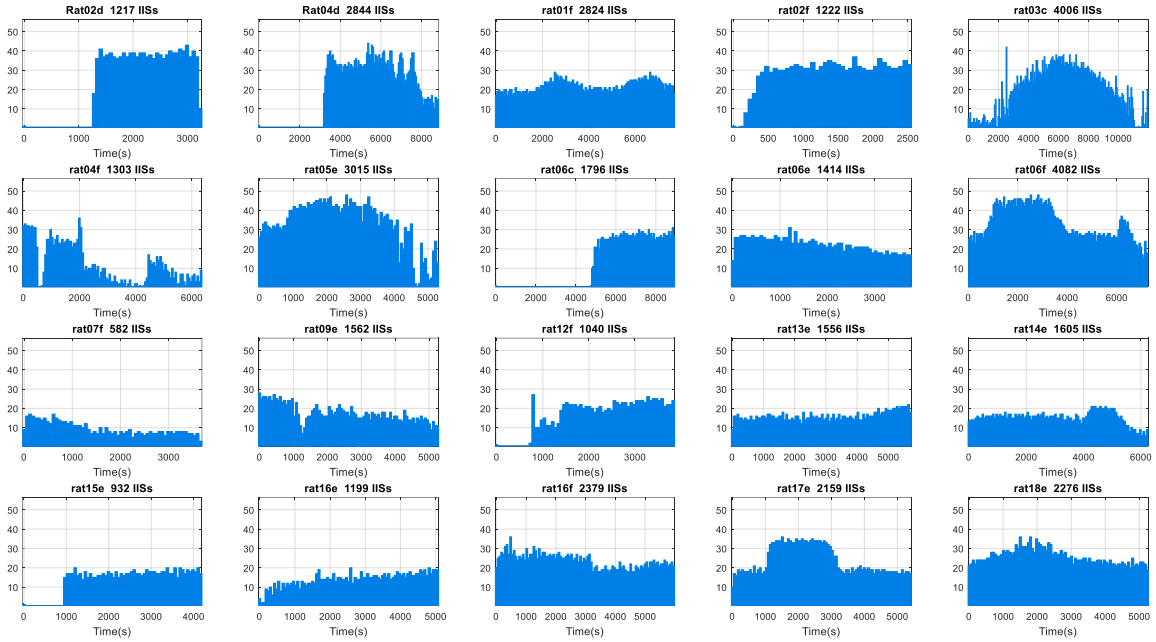

Figure 5.4. Counting of the firing rate per minute (Y-axis) along the recording time (X-axis).

5.2. Could the LFP signal predict the MUA onset surround the IIS?

Objective

The relationship between the superficial and deeper layers is discussed along the bibliography. To more precisely describe the relationship between different frequencies and IIS shapes along the cortical columns, an analysis about the peak of amplitude between the superficial and deep LFP were performed, including the power of the multi-unit activity.

Data analysis

A peak-to-peak analysis was computed for the superficial and deeper LFPs, surrounding the times of P1. If the shape similarities were more than 60%, the recording were discarded. To analyze the multi-unit activity (MUA), the channels (bandpass FIR filtered from 300 to 3000 Hz) with higher amplitudes were picked. the power peak parameters were then extracted (M1). From the deeper channel LFPs, the first valley (V1) and peak (V2), were extracted for each rat at the time interval of -100 ms to 100 ms of each IISs. A matrix was created with the times for P1, V1, V2 and M1, and Mann–Whitney *U* test was applied after setting each timing-peak as 0, for discover their relationship.

Results

Analyzing the phase locking value (PLV) at the IISs times between the superficial and deep channels, the PLVs mainly oscillate from 0 to 340º (range of 90º to 340º phase), but if the PLV is calculated for the MUA-power and the superficial LFP, the relevant phases are from 180º to 210º (range of 150º to 240º phase) (Figure 5A).

To study the role of the MUA, a peak-to-peak analysis was performed using the superficial, deep and MUA-power signals (Figure 5B). To analyze the data a condition of minimum 60% of difference, between the superficial and deep LFPs, were applied, and 11 recordings (total 6765 IISs) meet the condition. Peak times (M1, V1, V2) were aligned to P1 (set as time-0). It was found that in 27.3% of the cases the M1 appears 20 msec before P1 onset, 36.3% after 15 msec and the rest (36.4%) were close to P1 (<4 msec) (Figure 5C), with a total range of 34 msec. The next step was to align the peak times (M1, P1, V2) to the times of V1. In this case, the range of M1 was shorter (14 msec) with a significant relationship (p <0.05) (Figure 5C). In all cases, the data revealed that M1 could be inside the distance between V1 and V2 (range of 30 msec), located at the halfway of both (15 msec) 63.6% of the cases and in 36.4% in the first third of that distance. Although, a delay of 40 msec was observed between V1 and P1. In most cases (81,2%) V1 preceded P1.

Discussion

The results show an interesting relationship between the deep LFP (V1 and V2) with the M1. On one hand, the phase lock value suggested that the MUA appears in the rising part of the deeper LFP signals in all the rats. On the other hand, the P1 doesn't show a proper relationship with the M1. The relationship between the LFP and the MUA can be found in other analysis like CSD (Lakatos *et al.*, 2005; Quairiaux *et al.*, 2011). Other studies with dual single unit activity have shown that the activity recorded in the upper layer precede or (more commonly) follow the activity in the lower layer (Castro-Alamancos, 2000).

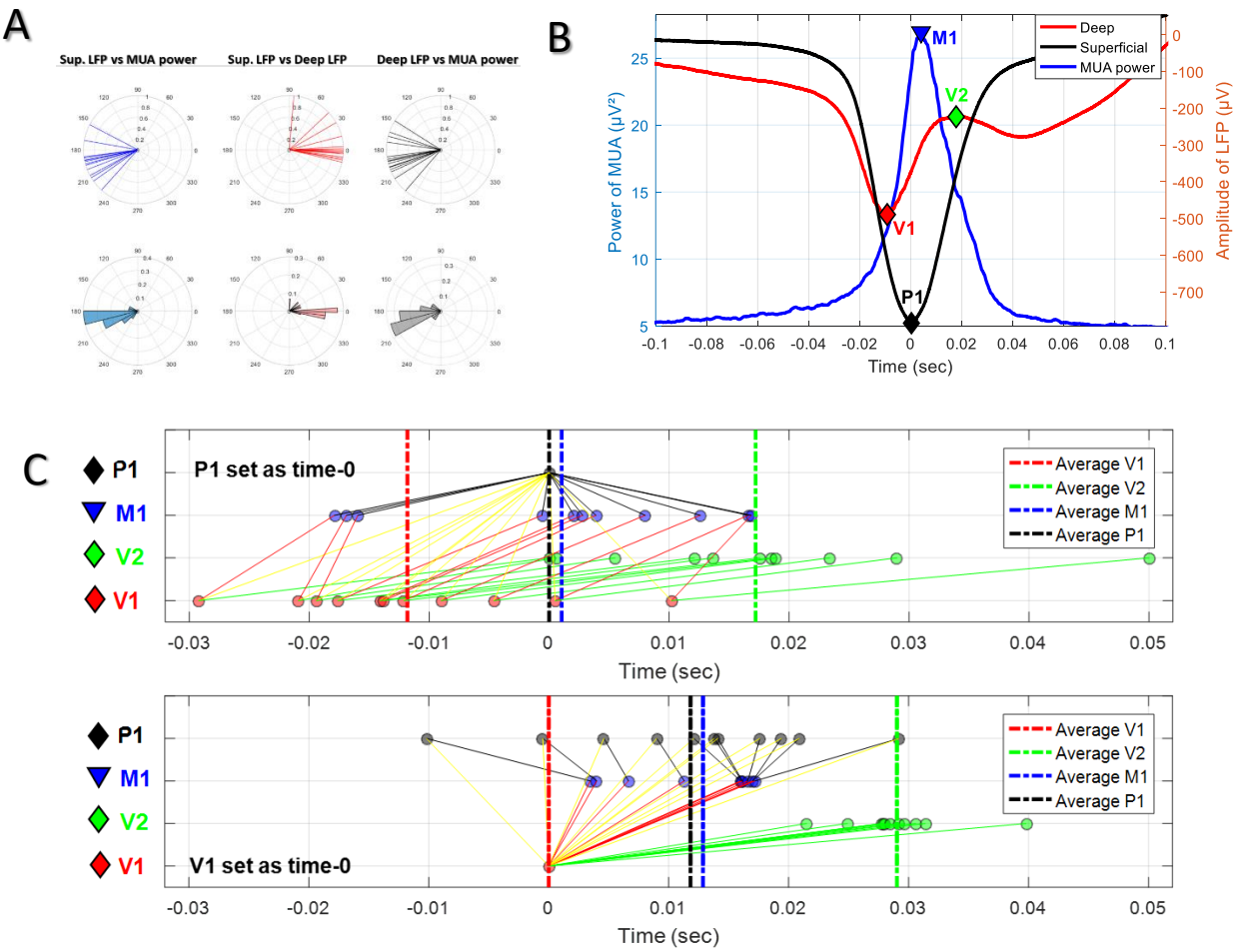

Figure 5.5. ***(A)*** Each line represents one rat phase-locking value for its pair of electrodes (superficial versus deep). *Blue* clocks (left) represent the PLV values of MUA power wave compared to superficial LFP oscillation. *Red* clocks (right) represent the PLV values of deeper LFP oscillation compared to the superficial one. ***(B)*** Representation of the peak extraction analysis of the MUA power (M1), the superficial channel peak of LFP (P1 of the IIS) and the valley (V1) and peak (V2) of the deepest channel LFP oscillation. ***(C)*** Times extracted from 11 rats, (*Top*) individually aligned to P1 (set as time-0) and (*Bottom*) individually aligned to V1 (set as time-00). The solid lines represent the data related individually for each rat.

CHAPTER

6

French summary

6.1. Aperçu de la thèse

Dans le *chapitre 1*, j'ai fait une brève introduction sur l'épilepsie, y compris l'épidémiologie, l'histoire et la classification pour introduire le modèle animal e pointes épileptiques intericales (IIS). Dans les parties suivantes, j'ai brièvement décrit les connaissances actuelles sur la dynamique des compartiments neuronaux et vasculaires liés aux décharges épileptiques intercritiques. J'ai ensuite décrit brièvement les principaux mécanismes du couplage neurovasculaire et sur ce qui est actuellement connu concernant la période pré-pointe de l'IIS. Enfin, d'autres perspectives telles que les changements dans l'espace extracellulaire au cours de l'IIS ont été brièvement passées en revue.

Dans les chapitres suivants, je vais présenter ma thèse, avec l'intention d'évaluer tous les changements qui peuvent être liés à l'IIS, y compris les approches électrophysiologiques (ECoG, LFP, UA et MUA), et l'imagerie optique (fNIRS y DCS), en mettant un accent particulier sur les périodes pré-IIS pour étudier comment elles sont générées.

Chapitre 2: Matériel et méthodes. Dans le chapitre 2, j'ai fait un tour d'horizon des différents systèmes utilisés pour réaliser une étude multimodale sur l'IIS. Les principales connaissances sur chaque méthodologie ont été brièvement décrites: (1) pour enregistrer les activités bioélectriques telles que ECoG

et MLE, (2) pour enregistrer les changements structurels neuronaux (FOS), (3) pour enregistrer l'activité hémodynamique (fNIRS) et (4) pour enregistrer le flux sanguin cérébral (DCS).

Chapitre 3: Résultats: Quels sont les mécanismes qui déclenchent la pointe épileptique intercritiques? Une analyse simultanée multimodale multi-échelles utilisant ECoG, MUA, NIRS, DCS et FOS chez le rat a été mise en oeuvre. Le chapitre 3 présente les principaux résultats de la thèse en cours de révision dans *Frontiers in Neurology*.

Chapitre 4: Conclusions et perspective. Dans le dernier chapitre, j'ai résumé les principales conclusions et les perspectives d'avenir.

6.2. Objectif et contributions de cette thèse

Cette thèse vise à analyser les différents mécanismes qui propulsent les neurones vers une synchronisation épileptique aberrante en développant une approche multi-échelle multimodale combinée des compartiments neuronaux, hémodynamiques et extracellulaires. Pour répondre à cet objectif, nous avons développé une activité combinée l'ECoG, la LFP et les enregistrements multi-unitaires (Neuronal), la NIRS et la spectroscopie de corrélation de diffusion (DCS) (hémodynamique) ainsi que les enregistrements de signaux optiques rapides (espace extra cellulaire). Cette approche permet d'aborder (1) l'activation d'un grand ensemble de neurones (ECoG) (2) l'activité mono et multi-unitaire (UA et MUA), (3) le couplage neurovasculaire (NIRS, DCS) et les changements de l'espace extracellulaire (FOS) se produisant autour de l'IIS. En raison de leurs résolutions temporelles élevées, ces techniques permettent de suivre les changements observés pendant les périodes pré-pointe, pointe et post-pointe.

Les contributions principales de cette thèse sont les suivantes:

- Développer un modèle animal qui permet des mesures simultanément: (1) les activités électrophysiologiques incluant l'électroencéphalogramme (EEG), les potentiels de champ local (LFP), les activités multi-unitaires et unitaires (MUA et UA) (2) les changements hémodynamiques (fNIRS et DCS) (3) les changements dans l'espace extracellulaire (FOS).
- Analyser la dynamique des différents compartiments pour mieux comprendre les mécanismes qui propulsent les neurones vers l'hypersynchronisation pendant l'IIS.
- Évaluer la dynamique des compartiments non synaptique et vasculaire ainsi que les activités synaptiques.

6.3. Étude

Qu'est-ce qui déclenche le pic épileptique intericta? Une analyse multimodale multi-échelles de la dynamique des compartiments neuronaux et vasculaires synaptiques et non-synaptiques à l'aide de mesures électriques et optiques

6.3.1. Objectif

Les pointes épileptique intercritiques (IIS) se caractérise par une augmentation de l'activité neuronale due au déséquilibre du réseau sous-jacent entre les cellules neuronales (synaptiques et non-synaptiques), vasculaires et métaboliques. Pour caractériser les interactions complexes entre les différents mécanismes liés aux IIS, il est nécessaire de développer et d'appliquer une approche globale qui révèle comment fonctionnent les différents compartiments. Dans un modèle de rat épileptique, nous avons évalué simultanément les changements synaptiques en enregistrant simultanément les enregistrements d'électrocorticographie (ECoG) et d'électrode linéaire multi-site (MLE) dans le domaine temps et temps-fréquence; la dynamique non synaptique en enregistrant les modifications de la diffusion de la lumière induites par les modifications de la configuration membranaire des cellules liées à l'augmentation de l'activité neuronale à l'aide du signal optique rapide (FOS); la dynamique vasculaire autour de l'activité IIS en utilisant la spectroscopie fonctionnelle proche infrarouge (fNIRS) et, indépendamment s mais synchronisées avec l'IIS, les changements dans le débit sanguin cérébral (rCBF) en utilisant la spectroscopie à corrélation de diffusion (DCS). Cette étude démontre que l'approche multimodale et multi-échelles mentionnée (ECoG, MLE, fNIRS, FOS et DCS) met en évidence la complexité des interactions entre les compartiments.

6.3.2. Matériel et méthodes

Des enregistrements ont été réalisés sur 43 mâles adultes Sprague-Dawley. Chaque rat a été pesé et anesthésié avec de l'uréthane avec une seule injection intrapéritonéale. La température corporelle, la respiration et la fréquence cardiaque ont été surveillées. Une partie du cuir chevelu a été enlevée et l'animal placé dans un cadre stéréotaxique pour exposer le crâne. Huit trous de craniotomie ont été forés à des coordonnées déterminées (Figure 1). Une dose de pénicilline G a été appliquée au cortex à travers le trou situé sur l'hémisphère gauche pour évoquer les IIS. Dans le même trou, un MLE à 16 sites a été introduit de 2,5 à 3 mm à un angle de 90 ° par rapport à la surface corticale pour enregistrer l'ensemble du cortex colonnaire. Ensuite, les électrodes plaquées or, monopolaires, ECoG, ont été insérées dans deux trous désignés. Les fréquences d'échantillonnage des signaux MLE et ECoG étaient de 20 kHz et 1024 Hz par canal, respectivement.

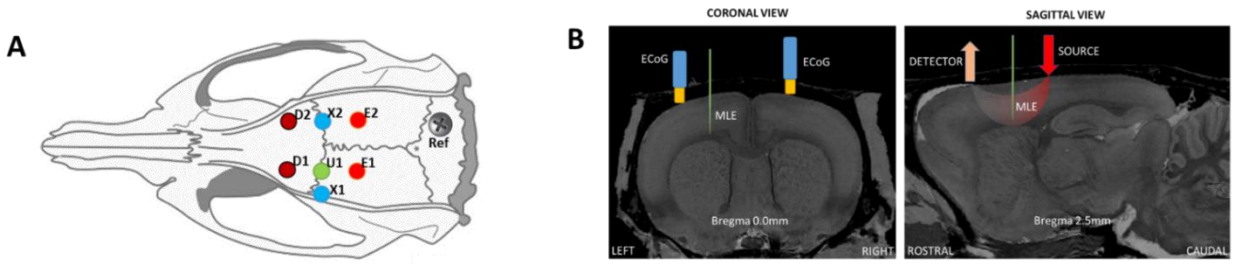

Figure 1. Représentation schématique de l'emplacement de l'ECoG et des sondes optiques sur une tête de rat. **(A)** Positions des sondes optiques, électrodes MLE et ECoG dans le cortex de rat: D1 et D2, détecteurs des spectromètres (antéro-postérieur (AP) 2,5 mm médial-latéral (ML) 2,5 mm); X1 et X2, électrodes ECoG (X1 à AP 0 mm ML 3,5 mm; X2 à AP 0 mm ML 2,5 mm); et U1, électrode linéaire multi-sites (AP 0 mm ML 2,5 mm), avec sa référence. **(B)** Vues coronales et sagittales dans l'atlas MRI pour les rats Sprague-Dawley (Papp *et al.*, 2014). *Côté gauche*: les électrodes MLE et ECoG à Bregma 0,0 mm, coupe coronale. *Côté droit*; placement de l'optode du détecteur et de la source lumineuse avec MLE, coupe sagittale (Bregma 2,5 mm).

Les activités hémodynamiques cérébrales ont été mesurées par la NIRS en plaçant une paire d'émetteurs de lumière à fibre optique (chaque paire avec des longueurs d'onde de 690 nm et 830 nm). La fréquence d'échantillonnage des détecteurs a été réglée à 156,25 Hz pour accéder aux changements d'absorption de la lumière (fNIRS) et de diffusion de la lumière (FOS). Un dispositif DCS a été utilisé pour quantifier de manière non invasive les changements de CBF. Les enregistrements ont commencé 20 minutes avant la perfusion de pénicilline G et se sont poursuivis pendant 3 à 4 heures.

Les données acquises ont été analysées principalement aux époques d'apparition de l'IIS. Ce signal a été prélevé sur le canal MLE le plus proche de la surface, et ses propriétés électriques ont été caractérisées. Dans les enregistrements intracorticaux, des analyses telles que la densité de courant-source (CSD), la wavelet-cohérence, la représentation temps-fréquence (TFR), le tri des pointes et l'analyse des activités rapides ont été effectuées. L'activité hémodynamique cérébrale, les activités FOS et rCBF ont été calculées et synchronisées avec l'IIS.

6.3.3. Résultats et conclusions

Nous avons identifié des changements complexes dans les paramètres hémodynamiques, qui ont commencé à être significatifs environ 8 secondes avant le pic de l'IIS, en accord avec les études précédentes réalisées par fNIRS sur des rats et des humains. Nos résultats sont également cohérents avec ceux rapportés par l'IRMf et les études d'imagerie optique de patients épileptiques et d'animaux montrant que des changements hémodynamiques peuvent survenir pendant la période précédant la pointe. Cela confirme que les modifications de l'activité hémodynamique commencent avant l'IIS, avant toute modification visible des signaux électrocorticaux.

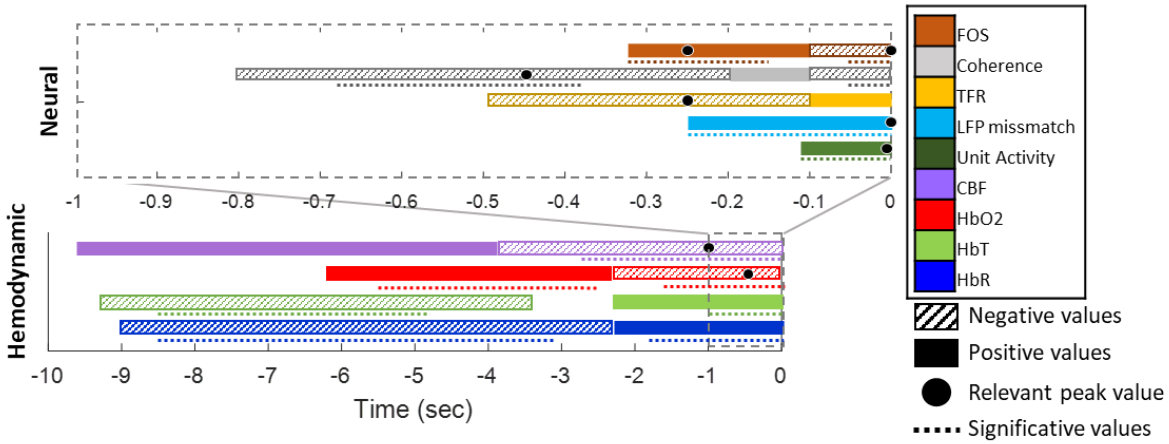

Figure 2. Résumé de tous les résultats basés sur les valeurs croissantes ou décroissantes des activités hémodynamiques et neuronales pendant la période pré-IIS. Les couleurs et motifs des barres sont expliqués dans la légende à droite. Les barres représentent les valeurs moyennes (positives ou négatives) et les lignes pointillées les périodes significatives pour chaque analyse.

L'analyse de wavelet-cohérence permet de quantifier la similitude en temps-fréquence (corrélation) entre les activités LFP et MUA à différents canaux. Nos résultats suggèrent des changements dans les interactions entre les différentes couches qui commencent 1 sec avant l'IIS, à l'inversion du CBF. Dans certains enregistrements unitaires, nous avons observé une diminution ou une augmentation concomitante de l'activité de décharge unitaire environ -0,8 s avant le pic d'IIS, ce qui suggère que cette diminution de la corrélation (décorrélation) peut être associée à un changement du schéma de l'activité neuronal.

Les modifications des propriétés optiques du tissu neuronal (FOS) consistaient en une augmentation de la détection de la lumière, correspondant à une diminution de la diffusion, suggérant le rétrécissement des neurones et/ou des astrocytes, entraînant une augmentation de l'espace extracellulaire.

Les changements dans les compartiments neuronaux et extracellulaires semblaient être symétriques autour de l'IIS, à l'exception des changements hémodynamiques. Comme précédemment observé par TFR, la décorrélation entre les canaux superficiels et plus profonds dans la présente étude suggère une alternance de downstate-upstate-downstate. En résumé, le rétrécissement-gonflement-rétrécissement cellulaire, ou une augmentation-diminution-augmentation de l'espace extracellulaire, concomitante avec une diminution-augmentation-diminution simultanée des données en TFR. Des changements symétriques se produisent dans la cohérence entre les couches superficielles, et sont présents autour de l'IIS ainsi que lors de l'augmentation de CBF et d'HbO_2 à partir de leurs valeurs les plus basses.

En conclusion, notre approche multimodale et multi-échelles met en évidence la complexité des interactions entre les différents compartiments neuronaux, vasculaires et extracellulaires, y compris les interactions neuronales entre différentes couches ainsi que complexité des mécanismes synaptiques (cohérence et synchronisation) et non-synaptiques qui se mettent en place dans le réseau neuronal autour des IIS dans un environnement hémodynamique cérébral très spécifique (Figure 2).

References

Aarabi A, Osharina V & Wallois F (2017). Effect of confounding variables on hemodynamic response function estimation using averaging and deconvolution analysis: An event-related NIRS study. *Neuroimage* **155,** 25–49.

Abeles M & Goldstein MH (1977). Multispike train analysis. *Proc IEEE* **65,** 762–773.

Agarwal A & Lang J (2005). *Foundations of analog and digital electronic circuits*. Elsevier.

Anderson WW, Lewis D V, Swartzwelder HS & Wilson WA (1986). Magnesium-free medium activates seizure-like events in the rat hippocampal slice. *Brain Res* **398,** 215–219.

Andrew RD & Macvicar BA (1994). Imaging cell volume changes and neuronal excitation in the hippocampal slice. *Neuroscience* **62,** 371–383.

Asano E, Muzik O, Shah A, Juhász C, Chugani DC, Sood S, Janisse J, Ergun EL, Ahn-Ewing J & Shen C (2003). Quantitative interictal subdural EEG analyses in children with neocortical epilepsy. *Epilepsia* **44,** 425–434.

Ashwood TJ, Lancaster B & Wheal H V (1986). Intracellular electrophysiology of CA1 pyramidal neurones in slices of the kainic acid lesioned hippocampus of the rat. *Exp brain Res* **62,** 189–198.

Attwell D & Laughlin SB (2001). *An Energy Budget for Signaling in the Grey Matter of the Brain*.

Azevedo FAC, Carvalho LRB, Grinberg LT, Farfel JM, Ferretti REL, Leite REP, Filho WJ, Lent R & Herculano-Houzel S (2009). Equal numbers of neuronal and nonneuronal cells make the human brain an isometrically scaled-up primate brain. *J Comp Neurol* **513,** 532–541.

Baldwin M, Frost LL, Wood CD & Lewis SA (1956). Effect of hypothermia on epileptiform activity in the primate temporal lobe. *Science (80-)* **124,** 931–932.

Banerjee PN, Filippi D & Allen Hauser W (2009). The descriptive epidemiology of epilepsy-A review. *Epilepsy Res* **85,** 31–45.

Barkmeier DT & Loeb JA (2009). An animal model to study the clinical significance of interictal spiking. *Clin EEG Neurosci* **40,** 234–238.

Bergers G & Song S (2005). The role of pericytes in blood-vessel formation and maintenance. *Neuro Oncol* **7,** 452–464.

Blanche TJ (2005). Polytrodes: High-Density Silicon Electrode Arrays for Large-Scale Multiunit Recording. *J Neurophysiol* **93,** 2987–3000.

Blanco A & Blanco G (2017). Chapter 14—Carbohydrate metabolism. *Med Biochem Blanco, A, Blanco, G, Eds*283–323.

Blatt M, Wiseman S & Domany E (1996). Superparamagnetic clustering of data. *Phys Rev Lett* **76,** 3251.

Bourel-Ponchel E, Mahmoudzadeh M, Delignières A, Berquin P & Wallois F (2017). Non-invasive, multimodal analysis of cortical activity, blood volume and neurovascular coupling in infantile spasms using EEG-fNIRS monitoring. *NeuroImage Clin* **15,** 359–366.

Bozkurt A & Onaral B (2004). Safety assessment of near infrared light emitting diodes for diffuse optical measurements. *Biomed Eng Online* **3,** 1–10.

Brown LS, Foster CG, Courtney JM, King NE, Howells DW & Sutherland BA (2019). Pericytes and neurovascular function in the healthy and diseased brain. *Front Cell Neurosci* **13,** 282.

Buxton RB, Wong EC & Frank LR (1998). Dynamics of blood flow and oxygenation changes during brain activation: the balloon model. *Magn Reson Med* **39,** 855–864.

Buzsáki G (2004). Large-scale recording of neuronal ensembles. *Nat Neurosci* **7,** 446–451.

Buzsáki G & Chrobak JJ (1995). Temporal structure in spatially organized neuronal ensembles: a role for interneuronal networks. *Curr Opin Neurobiol* **5,** 504–510.

Castro-Alamancos MA (2000). Origin of synchronized oscillations induced by neocortical disinhibition in vivo. *J Neurosci* **20,** 9195–9206.

Cauli B, Tong XK, Rancillac A, Serluca N, Lambolez B, Rossier J & Hamel E (2004). Cortical GABA interneurons in neurovascular coupling: Relays for subcortical vasoactive pathways. *J Neurosci* **24,** 8940–8949.

Chamberlin NL, Traub RD & Dingledine R (1990). Role of EPSPs in initiation of spontaneous synchronized burst firing in rat hippocampal neurons bathed in high potassium. *J Neurophysiol* **64,** 1000–1008.

Chang C & Glover GH (2010). Time–frequency dynamics of resting-state brain connectivity measured with fMRI. *Neuroimage* **50,** 81–98.

Chatrian E (1974). A glossary of terms most commonly used by clinical electroencephalographers. *Electroencephalogr Clin Neurophysiol* **37,** 538–548.

Cobb SR, Buhl EH, Halasy K, Paulsen O & Somogyi P (1995). Synchronization of neuronal activity in hippocampus by individual GABAergic interneurons. *Nature* **378,** 75–78.

Cohen LB (1973). *Changes in Neuron Structure During Action Potential Propagation and Synaptic Transmission*.

Cosandier-Rimélé D, Badier JM, Chauvel P & Wendling F (2007). A physiologically plausible spatio-temporal model for EEG signals recorded with intracerebral electrodes in human partial epilepsy. *IEEE Trans Biomed Eng* **54,** 380–388.

De Curtis M & Avanzini G (1994). Thalamic regulation of epileptic spike and wave discharges. *Funct Neurol* **9,** 307–326.

De Curtis M & Avanzini G (2001). Interictal spikes in focal epileptogenesis. *Prog Neurobiol* **63,** 541–567.

De Curtis M & Avoli M (2016). GABAergic networks jump-start focal seizures. *Epilepsia* **57,** 679–687.

de Curtis M, Jefferys JGR & Avoli M (2012). *Interictal Epileptiform Discharges in Partial Epilepsy: Complex Neurobiological Mechanisms Based on Experimental and Clinical Evidence*. National Center for Biotechnology Information (US).

De Curtis M, Manfridi A & Biella G (1998). *Activity-Dependent pH Shifts and Periodic Recurrence of Spontaneous Interictal Spikes in a Model of Focal Epileptogenesis*.

De Curtis M, Radici C & Forti M (1999). Cellular mechanisms underlying spontaneous interictal spikes in

an acute model of focal cortical epileptogenesis. *Neuroscience* **88,** 107–117.

Denda M, Tsutsumi M & Denda S (2010). Topical application of TRPM8 agonists accelerates skin permeability barrier recovery and reduces epidermal proliferation induced by barrier insult: role of cold-sensitive TRP receptors in epidermal permeability barrier homoeostasis. *Exp Dermatol* **19,** 791–795.

Diaz-Flores L, Gutierrez R, Varela H, Rancel N & Valladares F (1991). *Invited Revie W Microvascular pericytes: a review of their morphological and functional characteristics*.

Dore-Duffy P (2008). Pericytes: Pluripotent Cells of the Blood Brain Barrier. *Curr Pharm Des* **14,** 1581–1593.

Dowben RM & Rose JE (1953). A metal-filled microelectrode. *Science (80-)* **118,** 22–24.

Dragic S & Pavlovic V (2004). Penicillin epilepsy in rats. *Acta Medica Median* **43,** 19–23.

Duarte FS, Gavioli EC, Duzzioni M, Hoeller AA, Canteras NS & Delima TCM (2010). Short- and long-term anxiogenic effects induced by a single injection of subconvulsant doses of pilocarpine in rats: Investigation of the putative role of hippocampal pathways. *Psychopharmacology (Berl)* **212,** 653–661.

Durduran T, Choe R, Baker WB & Yodh AG (2010). Diffuse optics for tissue monitoring and tomography. *Reports Prog Phys*; DOI: 10.1088/0034-4885/73/7/076701.

Durduran T & Yodh AG (2014). Diffuse correlation spectroscopy for non-invasive, micro-vascular cerebral blood flow measurement. *Neuroimage* **85,** 51–63.

Duvernoy HM, Delon S & Vannson JL (1981). Cortical blood vessels of the human brain. *Brain Res Bull* **7,** 519–579.

Edmonds HL, Stark LG & Hollinger MA (1974). The effects of diphenylhydantoin, phenobarbital, and diazepam on the penicillin-induced epileptogenic focus in the rat. *Exp Neurol* **45,** 377–386.

Egert U, Schlosshauer B, Fennrich S, Nisch W, Fejtl M, Knott T, Müller T & Hämmerle H (1998). A novel organotypic long-term culture of the rat hippocampus on substrate-integrated multielectrode arrays. *Brain Res Protoc* **2,** 229–242.

Elston GN (2003). Cortex, cognition and the cell: new insights into the pyramidal neuron and prefrontal function. *Cereb cortex* **13,** 1124–1138.

Fabiani M, Gratton G & Corballis PM (1996). Noninvasive near infrared optical imaging of human brain function with subsecond temporal resolution. *J Biomed Opt* **1,** 387–399.

Faingold CL (1999). Neuronal networks in the genetically epilepsy-prone rat. *Adv Neurol* **79,** 311.

Ferrari M & Quaresima V (2012). A brief review on the history of human functional near-infrared spectroscopy (fNIRS) development and fields of application. *Neuroimage* **63,** 921–935.

Fisahn A, Pike FG, Buhl EH & Paulsen O (1998). Cholinergic induction of network oscillations at 40 Hz in the hippocampus in vitro. *Nature* **394,** 186–189.

Fischl B & Dale AM (2000). Measuring the thickness of the human cerebral cortex from magnetic resonance images. *Proc Natl Acad Sci U S A* **97,** 11050–11055.

Fisher RS, Acevedo C, Arzimanoglou A, Bogacz A, Cross JH, Elger CE, Engel Jr J, Forsgren L, French JA & Glynn M (2014). ILAE official report: a practical clinical definition of epilepsy. *Epilepsia* **55,** 475–482.

Fisher RS, Boas WVE, Blume W, Elger C, Genton P, Lee P & Engel Jr J (2005). Epileptic seizures and epilepsy: definitions proposed by the International League Against Epilepsy (ILAE) and the International Bureau for Epilepsy (IBE). *Epilepsia* **46,** 470–472.

Fountain NB, Bear J, Bertram III EH & Lothman EW (1998). Responses of deep entorhinal cortex are epileptiform in an electrogenic rat model of chronic temporal lobe epilepsy. *J Neurophysiol* **80,** 230–240.

Fox PT & Raichle ME (1986). Focal physiological uncoupling of cerebral blood flow and oxidative metabolism during somatosensory stimulation in human subjects. *Proc Natl Acad Sci* **83,** 1140–1144.

Freeman WJ & van Dijk BW (1987). Spatial patterns of visual cortical fast EEG during conditioned reflex in a rhesus monkey. *Brain Res* **422,** 267–276.

Fröhlich F (2016). *Network neuroscience*. Academic Press.

Fujii M, Inoue T, Nomura S, Maruta Y, He Y, Koizumi H, Shirao S, Owada Y, Kunitsugu I, Yamakawa T, Tokiwa T, Ishizuka S, Yamakawa T & Suzuki M (2012). Cooling of the epileptic focus suppresses seizures with minimal influence on neurologic functions. *Epilepsia* **53,** 485–493.

Fujii T & Ibata Y (1982). Effects of heating on electrical activities of guinea pig olfactory cortical slices. *Pflügers Arch* **392,** 257–260.

Fujioka H, Fujii M, Koizumi H, Imoto H, Nomura S, Saito T, Yamakawa T & Suzuki M (2010). An implantable, focal brain cooling device suppresses nociceptive pain in rats. *Neurosci Res* **66,** 402–405.

Fujita H, Kuwabara H, Reutens DC & Gjedde A (1999). Oxygen consumption of cerebral cortex fails to increase during continued vibrotactile stimulation. *J Cereb Blood Flow Metab* **19,** 266–271.

Garcia-Albea (1999). Las primeras descripciones escritas. In *Historia de la Epilepsia*, pp. 5–9. Masson, Barcelona.

Gasteiger EL, Albowitz B & Barken FM (1985). Interictal afterdischarge in focal penicillin epilepsy: Block by thalamic cooling. *Exp Neurol* **88,** 349–359.

Gloor P (1991). Mesial temporal sclerosis: historical background and an overview from a modern perspective. *Epilepsy Surg*689–703.

Gold C, Henze DA, Koch C & Buzsaki G (2006). On the origin of the extracellular action potential waveform: a modeling study. *J Neurophysiol* **95,** 3113–3128.

Gordon GRJ, Choi HB, Rungta RL, Ellis-Davies GCR & MacVicar BA (2008). Brain metabolism dictates the polarity of astrocyte control over arterioles. *Nature* **456,** 745–750.

Gordon GRJ, Howarth C & MacVicar BA (2011). Bidirectional control of arteriole diameter by astrocytes. *Exp Physiol* **96,** 393–399.

Gotman J (1984). Relationships between triggered seizures, spontaneous seizures, and interictal spiking in the kindling model of epilepsy. *Exp Neurol* **84,** 259–273.

Gotman J & Pittau F (2011). Combining EEG and fMRI in the study of epileptic discharges. *Epilepsia* **52,** 38–42.

Grant AC, O'Halloran JP, Chung SS, Gibbs W & Kaplan PW (2006). Evaluation of a novel EEG preamplifier. *J Clin Neurophysiol* **23,** 258–264.

Gratton G & Fabiani M (1998). Dynamic brain imaging: Event-related optical signal (EROS) measures of the time course and localization of cognitive-related activity. *Psychon Bull Rev* **5,** 535–563.

Gratton G & Fabiani M (2010). Fast optical imaging of human brain function. *Front Hum Neurosci* **4,** 52.

Gray CM, Maldonado PE, Wilson M & McNaughton B (1995). Tetrodes markedly improve the reliability and yield of multiple single-unit isolation from multi-unit recordings in cat striate cortex. *J Neurosci Methods* **63,** 43–54.

Grinsted A, Moore JC & Jevrejeva S (2004). Application of the cross wavelet transform and wavelet coherence to geophysical time series.

Guerra-Gomes S, Sousa N, Pinto L & Oliveira JF (2018). Functional Roles of Astrocyte Calcium Elevations: From Synapses to Behavior. *Front Cell Neurosci* **11,** 427.

Harris KD, Henze DA, Csicsvari J, Hirase H & Buzsaki G (2000). Accuracy of tetrode spike separation as determined by simultaneous intracellular and extracellular measurements. *J Neurophysiol* **84,** 401–414.

Hawco CS, Bagshaw AP, Lu Y, Dubeau F & Gotman J (2007). BOLD changes occur prior to epileptic spikes seen on scalp EEG. *Neuroimage* **35,** 1450–1458.

Herkenham M (1980). Laminar organization of thalamic projections to the rat neocortex. *Science (80-)* **207,** 532–535.

Hill MW, Wong M, Amarakone A & Rothman SM (2000). Rapid cooling aborts seizure-like activity in rodent hippocampal-entorhinal slices. *Epilepsia* **41,** 1241–1248.

Hoechstetter K, Bornfleth H, Weckesser D, Ille N, Berg P & Scherg M (2004). BESA source coherence: A new method to study cortical oscillatory coupling. *Brain Topogr* **16,** 233–238.

Hoffman WH & Haberly LB (1991). Bursting-induced epileptiform EPSPs in slices of piriform cortex are generated by deep cells. *J Neurosci* **11,** 2021–2031.

Holmes O, Wallace MN & Campbell AM (1987). COMPARISON OF PENICILLIN EPILEPTOGENESIS IN RAT SOMATOSENSORY AND MOTOR CORTEX. *Q J Exp Physiol* **72,** 439–452.

Van Horn JD & Poldrack RA (2009). Functional MRI at the crossroads. *Int J Psychophysiol* **73,** 3–9.

Hoshi Y (2003). Functional near-infrared optical imaging: Utility and limitations in human brain mapping. *Psychophysiology* **40,** 511–520.

Hubel DH (1957). Tungsten microelectrode for recording from single units. *Science (80-)* **125,** 549–550.

Ignarro LJ, Cirino G, Casini A & Napoli C (1999). Nitric oxide as a signaling molecule in the vascular system: An overview. *J Cardiovasc Pharmacol* **34,** 879–886.

Imoto H, Fujii M, Uchiyama J, Fujisawa H, Nakano K, Kunitsugu I, Nomura S, Saito T & Suzuki M (2006). Use of a Peltier chip with a newly devised local brain-cooling system for neocortical seizures in the

rat. Technical note. *J Neurosurg* **104,** 150–156.

Ito Y, Kennan RP, Watanabe E & Koizumi H (2000). Assessment of heating effects in skin during continuous wave near-infrared spectroscopy. *J Biomed Opt* **5,** 383–391.

Ives AE & Jefferys JGR (1990). Synchronization of epileptiform bursts induced by 4-aminopyridine in the in vitro hippocampal slice preparation. *Neurosci Lett* **112,** 239–245.

Jacobs J, LeVan P, Chander R, Hall J, Dubeau F & Gotman J (2008). Interictal high-frequency oscillations (80-500 Hz) are an indicator of seizure onset areas independent of spikes in the human epileptic brain. *Epilepsia* **49,** 1893–1907.

Jacobs J, LeVan P, Moeller F, Boor R, Stephani U, Gotman J & Siniatchkin M (2009). Hemodynamic changes preceding the interictal EEG spike in patients with focal epilepsy investigated using simultaneous EEG-fMRI. *Neuroimage* **45,** 1220–1231.

Jensen MS, Azouz R & Yaari Y (1994). Variant firing patterns in rat hippocampal pyramidal cells modulated by extracellular potassium. *J Neurophysiol* **71,** 831–839.

Jensen MS, Azouz R & Yaari Y (1996). Spike after-depolarization and burst generation in adult rat hippocampal CA1 pyramidal cells. *J Physiol* **492,** 199–210.

Juergens E, Guettler A & Eckhorn R (1999). Visual stimulation elicits locked and induced gamma oscillations in monkey intracortical- and EEG-potentials, but not in human EEG. *Exp Brain Res* **129,** 247–259.

Keller CJ, Truccolo W, Gale JT, Eskandar E, Thesen T, Carlson C, Devinsky O, Kuzniecky R, Doyle WK, Madsen JR, Schomer DL, Mehta AD, Brown EN, Hochberg LR, Ulbert I, Halgren E & Cash SS (2010). Heterogeneous neuronal firing patterns during interictal epileptiform discharges in the human cortex. *Brain* **133,** 1668–1681.

Kocharyan A, Fernandes P, Tong X-K, Vaucher E & Hamel E (2008). Specific subtypes of cortical GABA interneurons contribute to the neurovascular coupling response to basal forebrain stimulation. *J Cereb Blood Flow Metab* **28,** 221–231.

Kolb B & Whishaw IQ (2009). *Fundamentals of human neuropsychology*. Macmillan.

Kratzer I, Chip S & Vexler ZS (2014). Barrier mechanisms in neonatal stroke. *Front Neurosci* **8,** 359.

Lakatos P, Shah AS, Knuth KH, Ulbert I, Karmos G & Schroeder CE (2005). An Oscillatory Hierarchy Controlling Neuronal Excitability and Stimulus Processing in the Auditory Cortex. *J Neurophysiol*.

LaManna JC, McCracken KA, Patil M & Prohaska OJ (1989). Stimulus-activated changes in brain tissue temperature in the anesthetized rat. *Metab Brain Dis* **4,** 225–237.

Lassen NA, Ingvar DH & Skinhøj E (1978). Brain function and blood flow. *Sci Am* **239,** 62–71.

Lecrux C & Hamel E (2011). The neurovascular unit in brain function and disease. *Acta Physiol* **203,** 47–59.

Lennox WG (1939). John of Gaddesden on epilepsy. *Ann Med Hist* **3rd ser.,** 283–307.

Leppik IE (1997). *Contemporary diagnosis and management of the patient with epilepsy*. Handbooks in Health Care Newtown, PA.

Łęski S, Pettersen KH, Tunstall B, Einevoll GT, Gigg J & Wójcik DK (2011). Inverse current source density method in two dimensions: Inferring neural activation from multielectrode recordings. *Neuroinformatics* **9,** 401–425.

Leung L-WS (1985). Spectral analysis of hippocampal EEG in the freely moving rat: effects of centrally active drugs and relations to evoked potentials. *Electroencephalogr Clin Neurophysiol* **60,** 65–77.

Leung LS (2011). Field potential generation and current source density analysis. *Neuromethods* **54,** 1–25.

Lunden JW, Durens M, Phillips AW & Nestor MW (2019). Cortical interneuron function in autism spectrum condition. *Pediatr Res* **85,** 146–154.

Maggi CA & Meli A (1986). Suitability of urethane anesthesia for physiopharmacological investigations in various systems Part 1: general considerations. *Experientia* **42,** 109–114.

Mahmoudzadeh M, Wallois F, Kongolo G, Goudjil S & Dehaene-Lambertz G (2017). Functional maps at the onset of auditory inputs in very early preterm human neonates. *Cereb Cortex* **27,** 2500–2512.

Mandeville JB, Marota JJA, Ayata C, Zaharchuk G, Moskowitz MA, Rosen BR & Weisskoff RM (1999). Evidence of a cerebrovascular postarteriole windkessel with delayed compliance. *J Cereb Blood Flow Metab* **19,** 679–689.

Manoochehri M, Mahmoudzadeh M, Osharina V & Wallois F (2017). Shedding light on interictal epileptic spikes: An in vivo study using fast optical signal and electrocorticography. *Epilepsia*1–9.

Mansouri C & Kashou NH (2012). New window on optical brain imaging; medical development, simulations and applications. *Sel Top Opt fiber Technol*271–288.

Marsh ED, Peltzer B, Brown III MW, Wusthoff C, Storm Jr PB, Litt B & Porter BE (2010). Interictal EEG spikes identify the region of electrographic seizure onset in some, but not all, pediatric epilepsy patients. *Epilepsia* **51,** 592–601.

Mathern GW, Babb TL, Vickrey BG, Melendez M & Pretorias JK (1994). Traumatic compared to non-traumatic clinical-pathologic associations in temporal lobe epilepsy. *Epilepsy Res* **19,** 129–139.

Matsumoto H & Marsan CA (1964). Cortical cellular phenomena in experimental epilepsy: Interictal manifestations. *Exp Neurol* **9,** 286–304.

McAdams RM & Juul SE (2012). The role of cytokines and inflammatory cells in perinatal brain injury. *Neurol Res Int*; DOI: 10.1155/2012/561494.

McBain CJ, Traynelis SF & Dingledine R (1990). Regional variation of extracellular space in the hippocampus. *Science (80-)* **249,** 674–677.

McGinley MJ, Vinck M, Reimer J, Batista-Brito R, Zagha E, Cadwell CR, Tolias AS, Cardin JA & McCormick DA (2015). Waking state: rapid variations modulate neural and behavioral responses. *Neuron* **87,** 1143–1161.

McIntyre DC & Wong RK (1986). Cellular and synaptic properties of amygdala-kindled pyriform cortex in vitro. *J Neurophysiol* **55,** 1295–1307.

McNaught AD (comp. ., International Union of Pure and Applied Chemistry O (United K eng & Wilkinson A (comp. . (1997). Compendium of chemical terminology. IUPAC recommendations.

Millett D (2001). Hans Berger: From psychic energy to the EEG. *Perspect Biol Med* **44,** 522–542.

Mintun MA, Lundstrom BN, Snyder AZ, Vlassenko AG, Shulman GL & Raichle ME (2001). Blood flow and oxygen delivery to human brain during functional activity: theoretical modeling and experimental data. *Proc Natl Acad Sci* **98,** 6859–6864.

Mishra A, Reynolds JP, Chen Y, Gourine A V., Rusakov DA & Attwell D (2016). Astrocytes mediate neurovascular signaling to capillary pericytes but not to arterioles. *Nat Neurosci* **19,** 1619–1627.

Mitzdorf U (1985). Current source-density method and application in cat cerebral cortex: Investigation of evoked potentials and EEG phenomena. *Physiol Rev* **65,** 37–100.

Moretti R, Pansiot J, Bettati D, Strazielle N, Ghersi-Egea JF, Damante G, Fleiss B, Titomanlio L & Gressens P (2015). Blood-brain barrier dysfunction in disorders of the developing brain. *Front Neurosci* **9,** 40.

Muthuswamy J, Sridharan A & Okandan M (2016). MEMS Neural Probes BT - Encyclopedia of Nanotechnology. In, ed. Bhushan B, pp. 1993–2009. Springer Netherlands, Dordrecht.

Nguyen T (2010). Total Number of Synapses in the Adult Human Neocortex. *Undergrad J Math Model One + Two*; DOI: 10.5038/2326-3652.3.1.26.

Nicholson C & Freeman JA (1975). Theory of current source density analysis and determination of conductivity tensor for anuran cerebellum. *J Neurophysiol* **38,** 356–368.

Nioka S, Luo Q & Chance B (1997). Human brain functional imaging with reflectance CWS. In *Oxygen Transport to Tissue Xix*, pp. 237–242. Springer.

Nourhashemi M, Kongolo G, Mahmoudzadeh M, Goudjil S & Wallois F (2017). Relationship between relative cerebral blood flow, relative cerebral blood volume, and relative cerebral metabolic rate of oxygen in the preterm neonatal brain. *Neurophotonics* **4,** 21104.

Nourhashemi M, Mahmoudzadeh M & Wallois F (2016). Thermal impact of near-infrared laser in advanced noninvasive optical brain imaging. *Neurophotonics* **3,** 015001.

Obien MEJ, Deligkaris K, Bullmann T, Bakkum DJ & Frey U (2015). Revealing neuronal function through microelectrode array recordings. *Front Neurosci* **9,** 423.

Office of Health Economics (London E (1971). *Epilepsy in Society*.

Okazawa H & Vafaee M (2001). Effect of vascular radioactivity on regional values of cerebral blood flow: evaluation of methods for H215O PET to distinguish cerebral perfusion from blood volume. *J Nucl Med* **42,** 1032–1039.

Osharina V, Aarabi A, Manoochehri M, Mahmoudzadeh M & Wallois F (2017). Hemodynamic Changes Associated with Interictal Spikes Induced by Acute Models of Focal Epilepsy in Rats: A Simultaneous Electrocorticography and Near-Infrared Spectroscopy Study. *Brain Topogr* **30,** 390–407.

Osharina V, Ponchel E, Aarabi A, Grebe R & Wallois F (2010). Local haemodynamic changes preceding interictal spikes: A simultaneous electrocorticography (ECoG) and near-infrared spectroscopy (NIRS) analysis in rats. *Neuroimage* **50,** 600–607.

Ovchinnikov IA & Ovchinnikov YA (1987). *Retinal Proteins: Proceedings of an International Conference, Irkutsk (Lake Baikal), USSR, 22-28 July 1986*. VSP.

Pagliardini S, Funk GD & Dickson CT (2013). Breathing and brain state: urethane anesthesia as a model for natural sleep. *Respir Physiol Neurobiol* **188,** 324–332.

Papp EA, Leergaard TB, Calabrese E, Johnson GA & Bjaalie JG (2014). Waxholm Space atlas of the Sprague Dawley rat brain. *Neuroimage* **97,** 374–386.

Patel J, Marks K, Roberts I, Azzopardi D & Edwards AD (1998). Measurement of cerebral blood flow in newborn infants using near infrared spectroscopy with indocyanine green. *Pediatr Res* **43,** 34–39.

Paulson OB, Hasselbalch SG, Rostrup E, Knudsen GM & Pelligrino D (2010). Cerebral blood flow response to functional activation. *J Cereb Blood Flow Metab* **30,** 2–14.

Paxinos G & Watson C (2006). *The rat brain in stereotaxic coordinates: hard cover edition*. Elsevier.

Penfield W & Jasper H (1954). Epilepsy and the functional anatomy of the human brain.

Peppiatt CM, Howarth C, Mobbs P & Attwell D (2006). Bidirectional control of CNS capillary diameter by pericytes. *Nature* **443,** 700–704.

Pettersen KH, Devor A, Ulbert I, Dale AM & Einevoll GT (2006). Current-source density estimation based on inversion of electrostatic forward solution: Effects of finite extent of neuronal activity and conductivity discontinuities. *J Neurosci Methods* **154,** 116–133.

Petzold GC & Murthy VN (2011). Role of astrocytes in neurovascular coupling. *Neuron* **71,** 782–797.

Phillips CG, Zeki S & Barlow HB (1984). Localization of function in the cerebral cortex: past, present and future. *Brain* **107,** 328–361.

Pinault D, Leresche N, Charpier S, Deniau J, Marescaux C, Vergnes M & Crunelli V (1998). Intracellular recordings in thalamic neurones during spontaneous spike and wave discharges in rats with absence epilepsy. *J Physiol* **509,** 449–456.

Pogue BW, Patterson MS, Jiang H & Paulsen KD (1995). Initial assessment of a simple system for frequency domain diffuse optical tomography. *Phys Med Biol* **40,** 1709–1729.

Potworowski J, Jakuczun W, Łęski S & Wójcik DK (2011). Kernel current source density method. *BMC Neurosci* **12,** 1–2.

Pouzat C, Mazor O & Laurent G (2002). Using noise signature to optimize spike-sorting and to assess neuronal classification quality. *J Neurosci Methods* **122,** 43–57.

Proddutur A & Santhakumar V (2016). Fingerprints of interictal spikes: Can imprints deliver a verdict on their role in epilepsy? *Epilepsy Curr* **16,** 41–42.

Quairiaux C, Mégevand P, Kiss JZ & Michel CM (2011). Functional development of large-scale sensorimotor cortical networks in the brain. *J Neurosci* **31,** 9574–9584.

Quiroga RQ (2007). Spike sorting. *Scholarpedia* **2,** 3583.

Quiroga RQ, Reddy L, Kreiman G, Koch C & Fried I (2005). Invariant visual representation by single neurons in the human brain. *Nature* **435,** 1102–1107.

Rey HG, Pedreira C & Quian Quiroga R (2015). Past, present and future of spike sorting techniques. *Brain Res Bull* **119,** 106–117.

Roche-Labarbe N, Zaaimi B, Mahmoudzadeh M, Osharina V, Wallois A, Nehlig A, Grebe R & Wallois F (2010). NIRS-measured oxy- and deoxyhemoglobin changes associated with EEG spike-and-wave discharges in a genetic model of absence epilepsy: The GAERS. *Epilepsia* **51,** 1374–1384.

Rossokhin A V., Sharonova IN, Bukanova J V., Kolbaev SN & Skrebitsky VG (2014). Block of GABAA receptor ion channel by penicillin: Electrophysiological and modeling insights toward the mechanism. *Mol Cell Neurosci* **63,** 72–82.

Ruiz-Ezquerro JJ. (2008). Endemoniados, lunáticos y posesos: la epilepsia a través de los tiempos. In *De Cerebri Morbis.*, pp. 105–124. SANED, Madrid.

Rupawala M, Dehghani H, Lucas SJE, Tino P & Cruse D (2018). Shining a light on awareness: a review of functional near-infrared spectroscopy for prolonged disorders of consciousness. *Front Neurol* **9,** 350.

Saillet S, Quilichini PP, Ghestem A, Giusiano B, Ivanov AI, Hitziger S, Vanzetta I, Bernard C & Bénar CG (2016). Interneurons contribute to the hemodynamic/metabolic response to epileptiform discharges. *J Neurophysiol* **115,** 1157–1169.

Salimi I, Friel KM & Martin JH (2008). Pyramidal tract stimulation restores normal corticospinal tract connections and visuomotor skill after early postnatal motor cortex activity blockade. *J Neurosci* **28,** 7426–7434.

Sanzone M (2011). Neurotransmitters. In *Encyclopedia of Clinical Neuropsychology*, ed. Kreutzer JS, DeLuca J & Caplan B, pp. 1775–1776. Springer New York, New York, NY.

Scanziani M & Häusser M (2009). Electrophysiology in the age of light. *Nature* **461,** 930–939.

Schaefer MK, Hechavarría JC & Kössl M (2015). Quantification of mid and late evoked sinks in laminar current source density profiles of columns in the primary auditory cortex. *Front Neural Circuits* **9,** 52.

Seaba PJ (1984). Differential amplifiers and their limitations. *Am J EEG Technol* **24,** 11–23.

Seese TM, Harasaki H, Saidel GM & Davies CR (1998). Characterization of tissue morphology, angiogenesis, and temperature in the adaptive response of muscle tissue to chronic heating. *Lab Invest* **78,** 1553–1562.

Senzai Y, Fernandez-Ruiz A & Buzsáki G (2019). Layer-Specific Physiological Features and Interlaminar Interactions in the Primary Visual Cortex of the Mouse. *Neuron* **101,** 500-513.e5.

Seymour JP & Kipke DR (2007). Neural probe design for reduced tissue encapsulation in CNS. *Biomaterials* **28,** 3594–3607.

Siegel A, Marota JJ & Boas D (1999). Design and evaluation of a continuous-wave diffuse optical tomography system. *Opt Express* **4,** 287.

Siesjö BK (1978). Brain energy metabolism and catecholaminergic activity in hypoxia, hypercapnia and ischemia. *J Neural Transm Suppl*17.

Somogyvári Z, Cserpán D, Ulbert I & Érdi P (2012). Localization of single-cell current sources based on extracellular potential patterns: the spike CSD method. *Eur J Neurosci* **36,** 3299–3313.

Stafstrom CE (1998). The pathophysiology of epileptic seizures: a primer for pediatricians. *Pediatr Rev* **19,** 342–351.

Stanimirovic DB & Friedman A (2012). Pathophysiology of the neurovascular unit: Disease cause or consequence. *J Cereb Blood Flow Metab* **32,** 1207–1221.

Stice P, Gilletti A, Panitch A & Muthuswamy J (2007). Thin microelectrodes reduce GFAP expression in the implant site in rodent somatosensory cortex. *J Neural Eng* **4,** 42.

Strangman G, Boas DA & Sutton JP (2002). Non-invasive neuroimaging using near-infrared light. *Biol Psychiatry* **52,** 679–693.

Szabo I & Marczynski TJ (1993). A low-noise preamplifier for multisite recording of brain multi-unit activity in freely moving animals. *J Neurosci Methods* **47,** 33–38.

Szente M & Baranyi A (1987). Mechanism of aminopyridine-induced ictal seizure activity in the cat neocortex. *Brain Res* **413,** 368–373.

Thompson RF & Patterson MM (1973). *Bioelectric Recording Techniques: Pt. A. Cellular Processes and Brain Potentials*. Academic Press.

Traub RD & Wong RK (1982). Cellular mechanism of neuronal synchronization in epilepsy. *Science (80-)* **216,** 745–747.

Victor S & Weindling M (2008). Near-infrared spectroscopy and its use for the assessment of tissue perfusion in the neonate. In *Hemodynamics and Cardiology: Neonatology Questions and Controversies*, pp. 110–132. WB Saunders.

Vogels TP & Abbott LF (2009). Gating multiple signals through detailed balance of excitation and inhibition in spiking networks. *Nat Neurosci* **12,** 483.

Volterra A & Steinhäuser C (2004). Glial modulation of synaptic transmission in the hippocampus. *Glia* **47,** 249–257.

Walker AE (1945). Convulsive factor in commercial penicillin. *Arch Surg* **50,** 69.

Wallois F, Patil A, Héberlé C & Grebe R (2010). EEG-SPIR chez les patients épileptiques. *Neurophysiol Clin* **40,** 281–292.

Weber B, Keller AL, Reichold J & Logothetis NK (2008). The microvascular system of the striate and extrastriate visual cortex of the macaque. *Cereb Cortex* **18,** 2318–2330.

Williams P, White A, Ferraro D, Clark S, Staley K & Dudek FE (2006). The use of radiotelemetry to evaluate electrographic seizures in rats with kainate-induced epilepsy. *J Neurosci Methods* **155,** 39–48.

Wolbarsht ML, MacNichol EF & Wagner HG (1960). Glass insulated platinum microelectrode. *Science (80-)* **132,** 1309–1310.

World Health Organization (2019). *WHO | Epilepsy: a public health imperative*.

Yajuan X, Xin L & Zhiyuan L (2012). A comparison of the performance and application differences between manual and automated patch-clamp techniques. *Curr Chem Genomics* **6,** 87.

Yang X, Chang JH & Rothman SM (2003). Long-lasting anticonvulsant effect of focal cooling on experimental neocortical seizures. *Epilepsia* **44,** 1500–1505.

Yang XF & Rothman SM (2001). Focal cooling rapidly terminates experimental neocortical seizures. *Ann Neurol* **49,** 721–726.

Yang Y, Liu H, Li X & Chance B (1997). Low-cost frequency-domain photon migration instrument for

tissue spectroscopy, oximetry, and imaging. *Opt Eng* **36,** 1562–1569.

Yeager JD, Phillips DJ, Rector DM & Bahr DF (2008). Characterization of flexible ECoG electrode arrays for chronic recording in awake rats. *J Neurosci Methods* **173,** 279–285.